

Temperature changes in the tropical tropopause layer

Kohei Yoshida

Division of Earth System Science,
Graduate School of Environmental Science,
Hokkaido University

February 2011

Abstract

Temperature changes in the tropical tropopause layer (TTL) are examined in the cases of tropical sea-surface temperature (SST) changes as in El Niño/Southern oscillation, stratospheric sudden warming (SSW) event, and annual cycle.

We performed numerical experiments using an atmospheric general circulation model to assess the effect of convections associated with various tropical SST fields on the tropical tropopause (TT). The results reveal that in the case of a large (small) longitudinal gradient of tropical SST, the vertical heat flux ($\overline{w'\theta'}$) diverges strongly (weakly) around the TT, resulting in cooling (warming) of the TT. Divergence of $\overline{w'\theta'}$ is a primary controlling factor of variations in interannual TT temperature, especially during the peak of El Niño events. Analysis of ERA-Interim and ERA-40 data supports our results regarding the influence of $\overline{w'\theta'}$ on TT temperature.

Changes in the temperature in the TTL are investigated using ERA-Interim data during a major SSW event that started on about 16 January 2009. The tropics between 150 and 100 hPa started to cool from 18 January, and there is no clear relationship between the temperature anomalies in the tropical stratosphere and the TTL. On around 18 January, tropical ascent was the main contributor to cooling of the tropics between 150 and 100 hPa. Subsequently, convergence of $\overline{w'\theta'}$ resulted in a gradual decrease in temperature within the tropical uppermost troposphere. Waves propagated from Alaska to the tropics of the eastern Pacific and Atlantic at around 100 hPa, and the associated wave forcing drove the tropical ascent between 150 and 100 hPa.

A quantitative examination of the annual cycle of temperature and upwelling in the TTL and of momentum balance in the tropics is performed using ERA-Interim data to evaluate what causes annual cycle of temperature in the TTL. Results show that annual cycle in tropical temperature between 125 and 70 hPa is mainly driven by annual variation in tropical upwelling and consequent diabatic heating. The eastward residual forcing mainly drives annual cycle in tropical upwelling at 70 hPa. Variation in 125-100 hPa tropical upwelling between boreal winter and summer is dominated by wave forcing of stationary waves with meridional eddy momentum flux ($F_2^{(\phi)}$) and vertical flux of zonal momentum ($F_2^{(z)}$), and semiannual variation is dominated by eastward residual forcing and wave forcing of transient waves with $F_2^{(\phi)}$ and $F_2^{(z)}$.

Contents

Abstract	_____	i
1 General introduction	_____	1
2 Role of vertical eddy heat flux in the response of tropical tropopause temperature to changes in tropical sea surface temperature	_____	7
2.1 Introduction	_____	7
2.2 Data, model, and experiments	_____	9
2.3 Precipitation	_____	11
2.4 Temperature and meridional circulation	_____	12
2.5 Eliassen-Palm flux and meridional circulation	_____	13
2.6 Transformed Eulerian Mean thermodynamic analyses	_____	15
2.7 Vertical eddy heat flux	_____	18
2.8 Realistic SST experiment	_____	20
2.9 Concluding remarks	_____	21
3 Tropical cooling in the case of stratospheric sudden warming in January 2009: focus on the tropical tropopause layer	_____	37
3.1 Introduction	_____	37

3.2 Data and methods	38
3.2.1. Data	39
3.2.2. Transformed Eulerian Mean equations	38
3.2.3. Wave activity flux	40
3.2.4. Diagnosis of upwelling	40
3.2.5. Refractive index	42
3.2.6. Vertical interpolation	43
3.3 Temperature change and heat budget	43
3.4 Tropical upwelling generated by external forcing	44
3.5 Wave activity around the TTL	47
3.5.1 Eliassen-Palm flux	47
3.5.2 Three dimensional wave activity flux	48
3.6 Discussion	49
3.6.1 Tropical convection	49
3.6.2 Wave propagation towards the tropics	50
3.7 Summary	50
4 Seasonal changes in temperature and circulation in the tropical tropopause layer	
_____	64

4.1 Introduction	65
4.2 Data and methods	66
4.3 Transformed Eulerian Mean Thermodynamic analysis	67
4.4 Upwelling estimated from zonal mean momentum budget	69
4.5 Wave activity driving tropical upwelling	71
4.6 Behavior of eastward residual forcing	75
4.7 Summary	75
5 General conclusion	92
Acknowledgements	94
References	95

Chapter 1 | General Introduction

Tropical tropopause is the boundary between the troposphere and the stratosphere in the tropics. The traditional definitions of the tropopause are based on either temperature minimum (cold-point tropopause) or temperature lapse rate which meets a certain criterion (lapse rate tropopause; definition by the World Meteorological Organization).

However, observation of temperature, winds, and atmospheric trace gases suggests that the transition from the troposphere to the stratosphere occurs in a layer, rather than at a sharp tropopause [see *Highwood and Hoskins, 1998; Folkins et al., 1999; Fueglistaler et al., 2009a*]. The transition layer from the troposphere to the stratosphere may extend over several kilometers vertically, and is referred as tropical tropopause layer (TTL, sometimes also referred as tropical transition layer). *Fueglistaler et al. [2009a]* presents synthesis definition of the TTL with a bottom at 150 hPa, 355K, 14 km (pressure, potential temperature, and altitude) and a top at 70 hPa, 425 K, 18.5 km.

Due to tropical upwelling associated with dominant stratospheric circulation so-called “Brewer-Dobson (B-D) circulation”, the TTL acts as a gate to the stratosphere for atmospheric tracers such as water vapor.

TTL temperatures (especially minimum temperature in the TTL) are thought to limit the flux of water vapor into the stratosphere by freeze-drying (dehydration) and thus control stratospheric water vapor [*Holton and Gettleman, 2001; Hatsushika and Yamazaki, 2003; Fueglistaler et al., 2005*].

Despite its low abundance, stratospheric water vapor plays important roles in the radiative cooling in the stratosphere [e.g. *Forster and shine, 1999*] and stratospheric chemistry as the primary source for HO_x and in the activation of chlorine on polar stratospheric clouds (PSCs) that leads to ozone destruction [*Solomon et al., 1986*]. If TTL warms and thus stratospheric water vapor increases, these factors lead to destruction of stratospheric ozone. Hence, TTL temperature which controls water vapor in the stratosphere is important for the global climate system, and the importance has provided much of motivation for research on the TTL.

As an example of temperature variations in the TTL, 100 hPa tropical mean temperatures are shown in Figure 1.1-1.3.

Figure 1.1 shows annual cycle of 100 hPa tropical mean temperature. The

temperatures are low in boreal winter and high in boreal summer, have standard deviation at about 1.6 K. The peak-to-peak value is about 4 K and thus annual cycle has larger variability.

Figure 1.2 shows interannual variation in 100 hPa tropical temperature. Interannual variability of temperatures in the TTL, which has about 0.5 K standard deviation at 100 hPa, may arise because of El Nino Southern Oscillation (ENSO) [e.g. *Gettleman et al.*, 2001], volcano eruptions, and quasi-biennial oscillation (QBO) [*Baldwin et al.*, 2001].

Figure 1.3 shows intraseasonal variation in temperatures from December 2008 to February 2009. Such as Madden-Julian oscillation (MJO) [*Madden and Julian*, 1972], many phenomena may affect to the temperature variation. Stratospheric sudden warming (SSW) may also affect to the temperature variation.

Figure 1.4 shows saturation mixing ratio with respect to ice at 100 hPa. The saturation mixing ratio decreases rapidly with decreasing temperature. In the range of temperature from 185 to 195 K, temperature decrease of 4 K corresponds to decrease of saturation mixing ratio by half. Therefore, temperature changes in the TTL mentioned above have a large impact on the stratospheric water vapor.

As briefly stated above, temperature changes in the TTL are caused by various phenomena and in various timescales. However, about some of them, what mechanisms work to change in temperature in the TTL are still not clear completely.

The aim of this study is to clarify following issues;

- 1) thermodynamical and dynamical response of the TTL to tropical convection changes associated with ENSO and other sea surface temperature (SST) changes in the tropics,
- 2) thermodynamical and dynamical variations in the TTL during SSW (which investigate during a remarkable SSW event in second half of January 2009),
- 3) main drivers of annual cycle in temperature in the TTL and their degrees of contribution.

In the present study, the range of the TTL is defined as a bottom at 150 hPa and a top at 70 hPa between 10° S and 10° N.

The remainder of this paper is organized as follows. Chapter 2 examines issue 1), Chapter 3 deals with issue 2), and Chapter 4 tackles issue 3). Finally, general overview of the present study is given in Chapter 5.

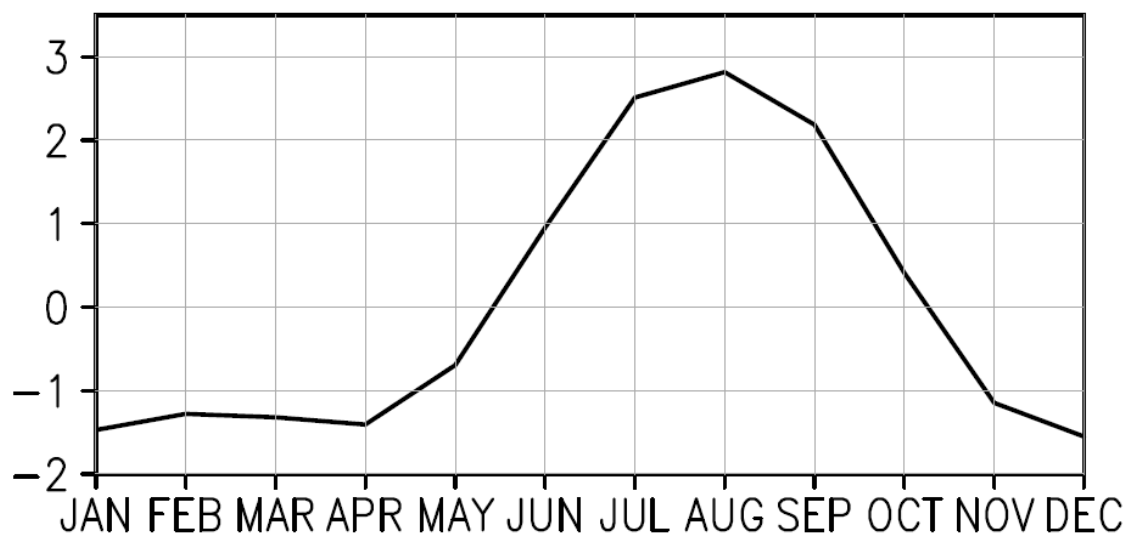


Figure 1.1. Annual cycle of 100 hPa zonal mean temperatures averaged over 10° S- 10° N (K) from ECMWF ERA-Interim 1989-2009 (time mean has been removed).

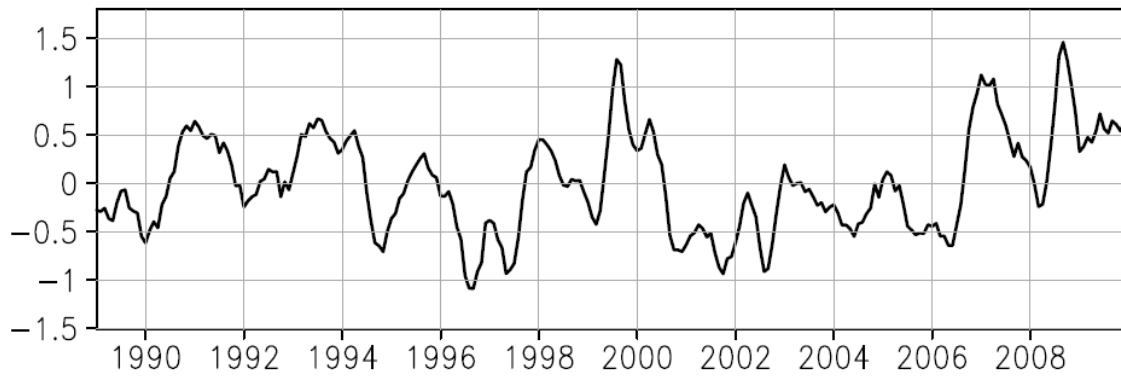


Figure 1.2. 100 hPa zonal mean temperatures averaged over 10°S - 10°N (K) from ECMWF ERA-Interim 1989-2009 (climatological annual cycle has been removed). Data are smoothed using a 5-month running average.

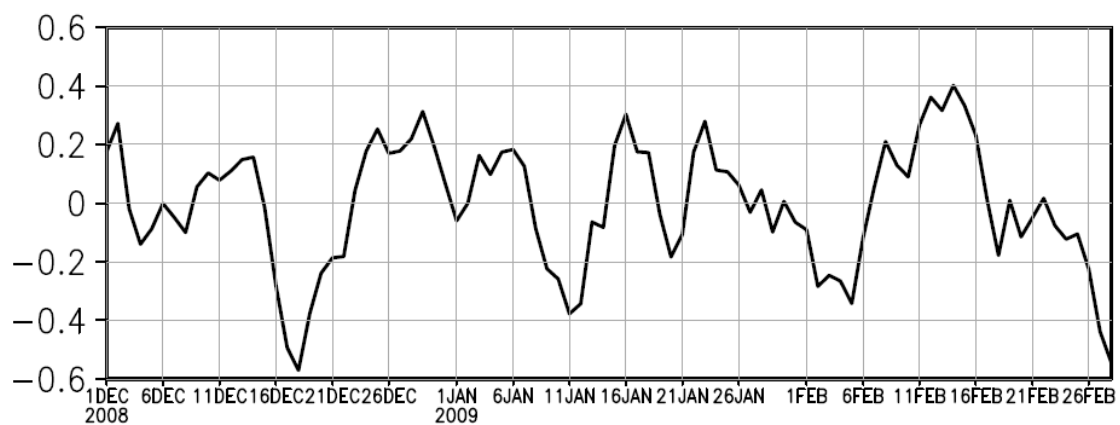


Figure 1.3. 100 hPa zonal mean temperature anomalies averaged over 10° S-10° N (K) from ECMWF ERA-Interim. The anomalies are deviation from 41-day running average. Data are smoothed using a 3-day running average.

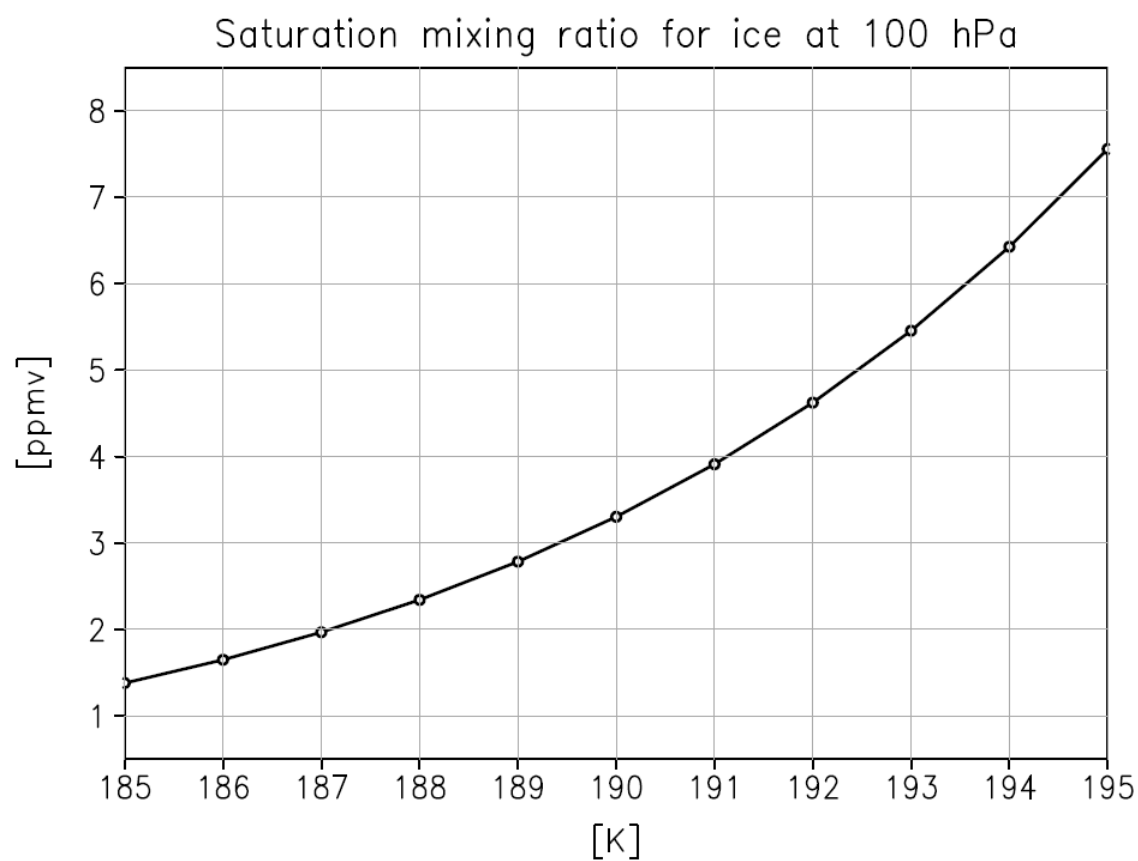


Figure 1.4. Saturation mixing ratio with respect to ice at 100 hPa. The temperature range is from 185 to 195 K. Saturated vapor pressure over ice is calculated from the equation in *Marti and Mauersberger (1993)*.

Chapter 2| Role of vertical eddy heat flux in the response of tropical tropopause temperature to changes in tropical sea surface temperature

2.1. Introduction

The tropical tropopause (TT) region plays an important role in governing the large-scale distribution of moisture in the stratosphere, because air entering the stratosphere is strongly dehydrated in the TT region [Holton and Gettleman, 2001; Hatsushika and Yamazaki, 2003; Fueglistaler *et al.*, 2005]. Hence, the structure of the TT and its spatial and temporal variations have been investigated in several previous studies [e.g., Highwood and Hoskins, 1998; Hartmann, 2007].

The TT temperature varies seasonally, being lower in the boreal winter and higher in the boreal summer. Two mechanisms have been invoked to explain this seasonal variation. First, stratospheric circulation, characterized by upward flow in the tropics and poleward-downward flow in the extratropics, known as Brewer–Dobson (B–D) circulation, controls the TT temperature by diabatic upwelling [Yulaeva *et al.*, 1994; Holton *et al.*, 1995]. The wave forcing caused by planetary-scale, synoptic-scale, and gravity wave dissipations in the subtropical and extratropical stratosphere, mainly in the winter hemisphere, drags on stratospheric poleward flow and induces upward motion in the tropics (the so-called “stratospheric pump”) [Haynes *et al.*, 1991; Plumb and Eluszkiewicz, 1999]. This forcing is stronger in the Northern Hemisphere, and induces stronger upward motion and lower temperatures during the boreal winter.

The second mechanism that influences the seasonality of TT temperature is the effect of localized meridional circulation in the TT region caused by equatorial waves [Kerr-Munslow and Norton, 2006]. Such waves are excited mainly by longitudinally localized deep convection around the equatorial western Pacific. Because the localized deep convection occurs around the equator during the boreal winter and around 15°N during the boreal summer, this wave forcing is stronger near the TT during the boreal winter. Therefore, upward motion is stronger and temperatures are lower during the

boreal winter. In addition, based on the results of an idealized AGCM experiment, *Norton* [2006] suggested that when the localized deep convection is shifted far from the equator (conditions corresponding to the boreal summer), tropical wave activity is weakened in the TT region.

Seasonal variations in convection in the tropics are caused by changes in SST distribution. The annual timescale is the dominant period driving such variations, but other timescales also make a contribution. For example, the El Niño/Southern Oscillation (ENSO) is known to strongly influence tropical temperature structure and wave activity [*Trenberth and Smith*, 2006], and the SST distribution in the Pacific is close to being zonally uniform in El Niño years because of weakening of the longitudinal SST gradient in the tropical Pacific. Consequently, it is important to investigate how the TT temperature varies at timescales other than annual, and in realistic situations.

Norton [2006] performed simulations using a seasonally fixed model with idealized diabatic heating in the tropical troposphere, following the simple model employed by *Gill* [1980]. In this approach, the heating distribution was prescribed as Gaussian in the horizontal and vertical. In reality; however, diabatic heating in the tropical troposphere is caused mainly by moist convection and depends on tropical SST.

In the present study, we examine the response of the zonal-mean TT temperature to various tropical SST fields via three experiments performed using an atmospheric general circulation model (AGCM). In the first experiment, we varied the longitudinal gradient of tropical SST. The second experiment was performed with variable mean tropical SST. These two experiments were designed to investigate how TT temperature changes with changing zonal mean part of an ENSO-like SST field and with perturbation of this field. Finally, the third experiment was performed with realistic SST during the 1997/98 El Niño period.

Following the methodology of *Kerr-Munslow and Norton* [2006], we performed a thermodynamic budget analysis within the transformed Eulerian mean framework. We found that the vertical eddy heat flux, which has not been considered in previous studies, strongly influences the TT temperature.

The remainder of this chapter is organized as follows. Section 2.2 describes the dataset, model, and experiments. Section 2.3 deals with changes in precipitation, and Section 2.4

discusses changes in temperature and meridional circulation near the TT. Section 2.5 describes wave activity that drives meridional circulation, and in Section 2.6 we assess the thermodynamic budget in the tropics. Section 2.7 considers the mechanism of vertical eddy heat flux, and Section 2.8 compares the results of realistic SST experiments with observations. Finally, Section 2.9 provides a discussion and summary of the conclusions.

2.2. Data, model, and experiments

The AGCM used in this study was developed by the Center for Climate System Research and the National Institute for Environmental Studies (CCSR/NIES) [Numaguti *et al.*, 1995]. The resolution is T42L24, with the model top at 0.4 hPa. The model has state-of-the-art physical processes, and was used previously to study the TT layer [Hatsushika and Yamazaki, 2003]. We define the TT as the coldest region (the so-called cold-point tropopause) between 10°N and 10°S. The TT in this model is located at about 90 hPa and is fixed at 90 hPa hereafter.

Three experiments were performed with various SST fields. Each experiment was designed to assess the response of TT temperature when the tropics is forced by different SST fields between 15°S and 15°N. The SST distributions used in the experiments were as follows:

- (1) Standard SST (Control run or CTR)
- (2) Changing longitudinal gradient of tropical SST (EXP1)
- (3) Changing mean tropical SST (EXP2)
- (4) Observed SST (EXP3)

The Standard SST case (CTR) uses the seasonally varying climatological SST field provided by the Atmospheric Model Intercomparison Project (AMIP I) [Gate, 1992]. The SST fields used in EXP1 and EXP2 are based on the AMIP SST and are given simple spatial change in the tropics.

The SST is decomposed into a zonal mean part and a perturbation part, as follows:

$$SST = \overline{SST} + SST', \quad (2.1)$$

where \overline{SST} is the zonal-mean SST and SST' is the departure from the zonal mean. In

EXP1, the perturbation part of AMIP SST is doubled or halved as follows:

$$\begin{aligned} [2SST'] &= \overline{SST} + 2SST' \\ [0.5SST'] &= \overline{SST} + 0.5SST' \end{aligned} \quad (2.2)$$

In EXP2, the zonal mean part of AMIP SST increases or decreases by 1 K, as follows:

$$\begin{aligned} [\overline{SST} + 1] &= \overline{SST} + 1[\text{K}] + SST' \\ [\overline{SST} - 1] &= \overline{SST} - 1[\text{K}] + SST' \end{aligned} \quad (2.3)$$

Figure 2.1 shows the annual-mean SST field for each experiment (except EXP3). Figure 2.1a shows the annual-mean SST used in the Standard SST run (CTR), and Figure 2.1b shows the SST field in the case of the perturbation part being doubled ($2SST'$). There exists a large longitudinal SST difference between the eastern and western tropical Pacific. Figure 1c shows the SST field in the case of the perturbation part being halved ($0.5SST'$). There exists a small temperature difference between the eastern and western tropical Pacific. Figure 2.1d and 2.1e shows the cases in which the tropical SST fields are increased ($\overline{SST} + 1$) and decreased ($\overline{SST} - 1$) by 1 [K], respectively.

In CTR, EXP1, and EXP2, the model was integrated for 20 years, with the model output for the last 15 years being analyzed; subsequently, the monthly annual cycle of climatology was calculated.

EXP3 was performed using observed SST for the period between January 1996 and December 1999 as a four-member initial-value ensemble. Data sets in January 1st of four years in CTR were applied as initial values for each member. Integration using the observed SST started in January 1996. Ensemble mean was calculated after analysis was made for each member. During this period, a distinct El Niño event took place, peaking in January 1998. The observed SST field was provided by the Hadley Centre Global Sea Ice Coverage and Sea Surface Temperature data on a $1^\circ \times 1^\circ$ grid (HadISST1.1). These SST data sets were interpolated to match the T42 resolution.

To confirm the validity of the model results, the results of EXP3 were compared with

those of ERA-Interim, which is the latest reanalysis data set provided by the European Centre of Medium-Range Weather Forecasts (ECMWF) [Simmons *et al.*, 2006; Uppala *et al.*, 2008]. The ERA-Interim data set has a smaller assimilation increment of temperature around the TT than does the ECMWF 40 Year Re-Analysis (ERA40) [Fueglistaler *et al.*, 2009b], which is a former reanalysis data set [see Simmons and Gibson, 2000; Uppala *et al.*, 2005]; therefore, ERA-interim is an appropriate data set for this study. The data period used in this study is from January 1989 to December 2008. The ERA40 data set is also compared. Kerr-Munslow and Norton [2006] used ECMWF 15-year Re-Analysis (ERA15), which has weaker vertical velocity in the TT region than do ERA-interim and ERA40.

2.3. Precipitation

To assess how convection is modified by SST change, Figure 2.2 shows precipitation in CTR and the difference from CTR for each of the other runs. The figure shows annual-mean precipitation, and its anomalies from CTR and their zonal mean values.

Figure 2.2a-left shows that the region in CTR with high precipitation corresponds to the Inter Tropical Convergence Zone (ITCZ) and Southern Pacific Convergence Zone (SPCZ). The region of maximum precipitation is located around the tropical western Pacific. Figure 2.2a-right shows that the zonal-mean precipitation has a sharp peak at around 7°N.

Figure 2.2b-left shows that precipitation increases around the dateline in areas south of the equator, and decreases along 10°N, except around 160°E in $2SST'$. Thus, the longitudinal gradient of precipitation increases in the tropics. Figure 2.2b-right shows that the shape of the major precipitation band becomes smooth in the tropics because zonal-mean precipitation increases along 10°S and decreases along 7°N in $2SST'$. In addition, the total precipitation in $2SST'$ is similar to that in CTR in the tropics.

Figure 2.2c-left shows that the precipitation anomaly pattern in $0.5SST'$ is almost opposite to that in $2SST'$ (Figure 2.2b-left). Thus, the longitudinal gradient of precipitation is reduced, and Figure 2.2c-right shows that the zonal-mean precipitation maximum at 7°N is more pronounced than that of CTR.

Figure 2.2d-left shows a precipitation increase along 10°N and 10°S in $\overline{SST} + 1$, whereas it is suppressed along 20°N and 20°S. Figure 2.2d-right shows that the

zonal-mean precipitation increases in the tropics, especially at 12°S and 12°N, whereas it decreases at around 20°S and 20°N. Figure 2.2e shows that the precipitation anomaly pattern in $\overline{SST} - 1$ is almost the opposite to that in $\overline{SST} + 1$ (Figure 2.2d).

2.4. Temperature and meridional circulation

Figure 2.3 shows meridional structures of the annual-mean zonal-mean temperature anomalies and residual mean stream function anomalies. Figure 2.3a shows that in $2SST'$, the temperature increases in the tropical troposphere, and decreases in the tropical lower stratosphere and TT. In addition, the residual mean vertical velocity increases between 15°S and 5°N, and decreases at around 10°N in the upper troposphere. These changes in the upper tropical troposphere correspond to the positive precipitation anomalies around 10°S and negative anomalies around 5°N (see dashed line in Figure 2.2b right). Anomalies of residual mean stream function between 20°N-20°S in the lower stratosphere mean anomalies of upward flow in the TT and poleward flow in the subtropical lower stratosphere, although the anomaly of the residual mean circulation is weak. The temperature in the equatorial lower stratosphere decreases in association with the ascending anomaly at around 70 hPa. The weak anomalous cells don't seem to be able to quantitatively make the temperature decrease in the TT region and the lower tropical stratosphere. This issue will be discussed in the next section by heat budget analysis. The zero line for the temperature anomaly is located near 100 hPa. Temperature shows an increase in the extratropical stratosphere.

In contrast, Figure 2.3b shows that temperature decreases in the tropical troposphere and increases in the tropical lower stratosphere in $0.5SST'$. The anomaly of the residual mean stream function indicates downwelling around the TT. The zero line for the temperature anomaly is located near 110 hPa, slightly lower than the zero line in $2SST'$ (Figure 2.3a). Except for the altitude of the zero line of temperature, the result of the $0.5SST'$ experiment is the opposite to that of the $2SST'$ experiment.

In EXP1, it is interesting that despite the minor anomaly in total tropical precipitation, the tropical tropospheric temperature increases, probably due to a change in the distribution of precipitation. The warming in the troposphere shows a maximum at 150 hPa, mainly caused by the vertical eddy heat flux. This effect is discussed in detail in the following Sections 2.6-2.7.

Figure 2.3c reveals that the temperature shows a marked increase in the tropical troposphere and decreases around the equator at 50 hPa. The zero line of the temperature anomaly is located near 80 hPa, and most of the extratropical stratosphere is warmed. The upward flow is intensified in the tropics, and a downward flow anomaly is generated in the extratropical stratosphere.

Figure 2.3d shows almost the opposite patterns in temperature and residual stream function to the result obtained for the $\overline{SST} + 1$ experiment (Figure 2.3c), except for the zero line of temperature near 90 hPa. B–D circulation is intensified in $\overline{SST} + 1$ and weakened in $\overline{SST} - 1$. Dynamical temperature changes due to vertical flow are pronounced in the stratosphere in EXP2, which shows a strong relationship between temperature anomalies and residual circulation anomalies in the upper TT layer. This relationship is not seen in EXP1 because of the use of a different SST field. Figure 2.3 shows that the temperature anomalies between 70 and 90 hPa in EXP1 have a larger amplitude than those in EXP2, despite the weaker circulations around the TT.

The above results provide the following questions:

- (1) What is the cause of the residual circulation anomalies in the lower stratosphere and the TT layer?
- (2) The zonal-mean temperature anomaly response of EXP1 between 70 and 90 hPa in the tropics is not in agreement with residual circulation anomalies. Are there any other effects in addition to residual circulation?

To understand how residual circulation is affected by wave forcing near the TT, the Eliassen–Palm (EP) fluxes of these runs are analyzed, along with the circulations, in Section 2.5. Furthermore, to understand the cause of TT temperature change, the transformed Eulerian Mean (TEM) thermodynamics budget is analyzed in Section 2.6.

2.5. Eliassen-Palm flux and meridional circulation

Figure 2.4 shows anomalies of EP flux and residual mean stream function in the upper troposphere and lower stratosphere. These results indicate that wave forcing drives residual mean meridional circulation around the TT.

Figure 2.4a shows that EP flux anomalies in $2SST'$ are headed from the equatorial upper troposphere to the lower stratosphere and into the subtropical upper troposphere, causing divergence in the equatorial upper troposphere and convergence in the

surrounding region. The poleward flow in the tropical stratosphere, driven by this wave forcing, induces upward flow around the TT.

In Figure 2.4b, $0.5SST'$ produces the opposite anomaly in EP flux to that obtained in $2SST'$, causing convergence in the equatorial upper troposphere and divergence in the surrounding region. The equatorward residual mean meridional circulation anomalies, driven by anomalies of the opposite wave forcing to that obtained in $2SST'$, induce downward residual mean vertical circulation anomalies in the TT region.

Figure 2.4c shows that EP flux anomalies in $\overline{SST} + 1$ diverge slightly from the upper equatorial troposphere and converge weakly in the subtropical upper troposphere, corresponding with the residual mean stream function anomalies. The poleward circulation anomalies in the mid-latitude stratosphere are driven by convergence of EP flux anomaly around the subtropical lower stratosphere. The vertical motion around the TT is enhanced to compensate for poleward circulation, and its amplitude and spatial range are larger than those in $2SST'$. Figure 2.4d shows that the EP flux anomaly in $\overline{SST} - 1$ results in almost the opposite residual mean meridional circulation to that obtained in $\overline{SST} + 1$.

There exists a difference between EXP1 and EXP2 regarding whether the greatest change is seen in mid-latitude large-scale waves or equatorial waves. In EXP1, the residual mean meridional circulation changes with large-scale equatorial waves excited from the tropical upper troposphere; this change is localized in the TT region and is consistent with the results of *Norton* [2006]. In EXP2, the residual mean meridional circulation around the TT changes with EP flux in the subtropical lower stratosphere, which corresponds to changes in B–D circulation. The EP flux changes in the subtropical lower stratosphere are mostly caused by changes in quasi-planetary and synoptic waves (zonal wave number 3-6). A large (small) meridional temperature gradient in the troposphere, arising from the enhancement (reduction) of convection, induces a strong (weak) subtropical jet by about 4 m/s increment at its peak (not shown). Because the wave activity is modified by change of the amplitude of the westerlies, it is suggested that a change in the subtropical jet affects the intensity of the stratospheric pump. This result is in good agreement with the findings of *Olsen et al.* [2007], which indicate that variation in the convection modifies large-scale wave propagation in the extratropics and amplitude of the B–D circulation via change in the subtropical jet.

2.6. Transformed Eulerian Mean thermodynamic analyses

Here, we assess the thermodynamic budget in the TT layer using the TEM thermodynamics equation in $\log p$ coordinates [see *Andrews et al.*, 1987]:

$$\frac{\partial \bar{\theta}}{\partial t} = -\bar{v}^* \frac{\partial \bar{\theta}}{a \partial \phi} - \bar{w}^* \frac{\partial \bar{\theta}}{\partial z} + \bar{Q} - \frac{1}{\rho_0} \frac{\partial}{\partial z} \left(\overline{v' \theta'} \frac{\bar{\theta}_\phi}{a \theta_z} \right) - \frac{1}{\rho_0} \frac{\partial}{\partial z} \left(\rho_0 \overline{w' \theta'} \right); \quad (2.4)$$

$$\bar{v}^* \equiv \bar{v} - \frac{1}{\rho_0} \frac{\partial}{\partial z} \left(\rho_0 \frac{\overline{v' \theta'}}{\theta_z} \right), \quad \bar{w}^* \equiv \bar{w} - \frac{1}{a \cos \phi} \frac{\partial}{\partial \phi} \left(\cos \phi \frac{\overline{v' \theta'}}{\theta_z} \right), \quad (2.5)$$

where the overbar denotes the zonal mean, the prime is the departure from the zonal mean, subscripts denotes partial differentiation, a is the radius of earth, θ is potential temperature, ϕ is latitude, ρ_0 is the reference density, Q is diabatic heating, \bar{v}^* is the residual mean meridional wind, and \bar{w}^* is the residual mean vertical wind. The diabatic heating term is calculated from the residual in equation (2.4). The second term on the right-hand-side is vertical advection, and the last (5th) term is convergence of the vertical eddy heat flux. Due to long time average, time change rate of the temperature is approximately zero. Around the TT, diabatic heating mainly consists of longwave radiative heating because of low abundances of ozone and water vapor. Longwave radiative heating approximately can be expressed by Newtonian (longwave) cooling, that is $Q \approx -\tau^{-1}(\theta - \theta_{Q=0})$ (τ is radiative relaxation time). Therefore, diabatic heating in the TT layer is almost passive forcing for temperature changes, and difference in the temperature between experiments corresponds to that in diabatic heating. In addition, difference in thermodynamic forcing which has same sign as difference in temperature contributes as active forcing.

Vertical profiles of the thermodynamic balance and their difference from those in CTR around the TT are investigated below. Figure 2.5 shows annual-mean vertical profiles of terms in the TEM thermodynamic budget and zonal-mean temperature, averaged between 10°S and 10°N. The major terms in equation (2.4) are shown in this figure; those terms not shown are negligible. Figure 2.5a shows a cold point at 90 hPa in CTR. Thermodynamic balance is largely maintained by vertical advection and diabatic

heating at each level. Divergence of the vertical eddy heat flux slightly cools the TT.

Figure 2.5b shows that the temperature decreases between 90 and 50 hPa and increases between 150 and 110 hPa in $2SST'$. In addition, the temperature between 150 and 80 hPa changes with convergence of vertical eddy heat flux. Divergence of vertical eddy heat flux is pronounced at 90 hPa; temperature decreases by 0.3 K at this height. Vertical advection leads to a reduced temperature above 80 hPa.

Figure 2.5c shows that temperature increases between 100 and 50 hPa and decreases between 150 and 130 hPa in $0.5SST'$. Convergence of the vertical eddy heat flux leads to a change in temperature between 150 and 80 hPa, and the temperature at 90 hPa increases by 0.8 K due to convergence of the vertical eddy heat flux. The vertical advection leads to an increase in temperature above 80 hPa.

Figure 2.5d shows that the temperature increases between 150 and 90 hPa (peak warming is located at 300 hPa, due to diabatic heating) and decreases between 70 and 50 hPa (due to vertical advection) in $\overline{SST} + 1$. The TT temperature increases due to diabatic heating.

Figure 2.5e shows that the temperature decreases between 150 and 100 hPa (peak cooling is located at 300 hPa, due to diabatic cooling), and vertical advection leads to an increase in temperature between 80 and 50 hPa in $\overline{SST} - 1$. The TT temperature is largely unchanged because of the three terms cancel each other out.

In EXP1, convergence of the vertical eddy heat flux results in marked changes in the temperature around the TT, whereas in EXP2, convergence of the vertical eddy heat flux is ineffective.

Figure 2.6 shows the annual cycle of the thermodynamic budget at 90 hPa in each experiment. Figure 2.6a shows that the TT temperature is warm from June to November (maximum in August at 193 K) and cold from December to May (minimum in February at 189 K). The annual cycle of TT temperature is in good agreement with the annual cycle of vertical advection, consistent with the results reported by *Kerr-Munslow and Norton* [2006]. Although convergence of the vertical eddy heat flux shows a similar annual cycle, it is of small magnitude.

The TT temperature in $2SST'$ shows slight increases in February and March, and decreases in other months (Figure 2.6b), especially from September to November (minimum in October at -0.7 K). The annual cycle of convergence of the vertical eddy

heat flux anomaly closely resembles that of the TT temperature anomaly, and the annual cycle of the vertical advection anomaly is similar to that of the TT temperature anomaly. The diabatic heating anomaly shows opposite variations to the TT temperature anomaly.

The TT temperature in $0.5SST'$ increases in all months, with the largest increase in December (+1.3 K; Figure 2.6c). The TT temperature anomaly is in good agreement with the anomalies of convergence of the vertical eddy heat flux and vertical advection. The diabatic heating anomaly shows opposite variations to the TT temperature anomaly.

In $\overline{SST} + 1$, the TT temperature shows a large increase during March–May (maximum in April at 1.0 K) (Figure 2.6d) and a minor increase during August–October (minimum in August at 0.1 K). Vertical advection and convergence of the vertical eddy heat flux show a similar annual cycle anomaly to that of zonal-mean temperature, especially during July–September. Although the diabatic heating anomaly shows the opposite variations to the TT temperature anomaly, these anomalies have positive values.

In $\overline{SST} - 1$ (Figure 2.6e), the TT temperature decreases from January to June (minimum in May at -0.3 K) and increases from July to December (maximum in August at 0.5 K). Differences in the vertical advection and convergence of the vertical eddy heat flux are of small amplitude, but these annual cycles are similar to that of zonal-mean temperature. The diabatic heating anomaly is of small amplitude compared with the TT temperature anomaly in the other cases, and has negative values.

In EXP1, the annual cycle of the TT temperature anomaly is similar to that of convergence of the vertical eddy heat flux anomaly. The strong cooling months in $2SST'$ (August–October) and strong heating months in $0.5SST'$ (December–February) due to convergence of the vertical eddy heat flux correspond to weak cooling months and strong cooling months in CTR, respectively.

In EXP2, the diabatic heating anomaly has the same sign or weak counteraction as the TT temperature anomaly, which can be explained by the changing intensity of long-wave radiation emitted from the sea surface due to variations in tropical SST. The annual cycle of TT temperature anomalies is poorly-matched to the cycles of vertical advection and convergence of the vertical eddy heat flux. Previous studies have suggested that changes in tropical SST and cloud-top-height influence the long-wave radiative emission absorbed by the TT [e.g., *Hartmann et al.*, 2001]. The role of diabatic

heating in this regard will be considered in a future study.

2.7. Vertical eddy heat flux

The previous section demonstrated that when a change occurs in the longitudinal gradient of tropical SST, convergence of the vertical eddy heat flux $(\overline{w'\theta'})$ —the last term in equation (4)—is important in terms of changes in the temperature of the TT layer. However, the importance of this term has not been emphasized in previous studies, such as studies of seasonal variations in TT temperature [e.g., *Kerr-Munslow and Norton, 2006*], because the amplitude of this term is so small that it is neglected in climatological mean cases (Figs. 2.5a and 2.6a). To understand in detail the causes of the vertical eddy heat flux, we investigate the time scale and spatial structure of perturbations of the vertical velocity and potential temperature that drive the vertical eddy heat flux around the TT. The months considered in this analysis were those with the largest amplitude of convergence of vertical eddy heat flux (i.e., December–February in both CTR and 0.5SST').

Perturbation of the vertical velocity can be decomposed into the monthly mean perturbation and the deviation from the monthly mean perturbation, as follows:

$$w' = [w'] + w'^*, \quad (2.6)$$

where the square brackets indicate the monthly mean and the asterisk indicates the deviation of the monthly mean. The monthly mean of the vertical eddy heat flux can then be decomposed into a stationary part, which consists of monthly mean perturbations, and a transient part, which consists of the deviations of the monthly mean perturbation, as follows:

$$[w'\theta'] = [w'][\theta'] + [w'^*\theta'^*], \quad (2.7)$$

where the first term of the right-hand side is the stationary part of the vertical eddy heat flux and the second term is the transient part.

Figure 2.7 shows horizontal wind, perturbations in both vertical velocity w' and potential temperature θ' , and the vertical eddy heat flux decomposed into the stationary

part $[w'\theta']$ and transient part $[w'^*\theta'^*]$ for the period between December and February in CTR. A pair of strong anticyclones around the western Pacific straddles the equator, with large positive w' and large negative θ' located between the anticyclones. Therefore, the stationary part of the vertical eddy heat flux is strongly negative in the equatorial western Pacific, as well as being negative in the area south of the equatorial eastern Pacific and in the equatorial Atlantic. Although the transient part of the vertical eddy heat flux also has large negative values along the equator, its amplitude is smaller than that of the stationary part (note that the range of values in the scale for the stationary vertical eddy heat flux is about three times greater than that in the scale for the transient flux). This circulation pattern, with anticyclones and westerly winds in the equatorial Pacific, is the “Matsuno–Gill pattern,” which is induced by localized heating in the equatorial western Pacific [Matsuno, 1966; Gill, 1980]. However, the vertical eddy heat flux in the equatorial western Pacific has relatively small negative value at 70 hPa ($0 \approx (\overline{w'\theta'})_{70\text{hPa}} > (\overline{w'\theta'})_{100\text{hPa}}$; not shown). Therefore, difference of the vertical eddy heat flux between 70 and 100 hPa generates divergence of the vertical eddy heat flux ($-\rho_0^{-1}\partial(\rho_0\overline{w'\theta'})/\partial z < 0$) in the TT, and divergence of the vertical eddy heat flux cools the TT.

Figure 2.8 shows differences in the vertical eddy heat flux between $0.5SST'$ and CTR at 100 hPa during the period December–February. The amplitudes of vertical velocity and potential temperature are reduced in the tropics, especially in the equatorial western Pacific and south of the equatorial eastern Pacific. The circulation pattern is obviously weakened in the tropics, except between 0° and 60°E . The vertical eddy heat flux in the stationary part is offset in the tropics, especially in the equatorial western Pacific and south of the equatorial eastern Pacific, and the amplitude of the vertical eddy heat flux in the transient part is offset along the equator. Therefore, divergence of the vertical eddy heat flux is reduced in the TT, and the TT temperature increases due to a reduction in divergence of the vertical eddy heat flux. The Matsuno–Gill pattern is visibly weakened at 100 hPa in $0.5SST'$, coincident with a reduction in divergence of the vertical eddy heat flux.

Figure 2.9 shows vertical profiles of the annual-mean zonal-mean vertical eddy heat flux averaged over the tropics in CTR and EXP1. The vertical eddy heat flux is divided into two time scales: longer and shorter than 1 month. The stationary part of the vertical

eddy heat flux shows a marked change at around 100 hPa in EXP1. Although the transient part of the vertical eddy heat flux has similar amplitude to that of the stationary part, its vertical gradient is small around the TT.

Localized convection generates the Matsuno–Gill pattern in the tropical troposphere. Consequently, ascending flow in the equatorial western Pacific transports the cold perturbation at 100 hPa upward (i.e., negative vertical eddy heat flux; Figure 2.10). Because the amplitude of the negative vertical eddy heat flux is reduced upward in the equatorial western Pacific, the vertical eddy heat flux diverges in the TT, leading to a reduction in TT temperature. A reduction in the longitudinal gradient of tropical SST results in weakening of the Matsuno–Gill pattern. Consequently, the TT temperature increases in response to a decrease in the divergence of the vertical eddy heat flux in $0.5SST'$. The longitudinal gradient of tropical SST is reduced during El Niño events.

2.8. Realistic SST experiment

Figure 2.11 shows comparisons of time-series of temperature and the TEM thermodynamic terms in the TT from January 1996 to December 1999. The TT temperature in the experiment using observed SST (EXP3) has a cold bias of about 2.5 K. The variations in TT temperature in EXP3 are consistent with those of ERA-Interim and ERA-40, except for high temperatures during the boreal summer of 1999 and low temperature during the boreal summer of 1996. In January 1998, when El Niño reached its peak, the TT temperature is higher than that in January of other years (1996, 1997, and 1999). This feature is seen in between 100 and 80 hPa of all the datasets including EXP3. At the same time, divergence of the vertical eddy heat flux is reduced in amplitude, which acts to increase TT temperature. Also in January of 1998, for ERA-Interim and ERA40, divergence of the vertical eddy heat flux leads to an increase in TT temperature. Despite these similarities among the three data sets, there exist large differences in vertical advection until 1998. The large amplitudes of vertical advection and diabatic heating in ERA40 are seen until August 1998, because in ERA 40 upward flow around the TT and B–D circulation are overestimated; for example, based on the chemical transport model, *Schoeberl et al.* [2003] and *Monge-Sanz et al.* [2007] suggested that the strength of B–D circulation is overestimated in ERA40. These amplitudes showed a marked reduction following the launch of NOAA-15 in August of

1998, which is equipped with the high vertical-resolution Advanced Microwave Sounding Unit (AMSU-A).

Figure 2.12 shows differences in the vertical eddy heat flux, vertical velocity, and potential temperature between EXP3 and CTR for January 1998. The characteristics of the results obtained from EXP3 are similar to those obtained from 0.5SST' (Fig. 2.8). In particular, in both the equatorial western Pacific and the area south of the equatorial eastern Pacific, the stationary part of the vertical eddy heat flux is similar to the result obtained from 0.5SST'.

Figure 2.13 shows similar fields to those in Fig. 2.12, but calculated from ERA-Interim. Compared with EXP3, the stationary part of the vertical eddy heat flux in ERA-Interim has a broader and weaker positive region around the equatorial western Pacific. Consequently, the stationary vertical eddy heat flux between 10°S and 10°N in EXP3 has a similar thermodynamic effect on the TT to that in ERA-Interim.

The positive anomalies in the stationary part of the vertical eddy heat flux in both EXP3 and ERA-Interim decay upward to 70 hPa, and the reduction in divergence of the vertical eddy heat flux leads to an increase in TT temperature. Consequently, the TT temperature in January 1998 is warmer than that in January of any other year. The EXP3 results for the 1997/98 El Niño event are in good agreement with the results of ERA-Interim and ERA-40, in terms of vertical eddy heat flux and TT temperature. These findings indicate that TT temperature change due to vertical eddy heat flux is not just a feature of the numerical model: it occurs in the real world, associated with the changing longitudinal gradient of tropical SST.

2.9. Concluding remarks

The main aim of this investigation was to study the response of TT temperature to various patterns of tropical SSTs. Four different patterns of tropical SSTs were used in a numerical model as the boundary conditions. The response of the TT was discussed based on the results of numerical experiments and an analysis of the ERA-Interim and ERA40 data sets. Based on these analyses, we arrived at the following conclusions.

- (1) With increasing (decreasing) longitudinal gradient of tropical SST, TT temperature and tropical upper-troposphere temperature decrease and increase (increase and decrease), respectively, due to strengthening (weakening) of the

vertical eddy heat flux. Divergence of the vertical eddy heat flux around the TT decreases with weakening the Matsuno–Gill pattern.

(2) Enhanced longitudinal gradient of tropical SST results in intensification of circulation (with ascent centered on the equator) and poleward meridional flow around the TT. This circulation weakens with a decrease in the gradient of SST.

(3) With increasing mean tropical SST, the annual-mean TT temperature increases due to diabatic heating; however, with decreasing mean tropical SST, the annual-mean TT temperature is unchanged because of counteracting thermodynamic effects. In both cases, change in the annual cycle of TT temperature shows poor agreement with vertical advection and convergence of the vertical eddy heat flux.

(4) Vertical eddy heat flux caused by a reduction of the longitudinal gradient of tropical SST due to El Niño (1997/98) results in an increase in TT temperature in the results of ERA-Interim and ERA40, and in the output of the numerical experiment using observed SST

(5) In terms of climatological seasonal variation, our experimental results are consistent with the findings of *Kerr-Munslow and Norton* [2006]. Variations in seasonal TT temperature are controlled mainly by the vertical advection induced by equatorial waves; however, interannual variations in TT temperature cannot be explained solely in terms of vertical advection.

The fifth term in equation (2.4), which represents convergence of the vertical eddy heat flux, has been largely neglected in previous studies, such as those of seasonal variations in TT temperature; however, the results of the present study demonstrate that this term makes a major contribution to interannual variations in TT temperature.

The localized deep convection around the tropical western Pacific enhances the ascending motion; thus, $w' > 0$. Interestingly, potential temperature perturbations around the tropical western Pacific at 100 hPa are negative ($\theta' < 0$); consequently, the vertical motion generates a negative eddy heat flux ($\overline{w'\theta'} < 0$) that acts to reduce the temperature in the TT due to the upward decay of this pattern. Figure 2.10 shows a schematic picture of this special pattern.

In adiabatic motion which follows isentropic surface, the vertical eddy heat flux must be zero because w' and θ' are out of phase. However, considering the longwave

radiative cooling and vertical flow which thermodynamically balances with diabatic heating, the vertical eddy heat flux can be nonzero value. In the region where low potential temperature part $\theta' < 0$ occurs, there are radiative heating part $Q' = -\theta' / \tau > 0$ under assumption of Newtonian cooling and upward flow part which is balanced with radiative heating $w' = Q' / \theta_z > 0$. In this case, w' and θ' are in phase (because of $w'\theta' = Q'\theta' / \theta_z = -\theta'^2 / (\tau\theta_z)$).

With increasing longitudinal gradient of tropical SST, localized convection develops around the tropical western Pacific, exciting tropical waves and enhancing the Matsuno–Gill pattern. Consequently, divergence of the vertical eddy heat flux is intensified around the TT, leading in turn to a decrease in TT temperature. However, with a reduction in the longitudinal gradient of tropical SST, as occurs during an El Niño event, the localized deep convection weakens around the tropical western Pacific, meaning that divergence of the vertical eddy heat flux is reduced around the TT, leading in turn to an increase in TT temperature.

These results are similar to those reported by *Hatsushika and Yamazaki* [2001], who found that between December and February in El Niño years the cold tropopause region becomes zonally elongated and meridionally narrow, and that the ascending area shifts eastward and weakens around the TT.

When the mean tropical SST increases or decreases, the TT temperature is controlled not only by vertical advection but also diabatic heating. It is highly possible that long-wave radiative absorption shows an increase (decrease) around the TT due to increasing (decreasing) tropical SST. In addition, TT temperature increases (decreases) with lowering (rising) of the cloud top height [*Hartmann et al.*, 2001]. Lowering (rising) of the cloud top height results in high (low) cloud-top temperature, and consequently an intensification (reduction) of outgoing long-wave radiation from the cloud top. Additional research is required to explain the effect of diabatic heating on TT temperature.

This chapter demonstrated the importance of the vertical eddy heat flux on interannual variations in TT temperature. The vertical eddy heat flux is likely to play a role in global warming and century-scale variations around the TT, as many climate models predict an El Niño-like climate in the future and the weakening of Walker circulation [*Vecchi et al.*, 2006; *Yamaguchi and Noda*, 2006].

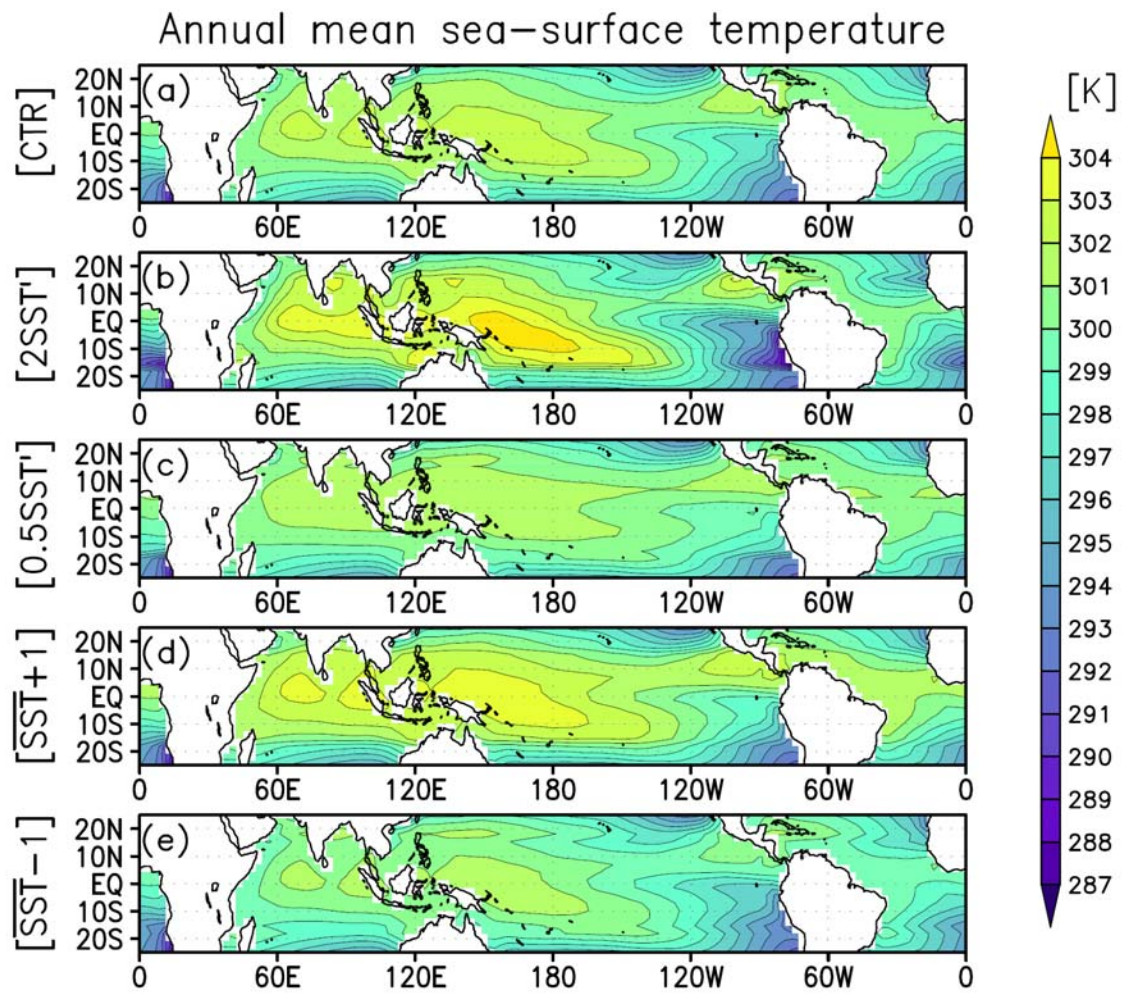


Figure 2.1. Annual-mean sea surface temperature [K] fields used for AGCM experiments. (a) CTR, (b) $2SST'$, (c) $0.5SST'$, (d) $\overline{SST} + 1$, (e) $\overline{SST} - 1$.

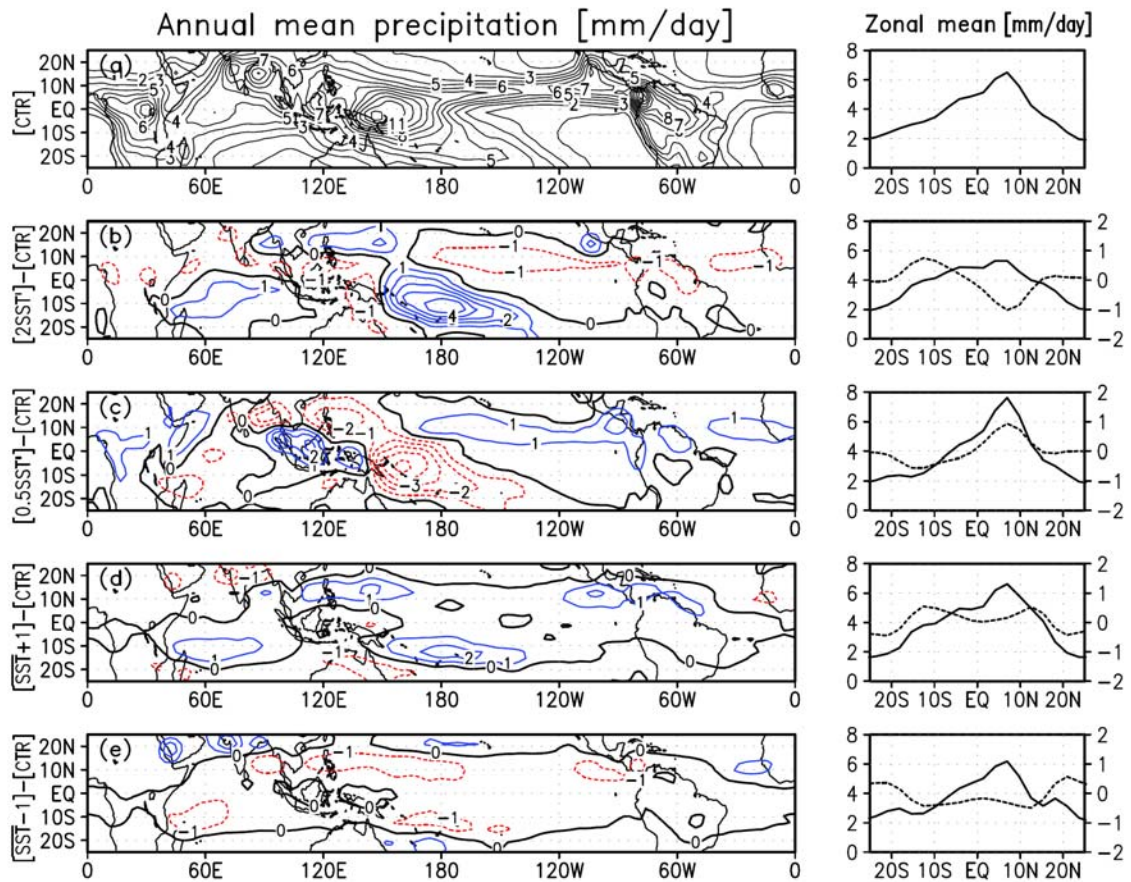


Figure 2.2. (Left) Annual-mean precipitation field in (a) CTR and the differences between CTR and (b) $2SST'$, (c) $0.5SST'$, (d) $\overline{SST} + 1$, and (e) $\overline{SST} - 1$. (Right) Solid lines indicate annual-mean zonal-mean precipitation in each experiment [left axis], and dashed lines indicate the difference from CTR [right axis].

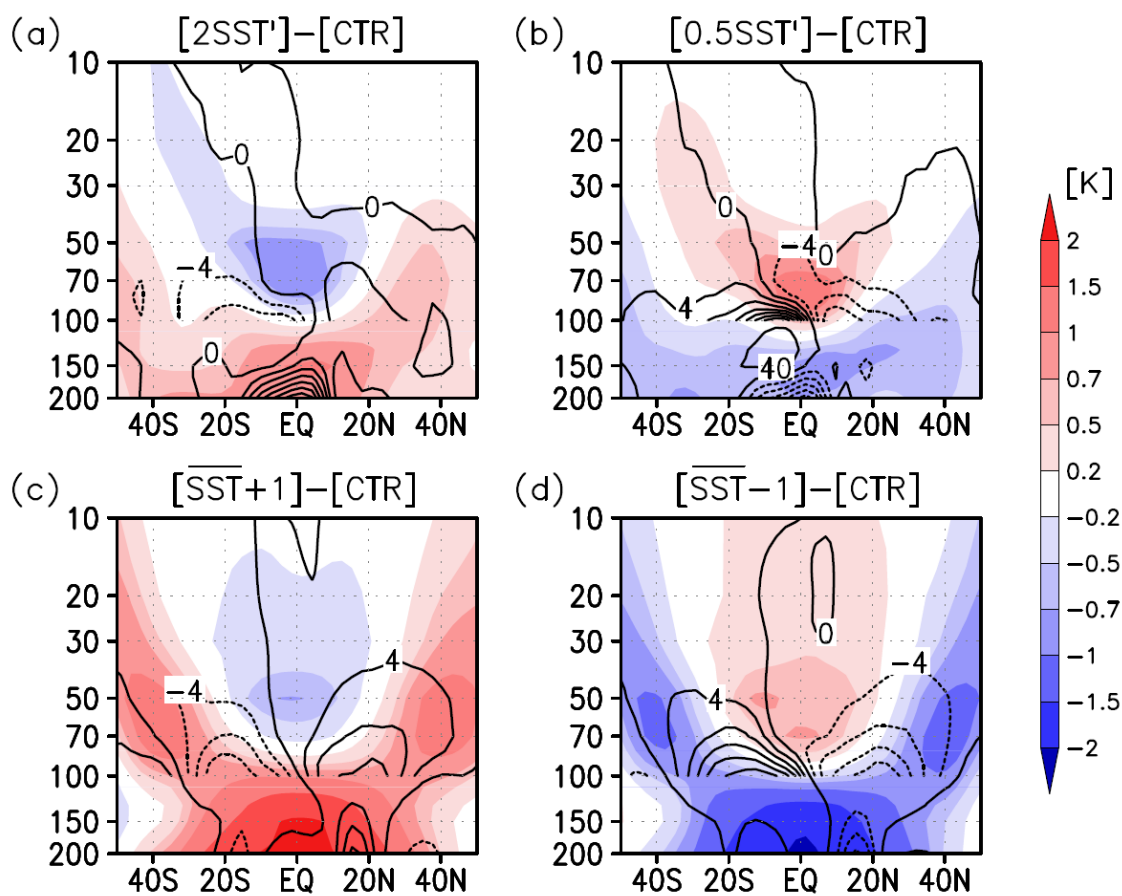


Figure 2.3. Annual-mean cross-sections of differences from CTR in zonal-mean temperature [K] (color shadings) and the residual mean stream function [$\text{kg m}^{-1}\text{s}^{-1}$] (contours; positive values mean counterclockwise flow) for (a) $2\text{SST}'$, (b) $0.5\text{SST}'$, (c) $\overline{\text{SST}+1}$, and (d) $\overline{\text{SST}-1}$. The contour interval is $4 \text{ kg m}^{-1}\text{s}^{-1}$ above 100 hPa and $40 \text{ kg m}^{-1}\text{s}^{-1}$ below 100 hPa.

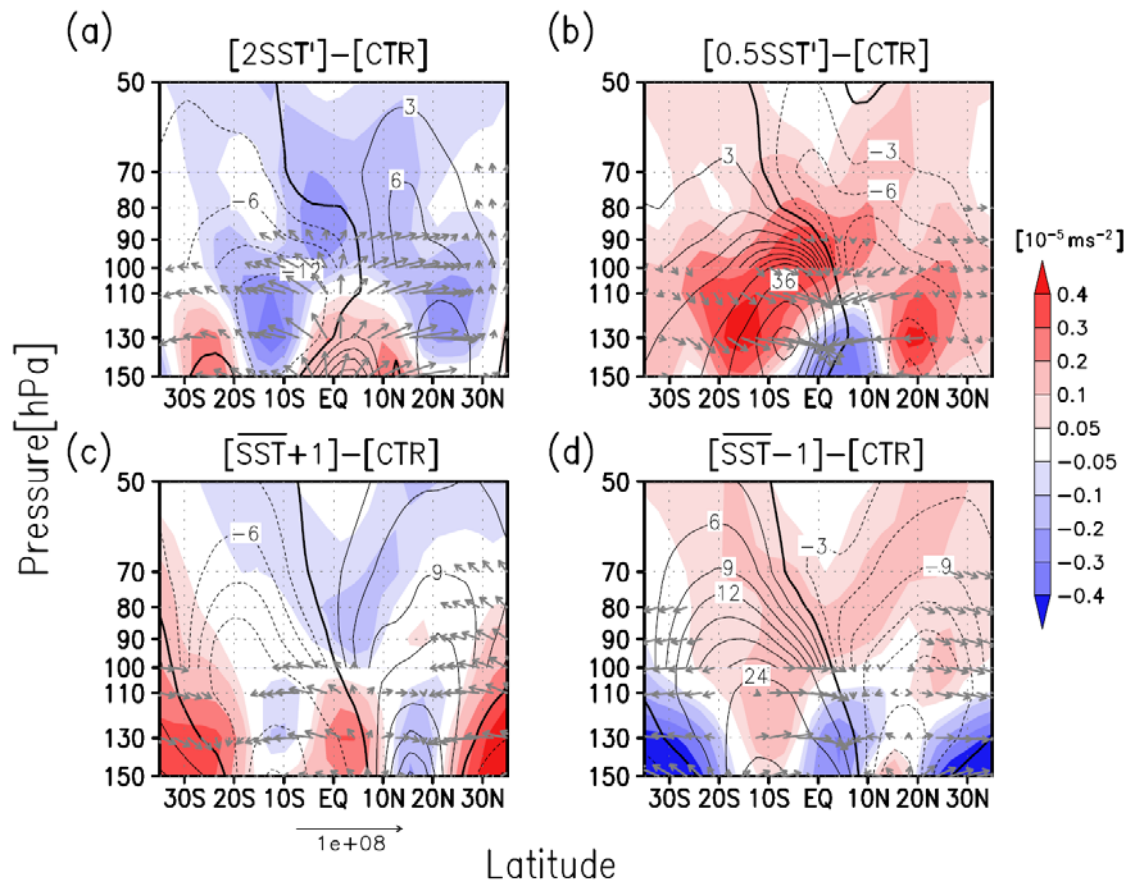


Figure 2.4. Annual-mean cross-sections of differences from CTR of the residual mean stream function [$\text{kg m}^{-1} \text{s}^{-1}$] (contours; positive values mean counterclockwise flow), the Eliassen–Palm flux [$\text{m}^2 \text{s}^{-2}$] (arrows), and EP flux divergence [m s^{-2}] (color shadings) for (a) $2SST'$, (b) $0.5SST'$, (c) $\overline{SST} + 1$, and (d) $\overline{SST} - 1$. The contour interval is 3 $\text{kg m}^{-1} \text{s}^{-1}$ above 100 hPa and 12 $\text{kg m}^{-1} \text{s}^{-1}$ below 100 hPa. The vertical component of the EP flux is multiplied by 200.

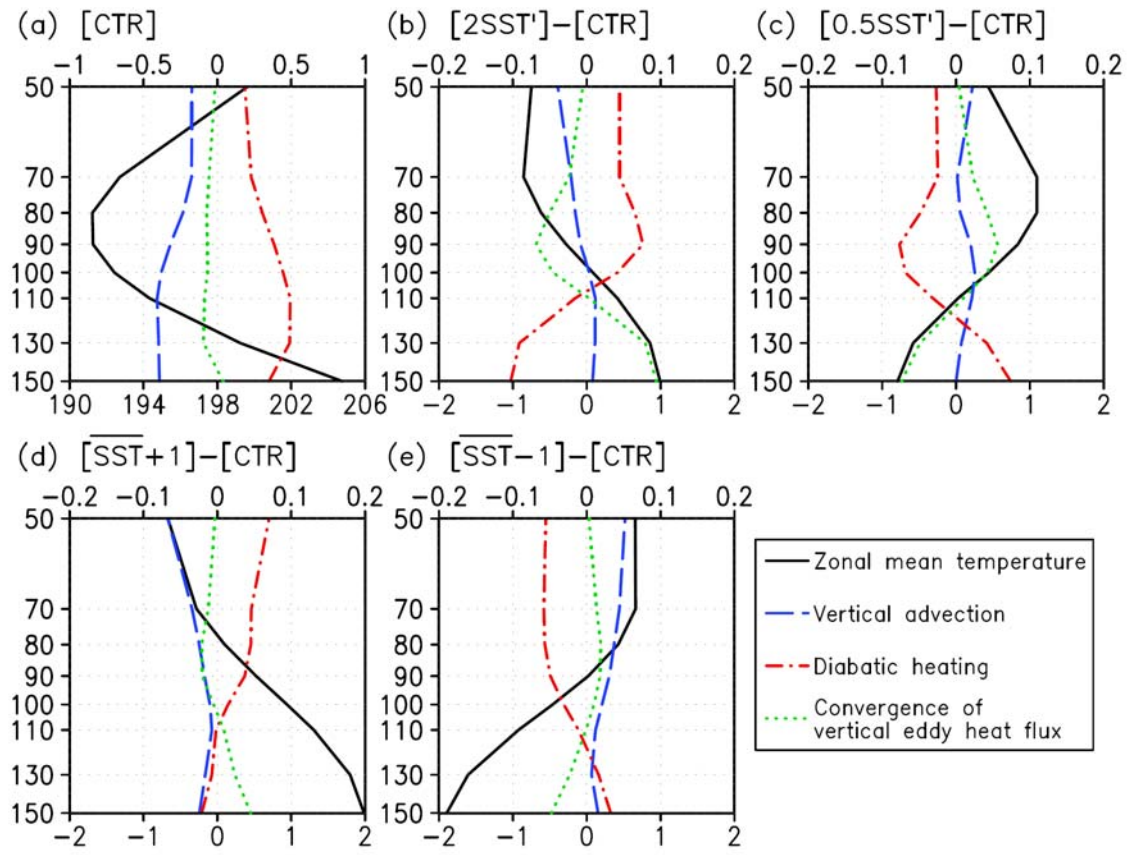


Figure 2.5. Comparison of annual-mean vertical profiles of zonal-mean temperature [lower axis; K] and terms in the TEM thermodynamic equation [upper axis; K/day] averaged over the tropics (10°S – 10°N) in (a) CTR and in the difference from CTR of (b) $2\overline{SST}'$, (c) $0.5\overline{SST}'$, (d) $\overline{SST} + 1$, and (e) $\overline{SST} - 1$.

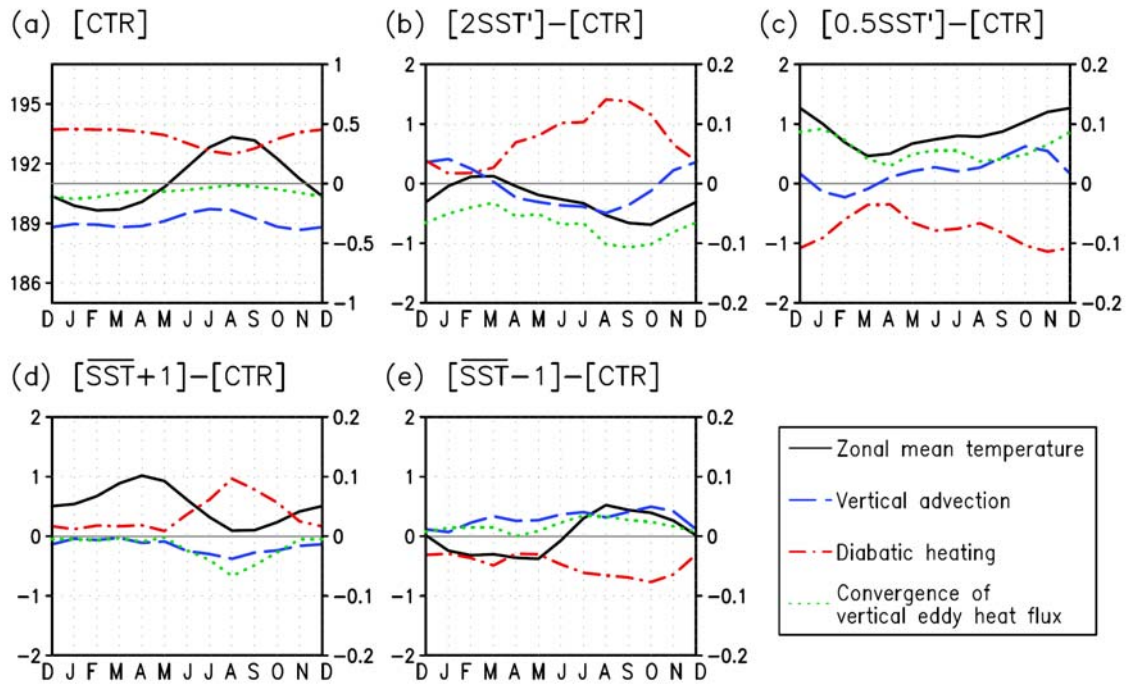


Figure 2.6. Annual cycles of zonal-mean temperature [left axis; K] and terms in the TEM thermodynamic equation [right axis; K/day] (the plotted terms are the same as those in Figure 5) in (a) CTR and in the difference from CTR of (b) $2SST'$, (c) $0.5SST'$, (d) $\overline{SST} + 1$, and (e) $\overline{SST} - 1$ averaged over the tropics (10°S – 10°N) at 90 hPa.

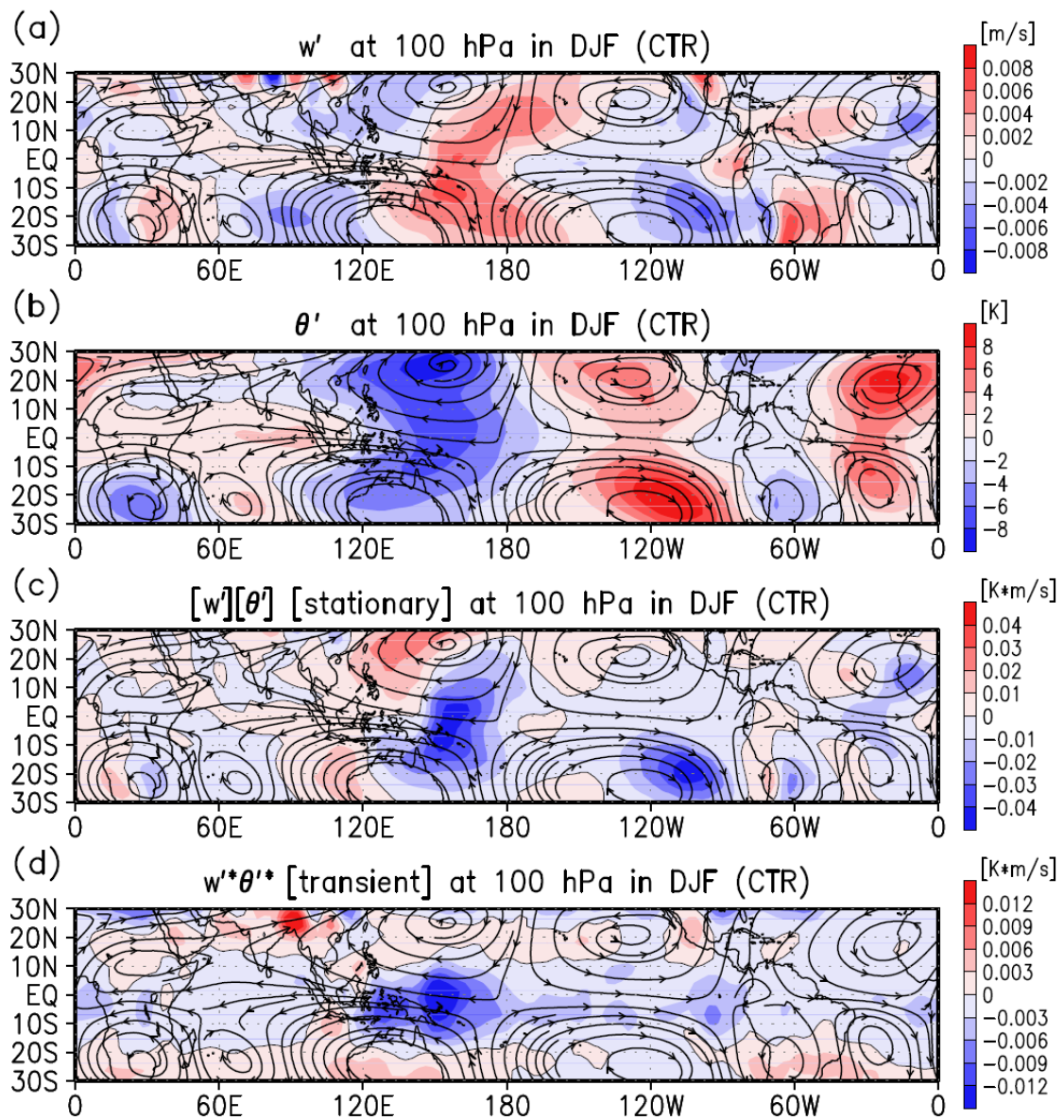


Figure 2.7. Horizontal fields of departures from the zonal mean of stream functions (black arrowed contours shown qualitatively): (a) vertical velocity w' , (b) potential temperature θ' , (c) stationary part of the vertical eddy heat flux $[w][\theta']$, and (d) transient part of the vertical eddy heat flux $w'^*\theta'^*$ in CTR for the period December–February at 100 hPa.

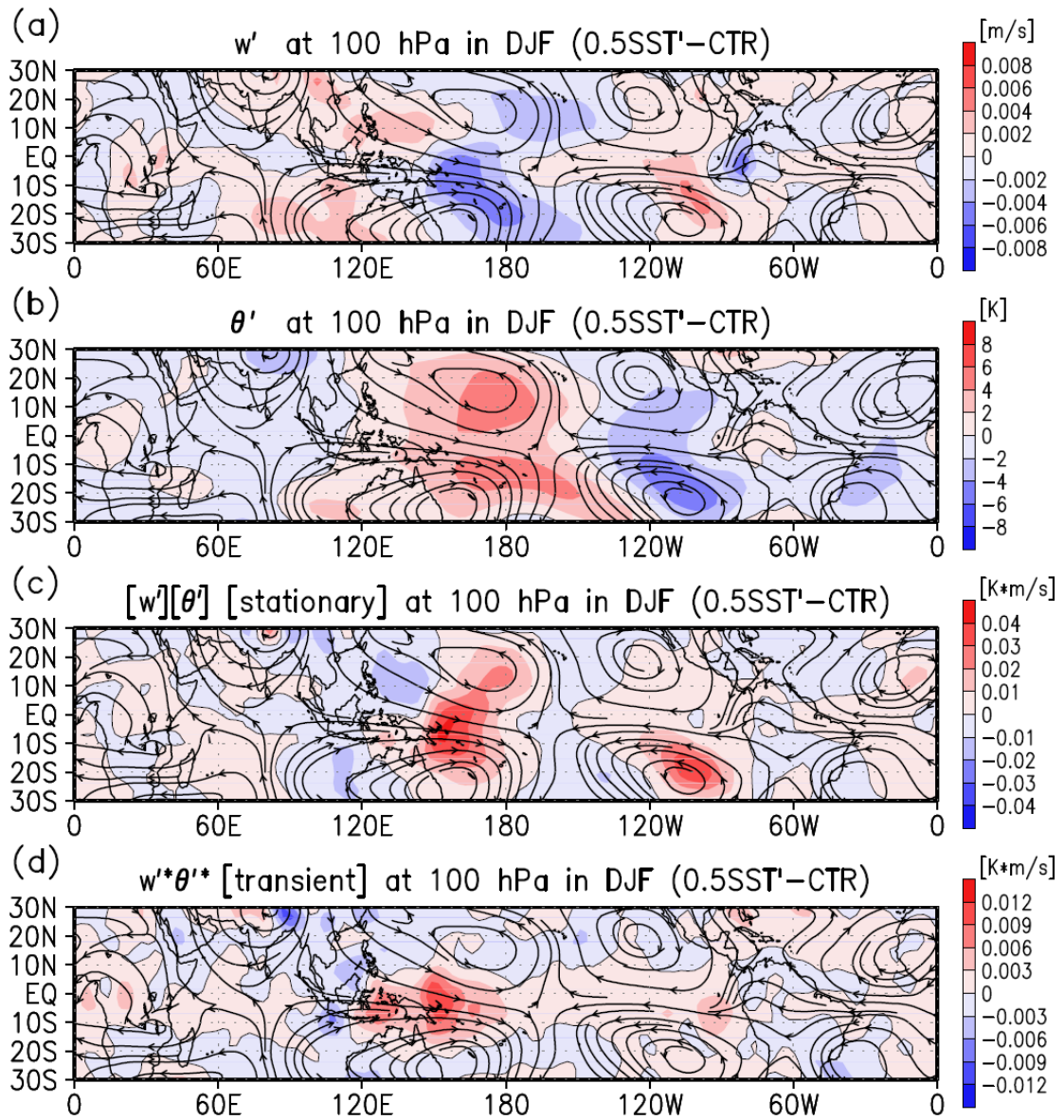


Figure 2.8 As for Figure 2.7, but for differences in $0.5SST'$ from CTR.

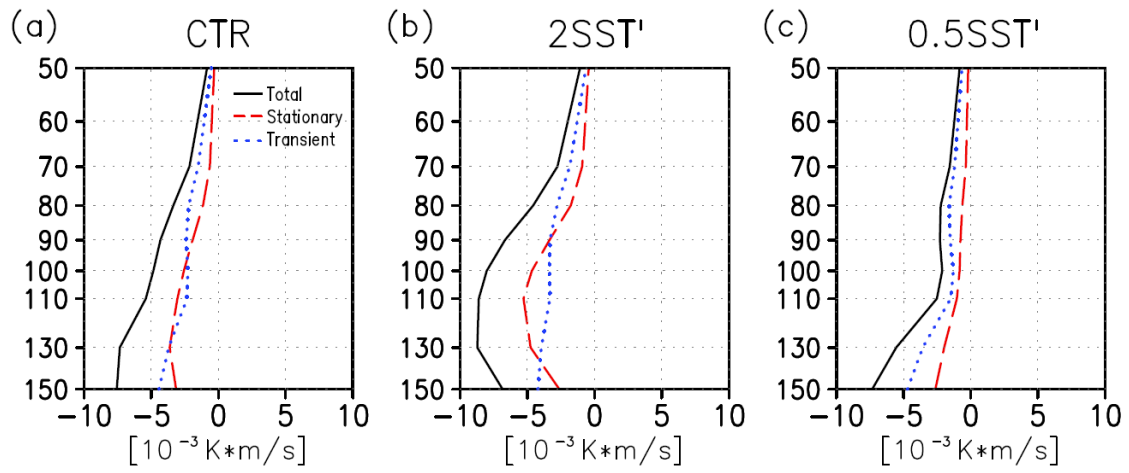


Figure 2.9. Vertical profiles of annual-mean zonal-mean vertical eddy heat flux averaged over the tropics (10°S – 10°N) between 50 and 150 hPa in (a) CTR, (b) 2SST', and (c) 0.5SST'. Solid lines indicate the total value of the vertical eddy heat flux, dashed lines are the stationary part of the vertical eddy heat flux, and dotted lines are the transient part of the vertical eddy heat flux.

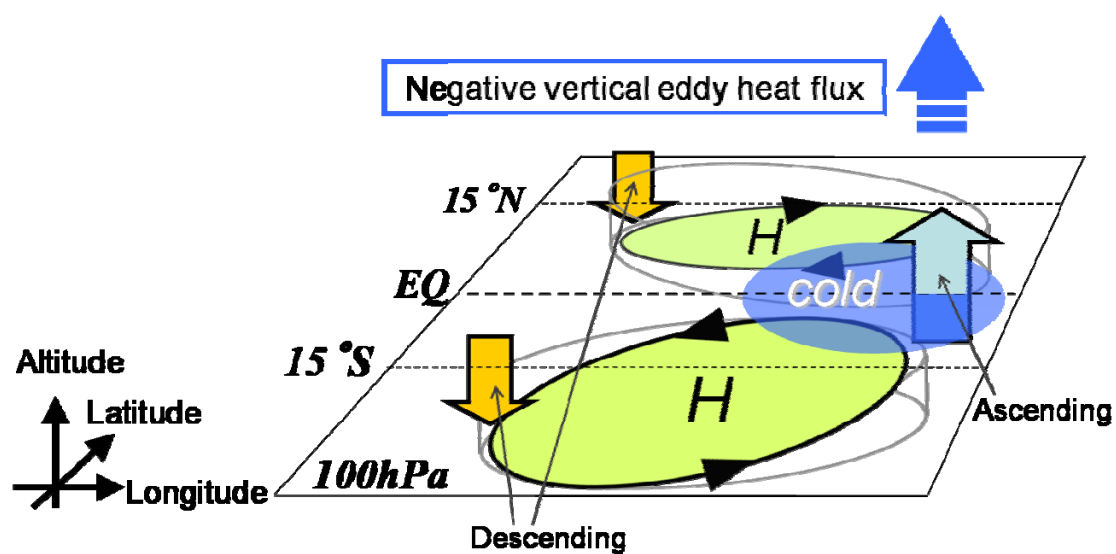


Figure 2.10. Schematic showing typical wave activity in the tropical western Pacific at 100 hPa. H indicates a high-pressure anomaly, the dark-grey oval is a cold anomaly, the upward arrow is an ascending anomaly, and the downward arrow is a descending anomaly. These cold and ascending anomalies generate negative vertical eddy heat flux.

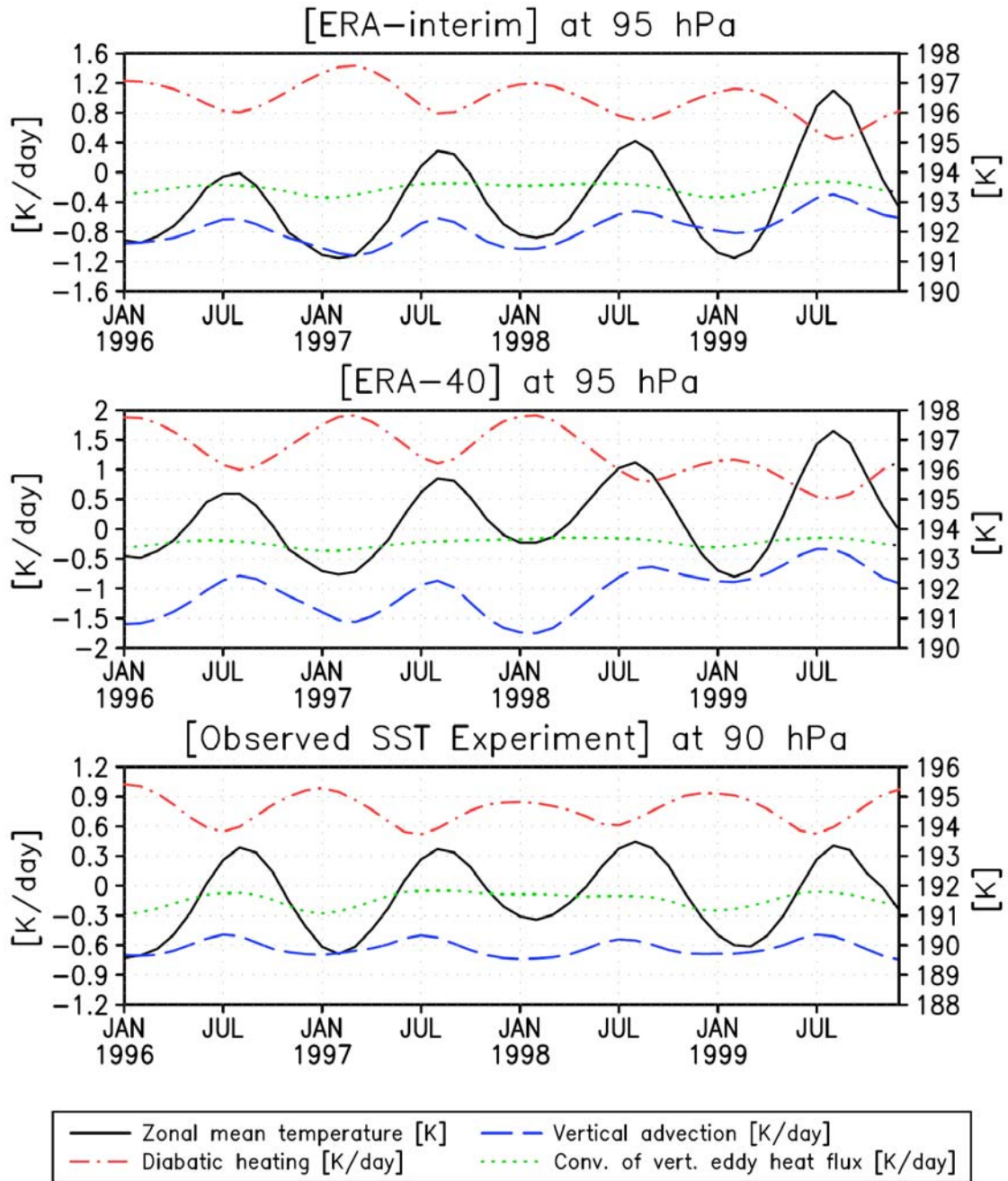


Figure 2.11. Comparison of the time series of zonal-mean temperature [K] and terms in the TEM thermodynamic equation [K/day] (the plotted terms are the same as those in Figures 2.5 and 2.6) averaged over the tropics (10°S – 10°N). (Top) ERA-Interim at 95 hPa. (Middle) ERA-40 at 95 hPa. (Bottom) Observed SST Experiment at 90 hPa.

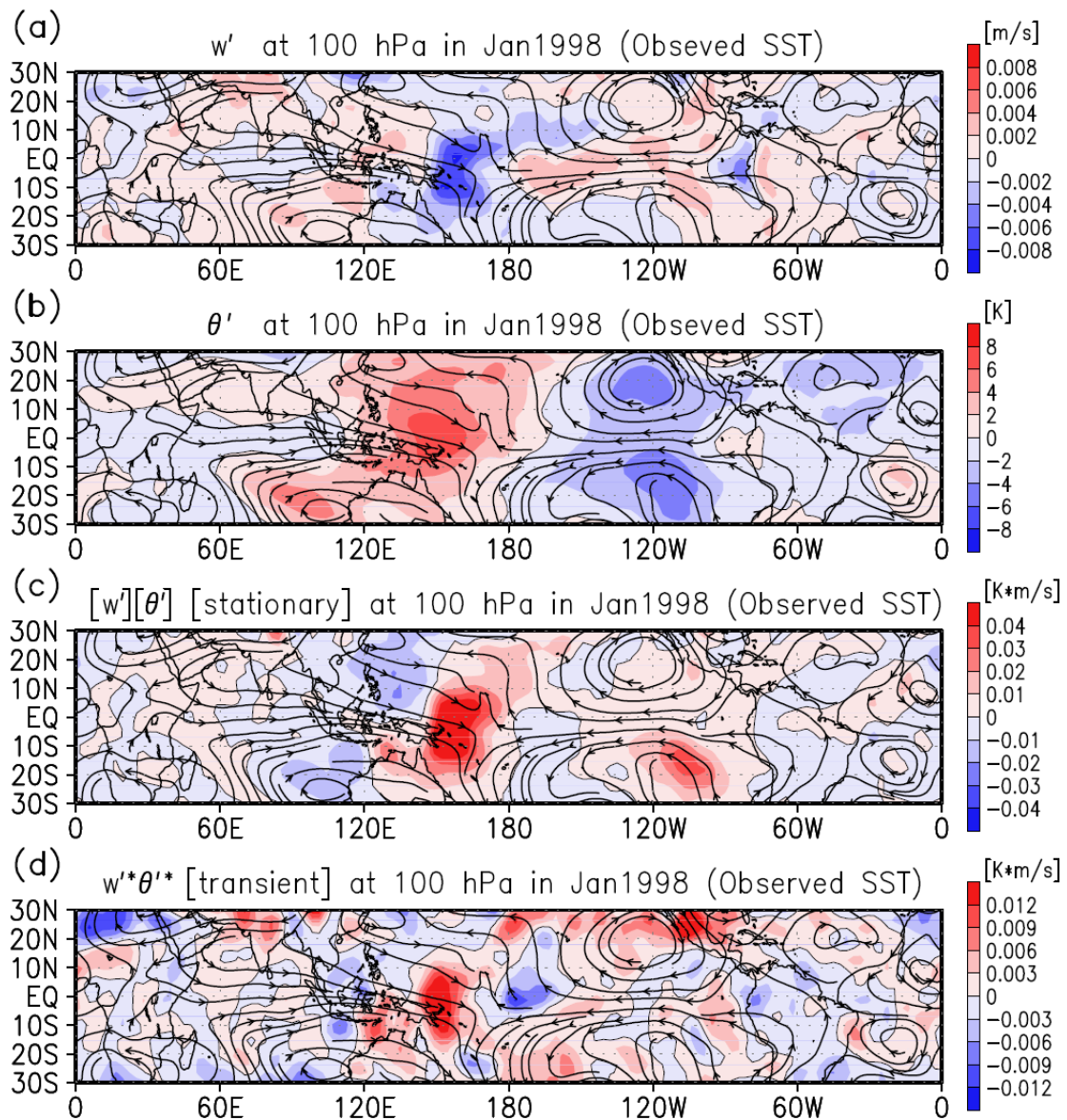


Figure 2.12. Horizontal field differences in departures from the zonal mean of stream functions (black arrowed contours shown qualitatively): (a) vertical velocity w' , (b) potential temperature θ' , (c) stationary part of the vertical eddy heat flux $[w'][\theta']$, and (d) transient part of the vertical eddy heat flux $w'^* \theta'^*$ in the Observed SST experiment from climatological means (CTR in January) for January 1998 at 100 hPa.

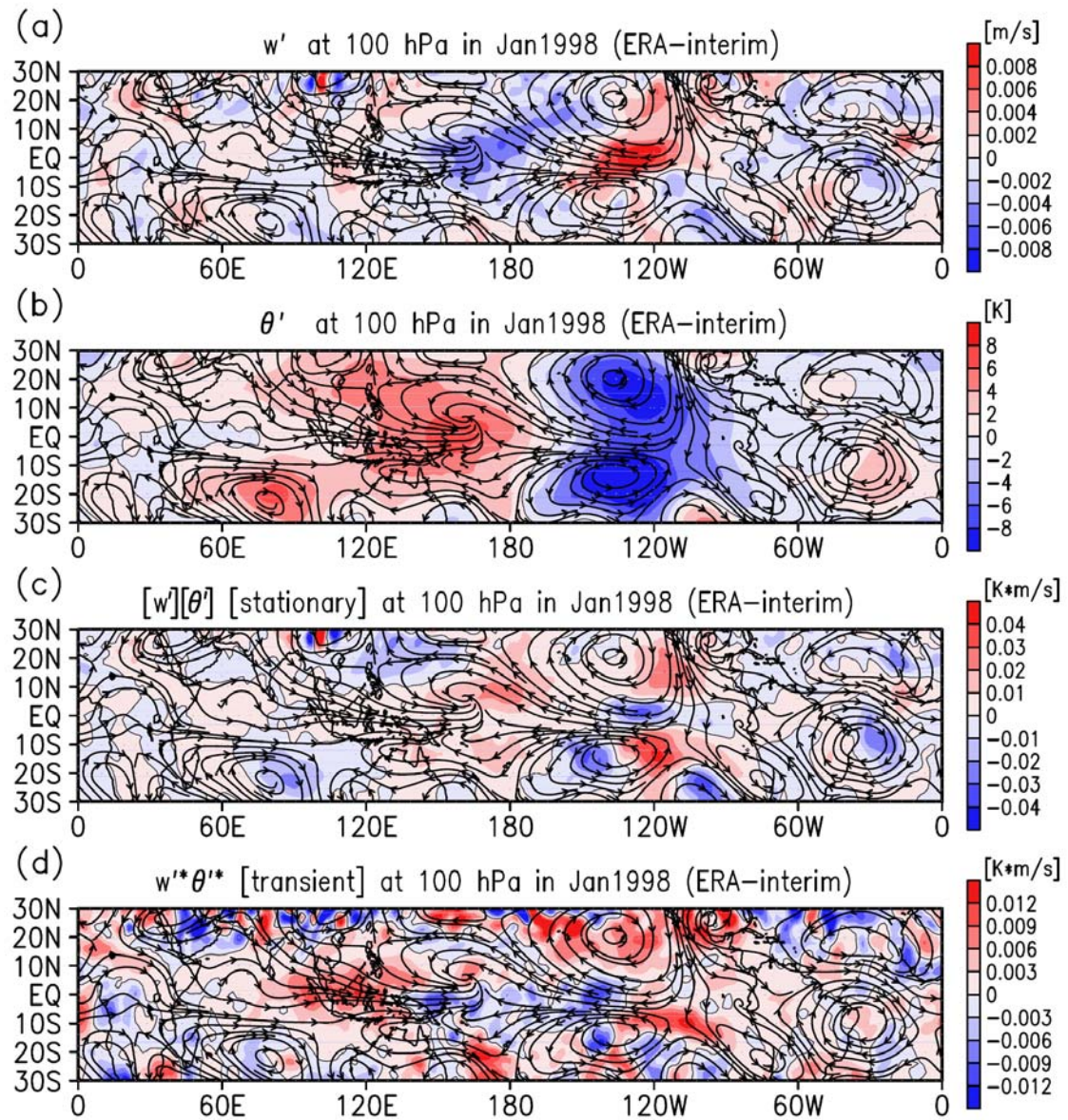


Figure 2.13. As for Figure 2.12, but calculated from ERA-Interim.

Chapter 3| Tropical cooling in the case of stratospheric sudden warming in January 2009: focus on the tropical tropopause layer

3.1. Introduction

The tropical tropopause layer (TTL; defined here as the tropics between 150 and 70 hPa) is an important region in stratospheric physics and chemistry because of its role as a gateway to the stratosphere. The coldness in the TTL, especially in the cold-point tropopause (which is the coldest region in the TTL), controls the large-scale distribution of water vapor in the stratosphere by dehydration of the air entering the stratosphere [Holton and Gettleman, 2001; Hatsushika and Yamazaki, 2003; Fueglistaler *et al.*, 2005]. Thus, spatial and temporal variations in the TTL have been examined in many previous studies [e.g., Highwood and Hoskins, 1998; Fueglistaler *et al.*, 2009a].

The TTL temperature is affected by processes in the troposphere and in the stratosphere, especially through the circulation. Mean stratospheric poleward flow, which is driven by the dissipation of vertically propagating Rossby and gravity waves, induces upwelling in the tropics and downwelling in the extratropics to conserve mass (the so-called Brewer–Dobson circulation) [Yulaeva *et al.*, 1994; Haynes *et al.*, 1991; Plumb and Eluszkiewicz, 1999]. The zonal mean temperature in the TTL is considered to be controlled by wave forcing of the extratropical stratosphere, which is referred to as the “stratospheric pump” [Holton *et al.*, 1995]. Tropical waves also drive a residual circulation in the TTL. Kerr-Munslow and Norton [2006] suggested that dissipation of quasi-stationary waves in the upper troposphere and lower stratosphere generated by deep convection induces upwelling in the TTL, resulting in a reduction in TTL temperature. Based on this result and model calculations, Norton [2006] reported that seasonally varying tropical Rossby waves generate an annual cycle in upwelling and therefore also in temperature. As an effect other than upwelling, Yoshida and Yamazaki [2010] suggested vertical convergence of vertical heat flux $\overline{w'\theta'}$ (see Section 3.2.2 for detail; referred to as “vertical eddy heat flux” in Chapter 2), which is closely tied to

tropical convection structure, plays a role in heat budget in the TTL.

Stratospheric sudden warming (SSW) is one of the most dramatic phenomena in the stratospheric atmosphere. The strong planetary-scale waves induce violent meridional circulation in the winter hemisphere of the stratosphere [Matsuno, 1971]. The relationship between the tropical troposphere and the SSW has been discussed in several studies. *Kodera* [2006] suggested that meridional circulation change associated with the SSW in Arctic regions produces a lower temperature in the equatorial lower stratosphere, which leads to a seesaw pattern of convective activity near the equatorial Southern Hemisphere, but suppression of convective activity in the tropics of the Northern Hemisphere. *Kuroda* [2008] suggested that tropical convection tends to be enhanced during SSW due to nonuniform meridional propagation of the planetary wave around the tropopause, associated with upward propagation of the planetary wave to the stratosphere. These phenomena may influence the TTL.

A strong SSW event occurred in the second half of January 2009. *Manney et al.* [2009] provided an overview of dynamics and transport during the 2009 SSW, based on observations by the Aura Microwave Limb Sounder (AMLS). The occurrence of very large wave-2 during the SSW in 2009 is consistent with vortex split. *Harada et al.* [2010] reported that the total amount of upward Eliassen–Palm (EP) flux for wave 2 was the strongest since the boreal winter of 1978/79, and the remarkable development of the upper tropospheric ridge over Alaska played an important role in the onset of SSW during January 2009.

The aim of this paper is to reveal how various factors (e.g., wave activity in the stratosphere, tropical convection, and meridional propagation of waves in the northern extratropics) affected the TTL in the case of the SSW event in January 2009. The remainder of this paper is organized as follows. Section 3.2 provides a description of the dataset and analysis methods. Section 3.3 shows the temperature structures as observed in the period of interest, and the associated thermodynamic budget calculated from ERA-Interim data. The nature of the forcing that causes the circulation in the TTL is evaluated in Section 3.4, and the structure of wave activity is described in Section 3.5. In Section 3.6, we consider the questions that arose in the preceding sections. Finally, the main results are summarized in Section 3.7.

3.2. Data and methods

3.2.1. Data

We used a 6-hourly dataset of European Centre for Medium-Range Weather Forecasts (ECMWF) ERA-Interim [Simmons *et al.*, 2006; Uppala *et al.*, 2008]. The period of analysis was from 1 December 2008 to 31 March 2009. Interpolated outgoing long-wave radiation (OLR) data were obtained from the Climate Diagnostic Center (CDC) of the National Oceanic and Atmospheric Administration (NOAA) [Liebmann and Smith, 1996]. The data presented in this paper are smoothed using a 3-day running average, unless stated otherwise.

3.2.2. Transformed Eulerian Mean equations

To diagnose the zonal mean thermodynamic balance, quantitative analysis was performed by the transformed Eulerian mean (TEM) equations in log-pressure coordinates [see Andrews *et al.*, 1987]:

$$\frac{\partial \bar{\theta}}{\partial t} = -\bar{v}^* \frac{\partial \bar{\theta}}{a \partial \phi} - \bar{w}^* \frac{\partial \bar{\theta}}{\partial z} + \bar{Q} - \frac{1}{\rho_0} \frac{\partial}{\partial z} \left(\rho_0 \overline{v' \theta'} \frac{\bar{\theta}_\phi}{a \theta_z} \right) - \frac{1}{\rho_0} \frac{\partial}{\partial z} \left(\rho_0 \overline{w' \theta'} \right); \quad (3.1)$$

$$\bar{v}^* \equiv \bar{v} - \frac{1}{\rho_0} \frac{\partial}{\partial z} \left(\rho_0 \frac{\overline{v' \theta'}}{\theta_z} \right), \quad \bar{w}^* \equiv \bar{w} + \frac{1}{a \cos \phi} \frac{\partial}{\partial \phi} \left(\cos \phi \frac{\overline{v' \theta'}}{\theta_z} \right), \quad (3.2)$$

where the overbar denotes the zonal mean, the prime is the departure from the zonal mean, subscripts denotes partial differentiation, a is the radius of Earth, θ is potential temperature, ϕ is latitude, $\rho_0 = \rho_s \exp(-z/H)$ is the reference density, $H = 7050$ m is the constant scale height, \bar{Q} is diabatic heating, \bar{v} is the residual mean meridional wind, and \bar{w}^* is the residual mean vertical wind. The diabatic heating term is calculated from the residual in equation (3.1). The second term on the right-hand-side is vertical advection, and the last (fifth) term is vertical convergence of the vertical heat flux. The first and fourth terms on the right-hand-side can be neglected because they are minor compared with the other terms.

The EP flux was analyzed to evaluate eddy forcing in zonal mean circulation [see Andrews *et al.*, 1987]:

$$\mathbf{F} \equiv (0, F_1^{(\phi)} + F_2^{(\phi)}, F_1^{(z)} + F_2^{(z)}), \quad (3.3)$$

$$F_1^{(\phi)} \equiv \rho_0 a \cos \phi \frac{\partial \bar{u}}{\partial z} \frac{\overline{v'\theta'}}{\bar{\theta}_z}, \quad F_2^{(\phi)} \equiv -\rho_0 a \cos \phi \overline{u'v'}, \quad (3.4)$$

$$F_1^{(z)} \equiv \rho_0 a \cos \phi \bar{\zeta} \frac{\overline{v'\theta'}}{\bar{\theta}_z}, \quad F_2^{(z)} \equiv -\rho_0 a \cos \phi \overline{u'w'}, \quad (3.5)$$

where $\bar{\zeta} = f - (a \cos \phi)^{-1} (\bar{u} \cos \phi)_\phi$ is the zonal mean absolute vorticity, f is the Coriolis parameter, and \mathbf{F} is EP flux. The total eddy forcing is represented by the divergence/convergence (westerly/easterly acceleration) of the EP flux.

3.2.3. Wave activity flux

To examine the behavior of the three-dimensional wave activity associated with the circulation in the midlatitude and tropics, we calculated the wave activity flux vector (\mathbf{F}_s vector) for quasi-geostrophic disturbance on the β plane, as proposed by *Plumb* [1985].

The \mathbf{F}_s vector can be given by

$$\mathbf{F}_s = \begin{pmatrix} F_s^{(\lambda)} \\ F_s^{(\phi)} \\ F_s^{(z)} \end{pmatrix} = p \cos \phi \begin{pmatrix} v'^2 - \frac{1}{2\Omega a \sin 2\phi} \frac{\partial(v'\Phi')}{\partial \lambda} \\ -u'v' + \frac{1}{2\Omega a \sin 2\phi} \frac{\partial(u'\Phi')}{\partial \lambda} \\ \frac{2\Omega \sin \phi}{S} \left[v'T' - \frac{1}{2\Omega a \sin 2\phi} \frac{\partial(T'\Phi')}{\partial \lambda} \right] \end{pmatrix}, \quad (3.6)$$

where $S = \partial \hat{T} / \partial z + \kappa \hat{T} / H$ is the static stability (the caret indicates the regional average over the area between 15°N and 75°N), p = pressure/1000 hPa, and Ω is the Earth's rotation rate. Longitudinal integration of \mathbf{F}_s corresponds to the EP flux for quasi-geostrophic motions on the midlatitude β plane.

3.2.4. Diagnosis of upwelling

To examine the response of residual mean circulation to external forcings, such as wave forcing and diabatic heating, the residual mean vertical wind was estimated by a diagnostic model using simplified TEM equations;

$$\frac{\partial \bar{u}}{\partial t} - 2\Omega\mu\bar{v}^* = \bar{F} + \bar{X}, \quad (3.7)$$

$$2\Omega\mu\bar{u} = -\frac{1}{a}\sqrt{1-\mu^2}\frac{\partial\bar{\Phi}}{\partial\mu}, \quad (3.8)$$

$$\frac{\partial\bar{\Phi}}{\partial p} = -\frac{R\bar{T}}{p}, \quad (3.9)$$

$$\frac{1}{a}\frac{\partial\sqrt{1-\mu^2}\bar{v}^*}{\partial\mu} + \frac{\partial\bar{\omega}^*}{\partial p} = 0, \quad (3.10)$$

$$\frac{\partial\bar{T}}{\partial t} - \Gamma\bar{\omega}^* = \bar{Q} + \bar{E}, \quad (3.11)$$

where $\bar{\omega}^*$ is the residual mean vertical wind in pressure coordinates, \bar{F} is divergence of the EP flux, \bar{X} is eastward residual forcing, \bar{E} is convergence of the vertical eddy heat flux, $\Gamma = -\partial T_0 / \partial p + \kappa T_0 / p$ is static stability for reference temperature, R is the ideal gas constant, and μ is sine latitude. The eastward residual forcing term is calculated from the residual in equation (3.7). Except for the terms of the residual mean circulation, EP flux divergence, and vertical convergence of vertical heat flux, equations (3.7)–(3.11) are essentially the same as those used by *Plumb* [1982], *Haynes and Shepherd* [1989], and *Kuroda and Kodera* [2004].

We can obtain a diagnostic equation for $\bar{\omega}^*$ by using equations (3.7)–(3.11), as follows:

$$\begin{aligned} & \frac{\partial}{\partial\mu} \left[\frac{1-\mu^2}{\mu^2} \frac{\partial\bar{\omega}^*}{\partial\mu} \right] + \frac{4\Omega^2 a^2 p}{R\Gamma} \frac{\partial^2\bar{\omega}^*}{\partial p^2} \\ &= \frac{2\Omega a p}{R\Gamma} \frac{\partial^2}{\partial\mu\partial p} \left[\frac{\sqrt{1-\mu^2}}{\mu} (\bar{F} + \bar{X}) \right] - \frac{1}{\Gamma} \frac{\partial}{\partial\mu} \left[\frac{1-\mu^2}{\mu^2} \left(\frac{\partial\bar{Q}}{\partial\mu} + \frac{\partial\bar{E}}{\partial\mu} \right) \right]. \end{aligned} \quad (3.12)$$

Equation (3.12) is easily solved if all variables are expanded by a zero zonal wavenumber, zero frequency Hough function $\Theta_n(\mu)$, or its associated function $B_n(\mu)$ [e.g., *Plumb*, 1982; *Haynes and Shepherd*, 1989; *Kuroda and Kodera*, 2004], as follows:

$$\bar{\omega}^* = \sum_n \omega_n^* \Theta_n(\mu), \quad \bar{Q} = \sum_n Q_n \Theta_n(\mu), \quad \bar{E} = \sum_n E_n \Theta_n(\mu), \quad (3.13)$$

$$\bar{F} = \sum_n \hat{F}_n B_n(\mu), \quad \bar{X} = \sum_n \hat{X}_n B_n(\mu). \quad (3.14)$$

By using equations (3.13) and (3.14), equation (3.12) is degenerated into an ordinary

differential equation with respect to p :

$$\frac{4\Omega^2 a^2 p}{R\Gamma} \frac{d^2 \omega_n^*}{dp^2} + \varepsilon_n \omega_n^* = \frac{2\Omega a p}{R\Gamma} \left(\frac{d\hat{F}_n}{dp} + \frac{d\hat{X}_n}{dp} \right) - \frac{\varepsilon_n}{\Gamma} (Q_n + E_n), \quad (3.15)$$

where ε_n is the n -th eigenvalue of the zonal Hough function. Equation (3.15) is a diagnostic equation; hence, ω_n^* is obtained by substituting the observed external forcings into the right-hand-side of equation (3.15). Boundary values of ω_n^* at the top and bottom are set to be zero as usual. Because of the linearity in equation (3.15), we can separately estimate the contribution of each external forcing and each forced region to residual mean vertical wind (hereafter, we describe these operations as a TEM model).

We can also give realistic boundary conditions in equation (3.15) by treating it as an external forcing. The lower and upper boundary values of observed residual mean vertical velocity are expanded using a Hough function, and these are substituted into differential terms. Treating the differential terms as a kind of external forcing, the effect of boundary conditions can be considered in the TEM model; however, it should be noted that the inclusion of boundaries may generate errors related to topography.

3.2.5. Refractive index

The square of the refractive index, which characterizes the tendency for stationary wave propagation, as given by *Matsuno* [1970] and developed by *Andrews et al.* [1987] and *Hu and Tung* [2002], is presented in spherical quasi-geostrophic form as follows:

$$n_k^2(\phi, z) = \frac{\bar{q}_\phi}{\bar{u}} - \left(\frac{k}{a \cos \phi} \right)^2 - \left(\frac{f}{2NH} \right)^2, \quad (3.16)$$

where

$$\bar{q}_\phi = \frac{2\Omega}{a} \cos \phi - \frac{1}{a^2} \left[\frac{(\bar{u} \cos \phi)_\phi}{\cos \phi} \right]_\phi - \frac{f^2}{\rho_0} \left(\rho_0 \frac{\bar{u}_z}{N^2} \right)_z \quad (3.17)$$

is the meridional gradient of the mean potential vorticity and k is the zonal wavenumber. Stationary waves with zonal wavenumber k are able to propagate in regions where $n_k^2 > 0$ and are refracted toward a region of larger n_k^2 .

3.2.6. Vertical interpolation

To yield the detailed vertical structure, vertical spline interpolation was performed in the upper troposphere and the stratosphere. We interpolated onto the following pressure levels: [175], 162.5, [150], 137.5, [125], 112.5, [100], 90, 80, [70], 60, [50], 40, [30], [20], 15, [10], [7], 6, [5], 4, [3], 2.5, [2], 1.5, 1.2, and [1] hPa, where brackets denote original pressure levels. To avoid analytical error, the interpolation was performed after eddy terms had been calculated at original pressure levels.

3.3. Temperature change and heat budget

Figure 3.1 shows time–height sections of the zonal-mean temperatures averaged over 70°N–90°N and 10°S–10°N, and their anomalies calculated from the mean of the period from December 2008 to March 2009. A rapid increase in 10 hPa temperature occurs in the Arctic region from 18 January, and the warm anomaly propagates downward (Figure 3.1a). At the same time, the 10 hPa temperature in the tropics shows a drastic decline and the cold anomaly propagates downward (Figure 3.1b). Around 26 January, rate of the temperature change reaches its peak at 70 hPa (maximum rate of temperature decrease, -0.34 K/day). The temperature drop between 150 and 125 hPa occurs around 18 January, which is larger than that at 70 hPa (maximum rate of temperature decrease at 125 hPa, -0.4 K/day). There is no clear relationship between the temperature anomalies in the tropical stratosphere and in the tropical troposphere. In the stratosphere we see the usual signature of an evolving SSW from January through early March. In the troposphere the temperature anomalies oscillate on a much shorter time scale that appears unrelated to what transpires above 100 hPa. To identify the cause of the temperature change in the tropics, we performed a heat budget analysis.

Figure 3.2a–e compares the zonal mean temperature and the residual mean vertical wind at various layers from 150 to 10 hPa in the tropics, and Figure 3.2f–j shows the major terms in the TEM thermodynamic equation at the same altitudes as those in Figure 3.2a–e. The upward flow results in a marked decrease in 10 hPa temperature around 19 January (Figure 3.2a), and vertical advection has a strong influence on the 10 hPa potential temperature during this period (Figure 3.2f). The temperature change due

to vertical advection at 70 hPa, which achieves a minimum value on 26 January, is weaker than that at 10 hPa (Figure 3.2b, g). There is no evidence of large rate of temperature changes at 100 hPa after 26 January (Figure 3.2c). On 18 January, the temperature declines in response to vertical advection between 150 and 100 hPa (Figure 3.2c–e, h–j). These changes are not synchronized with those at 70 hPa. In addition, after 18 January, cold temperature anomalies between 150 and 125 hPa persist for 1–2 weeks under the influence of vertical convergence of the vertical heat flux (Figure 3.2i, j). This aspect is discussed in Section 3.6. These observations indicate that the temperature changes between 150 and 100 hPa appear not to be caused by vertical advection associated with the stratospheric process, although the cooling is caused mainly by vertical advection. In Sections 3.4 and 3.5, we examine the forcings that induced tropical ascent between 150 and 100 hPa.

3.4. Tropical upwelling generated by external forcing

To evaluate what and where forcing induce upwelling in the tropics, we estimate the residual mean vertical wind generated by external forcing, using the TEM model introduced in Section 3.2. The vertical flow is estimated for each forcing and each region. The external forcing consists of EP flux divergence, eastward residual forcing, diabatic heating, and vertical eddy heat flux convergence. The forced regions are classified into seven regions (Table 3.1). We compare the residual mean vertical wind from observation and that based on TEM model (equation 3.12).

Figure 3.3 shows the residual mean vertical wind in the tropics averaged between 50 and 20 hPa. Without the boundary effect, although the diagnosed upwelling is smaller than observed, its time development is similar (gray line in Figure 3.3a). When the boundary values are included, the estimated vertical flow resembles the observed flow, although overestimated by approximately 0.2 mm/s. The estimated vertical flow from global forcing above 80 hPa (blue solid line in Figure 3.3) shows good agreement with the observed temporal variation. In contrast, the vertical flow estimated from global forcing below 90 hPa (green line in the figure) indicates minor variability and is not in good agreement with observed variations. The global forcing above 80 hPa induces the bulk of the temporal variation between 50 and 20 hPa. Furthermore, in the case of northern hemispheric forcing above 80 hPa, the estimated vertical flow performs pretty

well in reconstructing the observed temporal variation (Figure 3.3b; blue dashed line). Thus, the TEM model performs well in reproducing the temporal variations, and the northern hemispheric forcing above 80 hPa generates most of the tropical upwelling in the stratosphere. In the northern hemispheric forcing above 80 hPa, divergence of the EP flux (especially $F_1^{(z)}$) controls tropical ascent in the stratosphere (not shown).

Figure 3.4a compares the observed residual mean vertical wind with that calculated from all external forcings in the TEM model, averaged between 150 and 100 hPa in the tropics. The observed values show a maximum at 2.4 mm/s on 18 January, for the values estimated from forcings in both the all regions and the global region below 90 hPa. In addition, these estimated vertical flows are very similar to the observed variation throughout January, although underestimated. In the case of global forcing above 80 hPa, the tropical ascent is weakly driven during January (blue line in Figure 3.4a). This finding indicates that tropical ascent is driven by global forcing below 90 hPa throughout January (green solid line). Therefore, the stratospheric pump has only a minor influence on vertical flow between 150 and 100 hPa. The estimated values are systematically smaller than those observed. When the boundary values are included, the mean estimated value is closer to the mean observed value, but the estimated temporal variation differs slightly from that observed.

Figure 3.4b compares the residual mean vertical velocity generated by global forcing below 90 hPa with that by forcings below 90 hPa in the southern and northern hemispheres. The maximum on 18 January is caused mainly by forcing in the northern hemisphere below 90 hPa (green dashed line), and the second peak on 9 January is driven by southern hemispheric forcing below 90 hPa (green dotted line). Thus, on 18 January, upwelling in the tropics between 150 and 100 hPa is generated mainly by northern hemispheric forcing below 90 hPa.

Figure 3.5 compares the residual mean vertical wind calculated by each component of northern hemispheric forcing below 90 hPa. The mean vertical flow is driven by diabatic heating (purple dash-dotted line in the figure) and vertical divergence of $F_2^{(z)}$ (blue dotted line; associated with the vertical momentum flux $\overline{u'w'}$). Because of small temporal variation in contribution of the diabatic heating, diabatic upwelling balanced with infrared radiative relaxation did not have large impact on the temporal variation of tropical upwelling between 150 and 100 hPa. Temporal variations in vertical flow are

mainly forced by vertical divergence of $F_1^{(z)}$ (red dashed line), especially around 18 January. Temporal variations in the divergences of $F_2^{(\phi)}$ and $F_2^{(z)}$ influence the upward flow around 17 January and 15 January, respectively. In fact, $F_1^{(z)}$ is the dominant contributor to the maximum in tropical ascent between 150 and 100 hPa on 18 January. In the eddy forcing, $F_1^{(z)}$ makes the dominant contribution in both stratospheric forcing and tropospheric forcing on 18 January. It is necessary to examine tropical upwelling driven by stratospheric and tropospheric wave forcing, especially by $F_1^{(z)}$ in the meridional plane.

Figure 3.6 shows anomalies of the estimated vertical flow from divergence of the EP flux above 80 hPa and from vertical divergence of $F_1^{(z)}$ above 80 hPa on 18 January. These anomalies are calculated from the mean value for January 2009. There is a small anomaly of stratospheric circulation due to very weak divergence of the EP flux in the southern hemisphere above 80 hPa (Figure 3.6a). A strong negative anomaly of EP flux divergence at high latitudes in the upper stratosphere generates a large anomaly in stratospheric circulation (Figure 3.6b). A downwelling anomaly is induced at high latitudes and an upwelling anomaly is induced south of 50°N. The anomaly of residual mean vertical wind decays with decreasing altitude. The stratospheric wave forcing generates only a negligible tropical ascent (<0.1 mm/s) below 70 hPa on 18 January. Southern hemispheric forcing above 80 hPa due to the divergence of $F_1^{(z)}$ is too weak to generate a strong anomaly of stratospheric circulation (Figure 3.6c). Forced by the divergence of $F_1^{(z)}$ in the northern hemispheric stratosphere, stratospheric circulation intensifies broadly, especially in the extratropical upper stratosphere, and weak tropical ascent is generated in the lowermost stratosphere (Figure 3.6d).

Figure 3.7 is the same as Figure 6, but for forcing below 90 hPa. Convergence of the EP flux at around 7°S, 150 hPa induces a positive anomaly of vertical flow in the tropics between 200 and 150 hPa and at around 13°S, 125 hPa (Figure 3.7a). Eddy forcing in the southern hemispheric troposphere has an insignificant effect on the TTL. Convergence of the EP flux at around 15°N in the upper troposphere and lower stratosphere generates a strong, broad upwelling anomaly in the tropics between 500 and 100 hPa (Figure 3.7b). In particular, remarkable tropical ascent is induced around 250 and 125 hPa due to convergence of the EP flux.

The vertical convergence of $F_1^{(z)}$ at around 15°N, 100 hPa generates a positive

anomaly of the estimated vertical flow in the tropics between 150 and 100 hPa, while convergence of $F_1^{(z)}$ around 15°S, 150 hPa generates a positive anomaly of estimated vertical flow in the tropics at around 200 hPa (Figure 3.7c, d). Vertical convergence of $F_1^{(z)}$ drove large part on tropical upwelling anomaly between 150 and 100 hPa (the other part driven by convergences of $F_2^{(\phi)}$ and $F_2^{(z)}$). Vertical convergences of $F_1^{(z)}$ at around 15°N, 100 hPa and 15°S, 150 hPa are the main factor in inducing tropical ascent at around 125 and 200 hPa, respectively. In next section, we investigate wave activity that caused the tropical upwelling in detail.

3.5. Wave activity around the TTL

3.5.1. Eliassen-Palm flux

Figure 3.8 shows latitude–height sections of the EP flux, its divergence, and the residual mean vertical wind. Before the SSW occurred, the vertical component of the EP flux is weak in the extratropical troposphere and stratosphere, and equatorward EP flux is weak in the subtropics of northern hemispheric upper troposphere (Figure 3.8a, b). Thus, convergence of the EP flux is small around 15°N, 125 hPa. On 18 January, upward flow (> 4 mm/s) occurs broadly in the tropical upper troposphere (Figure 3.8c). Equatorward EP flux diverges vertically at around 20°N, which causes convergence of the vertical component of the EP flux at around 200 hPa, 15°N and 100 hPa, 15°N. As shown in Figure 3.7, convergence of the EP flux (especially $F_1^{(z)}$) around 15°N, 100 hPa is the main contributor of tropical upwelling between 150 and 100 hPa. On 26 January, upward flow occurs in the tropics below 150 hPa. At the same time, the equatorward EP flux decreases in the subtropical troposphere (Figure 3.8d). In these cases, wave propagation from the extratropical troposphere to the tropics is contributed by the second meridional component of the EP flux $F_2^{(\phi)}$ (associated with the meridional eddy momentum flux $\overline{u'v'}$) and the first vertical component of the EP flux $F_1^{(z)}$ (associated with the meridional eddy heat flux $\overline{v'\theta'}$) (not shown). Equatorward EP flux from the midlatitude troposphere appears to be coincident with upward EP flux in the midlatitude troposphere and stratosphere.

Figure 3.9 shows a time–altitude section of $F_1^{(z)}$ in mid-latitudes and a time–latitude section of $F_2^{(\phi)}$ averaged over 125 and 100 hPa. From 15 January, $F_1^{(z)}$ is amplified

in the mid-latitude troposphere, which causes the SSW event (Figure 3.9a). At the same time, the equatorward EP flux is intensified between 125 and 100 hPa (Figure 3.9b). These components of the EP flux ($F_2^{(\phi)}$ and $F_1^{(z)}$) may be excited by the same wave source. To examine the wave activity in detail, it is necessary to investigate not only the meridional field but also the three-dimensional field.

3.5.2. Three-dimensional wave activity flux

To investigate the wave behavior in detail, we calculated the three-dimensional wave activity flux, as proposed by *Plumb* [1985]. Figure 3.10 shows the time evolution of *Plumb's* [1985] wave activity flux \mathbf{F}_s averaged between 125 and 100 hPa. On 12 January, the amplitude of wave activity flux is weak in the boreal mid-latitudes (Figure 3.10a). On 15 January, wave activity over Alaska is blooming, and horizontal wave activity fluxes toward the tropical areas of the eastern Pacific and Atlantic are amplified (Figure 3.10b). Due to downward wave activity flux around the northwestern Pacific, the zonal mean vertical component of the wave activity flux, which corresponds to the vertical component of the EP flux, is negative around 10°N. On 18 January, strong upward and southeastward wave activity fluxes are furthermore excited over Alaska (Figure 3.10c). This upward wave activity flux apparently dominates the vertical component of the EP flux at high latitudes. In addition, the southeastward wave activity flux propagates toward the tropical eastern Pacific, and the eastward wave activity flux propagates farther toward the tropical eastern Atlantic. In the tropical eastern Pacific/Atlantic, the waves propagate upward. The upward wave activity flux in the tropical eastern Pacific and Atlantic has a large influence on the vertical component of the EP flux (not shown). Subsequently, the horizontal and vertical wave activity flux decays over Alaska, and upward wave activity flux in the tropical area of the eastern Pacific and Atlantic also diminishes (Figure 3.10d).

Because the mean westerly flow extends to the tropical upper troposphere over the eastern Pacific and Atlantic during the boreal winter and spring (referred to as the “westerly duct”), the equatorward-propagating waves are able to enter the tropics [e.g., *Webster and Holton*, 1982; *Kiladis and Weickmann*, 1997]. *Harada et al.* [2010] showed that wave activity over Alaska developed and intensified wave-2 structure in the

northern high-latitudes during 15-20 January, and suggested that it played an important role in the SSW that occurred during January 2009. Thus, wave activity over Alaska has two roles; the equatorward EP flux between 125 and 100 hPa entering the tropics caused tropical upwelling between 150 and 100 hPa, and the upward EP flux in the extratropics caused the SSW event.

3.6. Discussion

3.6.1. Tropical convection

In Section 3.3, we reported that vertical convergence of the vertical heat flux $\overline{w'\theta'}$ resulted in reduced heating in the tropical uppermost troposphere from 12 to 26 January. The vertical heat flux is strongly linked to localized convection around the western tropical Pacific. *Yoshida and Yamazaki* [2010] suggested that the concentration of localized convection, such as the deep convection in the tropical western Pacific, warms the tropical uppermost troposphere and cools the upper TTL via vertical convergence of the vertical heat flux, $-\rho_0^{-1}\partial(\rho_0\overline{w'\theta'})/\partial z$.

Figure 3.11 shows the time evolution of OLR and the vertical heat flux in the tropics. Before the SSW event, convection is gradually concentrated and intensified in the SPCZ, and negative value of the vertical heat flux is amplified at around 100 hPa (Figure 3.11a, b, e, f). The strong negative value of the vertical heat flux results in enhanced divergence in the lowermost stratosphere and enhanced convergence in the tropical uppermost troposphere. With the onset of the SSW event, convection observed to decay near the tropical western Pacific and to intensify over tropical South America (Figure 3.11c). At the same time, the negative value of the 100 hPa vertical heat flux decays, resulting in weakened heating in the tropical uppermost troposphere (Figure 3.11g). Subsequently, the more tropical convection extends zonally, the greater the degree that the negative value of the 100 hPa vertical heat flux diminishes (Figure 3.11d, h). This result corresponds to the decay of heating by vertical convergence of the vertical heat flux in the tropical uppermost troposphere. The time evolution of convection is consistent with variations in vertical convergence of the vertical heat flux in the tropical uppermost troposphere.

Our results accord with those of several studies, which indicate that the occurrence

of ascent and reduced static stability ahead of the cyclonic anomaly in the westerly duct, consistent with the interpretation that equatorward-propagating waves force the convection [Kiladis, 1998; Matthews and Kiladis, 2000]. In fact, the region in which the equatorward-propagating waves enter appears to generate a lower OLR (see Figures 3.10 and 3.11). Hence, during the SSW event, the equatorward-propagating wave activity may cause not only circulation change in the TTL, but convection change. Further study is required on this topic.

3.6.2. Wave propagation towards the tropics

The results presented in Sections 3.4 and 3.5 indicate that wave propagation originating over Alaska has an influence on tropical ascent in the uppermost troposphere on 18 January. To generate tropical ascent in the uppermost troposphere, dissipation of the waves must have its maximum above the uppermost troposphere. To investigate why the waves propagate toward the tropical lowermost stratosphere, we calculated the refractive index for a stationary wave of zonal wavenumber 5, based on the mean field of the western hemisphere averaged from 10 to 17 January (Figure 3.12a). Because of the small scale of the waves propagating to the tropics, the western hemisphere may be regarded as the background. Equatorward EP flux from the mid-latitude troposphere splits into two directions: toward the tropical lowermost stratosphere and toward the subtropics at around 250 hPa. Because these regions have a high refractive index, the equatorward-propagating waves change in direction and dissipate in the lowermost stratosphere at around 15°N. At this time, the westerlies weaken with height in the TTL of the western hemisphere (Figure 3.12b). Therefore, the tropical lowermost stratosphere has a high refractive index. Kiladis [1998] suggested that wave activity becomes more vertically constrained and propagates into the stratosphere as it moves equatorward through the subtropics, because the westerly weakens with height in the westerly duct.

3.7. Summary

In a study of the major stratospheric sudden warming (SSW) event of January 2009, we analyzed the temperature change and its mechanism in the tropics, focusing on the TTL, yielding the following main findings.

- (1) During the SSW event, wave forcing, especially by meridional eddy heat flux

(first vertical component of the EP flux $F_1^{(z)}$), in the northern hemispheric stratosphere strongly induced tropical ascent in the stratosphere. However, the stratospheric wave forcing induced only weak upwelling in the tropics below 100 hPa.

(2) On 18 January, at the onset of the SSW event, tropical ascent was the main contributor to cooling in the tropics between 150 and 100 hPa. Subsequently, vertical convergence of the vertical heat flux $\overline{w'\theta'}$, which is closely tied to the convection structure, resulted in a gradual decrease in heating and temperature in the tropical uppermost troposphere.

(3) Residual mean vertical wind calculated by the transformed Eulerian mean model indicates that the wave dissipation around 15°N, 100 hPa was the main driver of tropical ascent between 150 and 100 hPa on around 18 January.

(4) Equatorward-propagating waves at around 100 hPa, which had same wave source with the upward-propagating waves that caused the SSW event, traveled from Alaska to the tropical areas of eastern South America and eastern Africa, entered the tropical lowermost stratosphere, and dissipation of the waves drove the tropical upwelling between 150 and 100 hPa on around 18 January.

Table 3.1. List of regions where external forcings are imposed.

Forced region	Forced region in detail
All regions	90°S-90°N, 975-1.2 hPa
Global stratosphere	90°S-90°N, 80-1.2 hPa
Northern hemispheric stratosphere	EQ-90°N, 80-1.2 hPa
Southern hemispheric stratosphere	90°S-EQ, 80-1.2 hPa
Global troposphere	90°S-90°N, 975-90 hPa
Northern hemispheric troposphere	EQ-90°N, 975-90 hPa
Southern hemispheric troposphere	90°S-EQ, 975-90 hPa

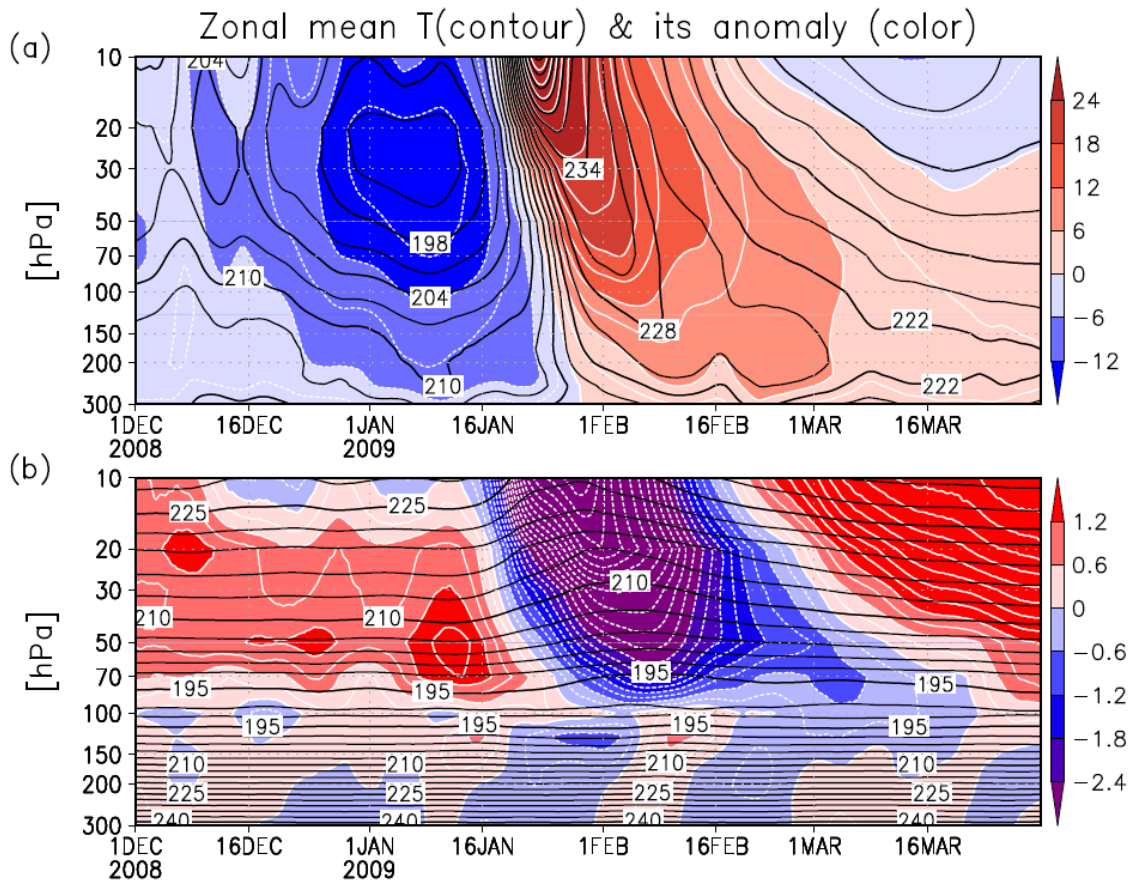


Figure 3.1. Time–altitude section of zonal mean temperature (K; contours) and its anomaly (K; color shading) averaged over (a) 70°N – 90°N and (b) 10°S – 10°N . The anomaly is the deviation from the 3-month mean. White contours show the anomaly of the zonal mean temperature, with contour intervals of 3 K in (a) and 0.3 K in (b). Black contour interval is 3 K. Data are smoothed using a 5-day running average.

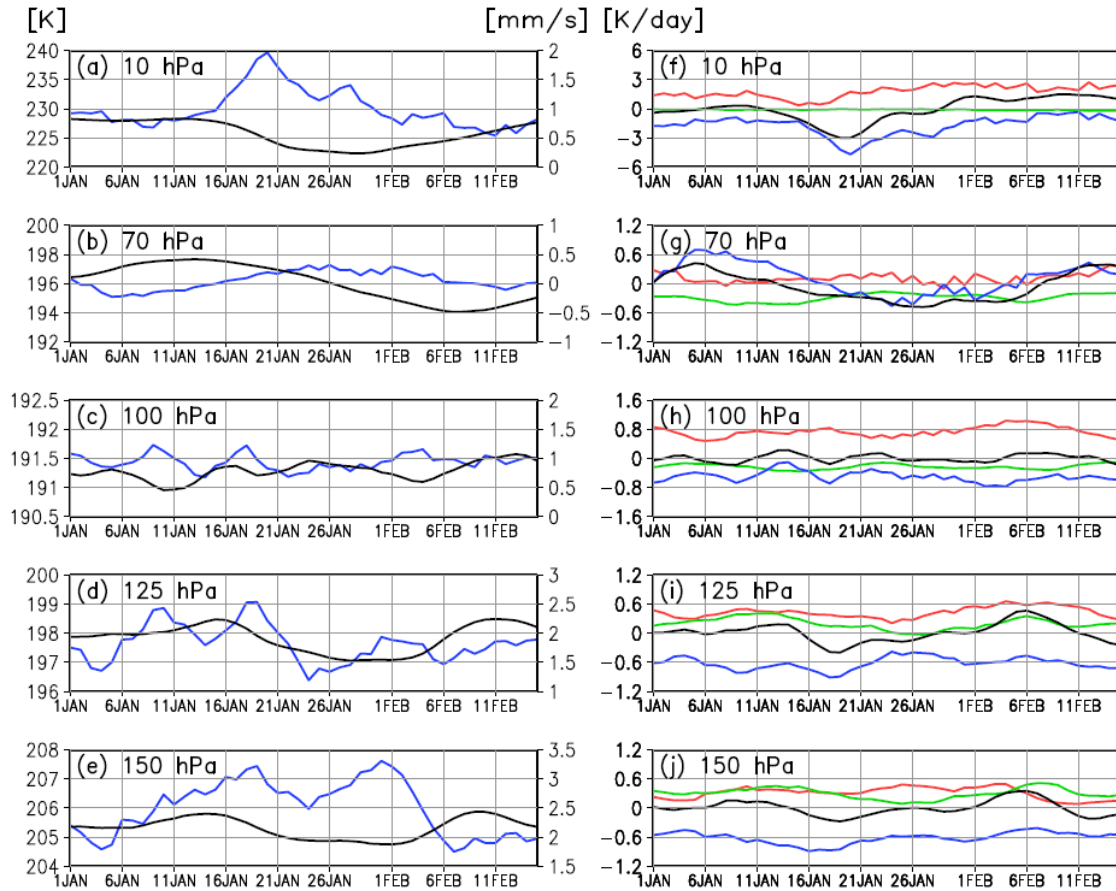


Figure 3.2. Time series of (left) zonal-mean temperature (K; black lines), residual mean vertical wind ($mm\ s^{-1}$; blue lines), and (right) major terms in the transformed Eulerian mean (TEM) thermodynamic equation averaged over $10^{\circ}S-10^{\circ}N$ ($K\ d^{-1}$). (a, f) 10 hPa, (b, g) 70 hPa, (c, h) 100 hPa, (d, i) 125 hPa, and (e, j) 150 hPa. The terms in the TEM thermodynamic equation consist of potential temperature change (black lines), vertical advection (blue lines), convergence of vertical eddy heat flux (green lines), and diabatic heating (red lines). Other terms are not shown. Data are smoothed using a 5-day running average.

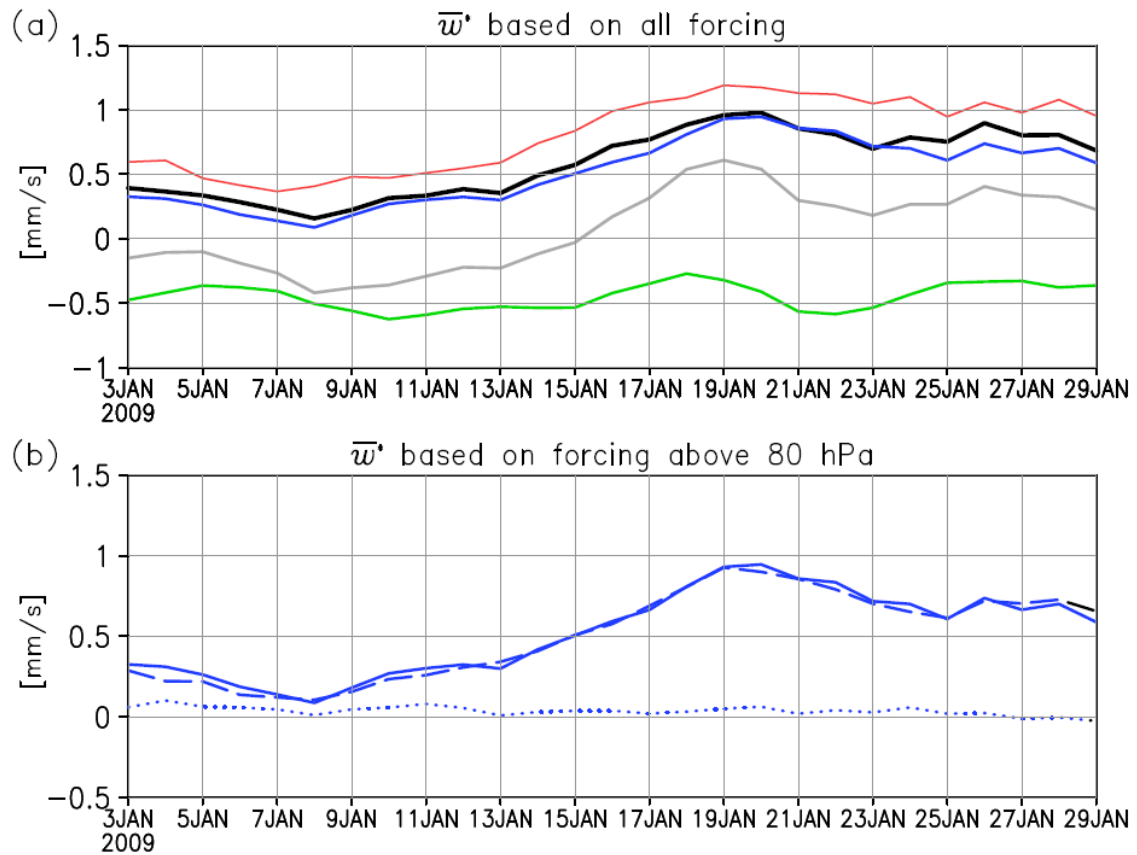


Figure 3.3. Time series of residual mean vertical wind (mm s^{-1}) in the tropics averaged over 50–20 hPa, based on all forcings. (a) Observations (black thick-solid line), forcing in the all regions (grey solid line), all regions including boundaries (red thin-solid line), global troposphere (green solid line), and global stratosphere (blue solid line). (b) Forcing in the global stratosphere (blue solid line; same as Figure 3.6a), northern hemispheric stratosphere (blue dashed line), and southern hemispheric stratosphere (blue dotted line). See Table 3.1 for details.

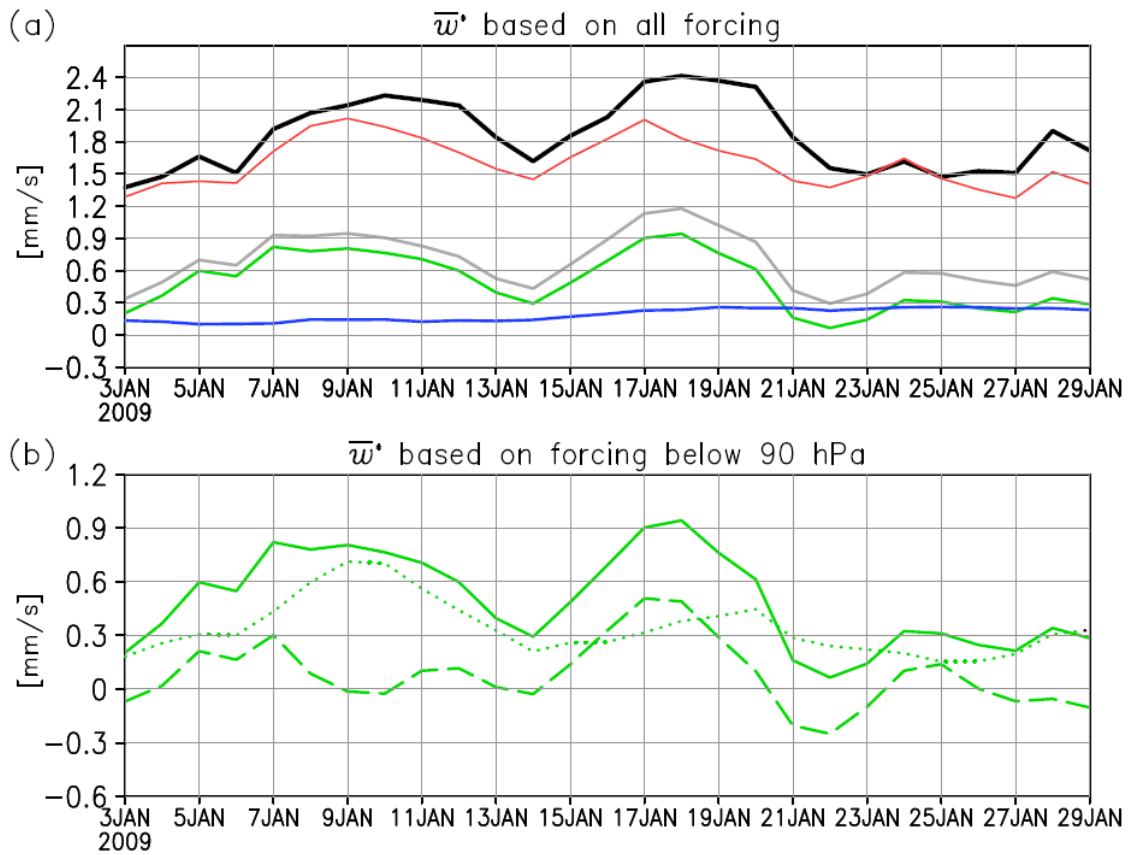


Figure 3.4. As for Figure 3.3, except for residual mean vertical wind (mm s^{-1}) in the tropics averaged over 150–100 hPa. (a) Observations (black thick-solid line), forcing in the all regions (gray solid line), all regions including boundaries (red thin-solid line), global troposphere (green solid line), and global stratosphere (blue solid line). (b) Forcing in the global troposphere (green solid line; same as Figure 3.7a), northern hemispheric troposphere (green dashed line), and southern hemispheric troposphere (green dotted line). See Table 3.1 for details.

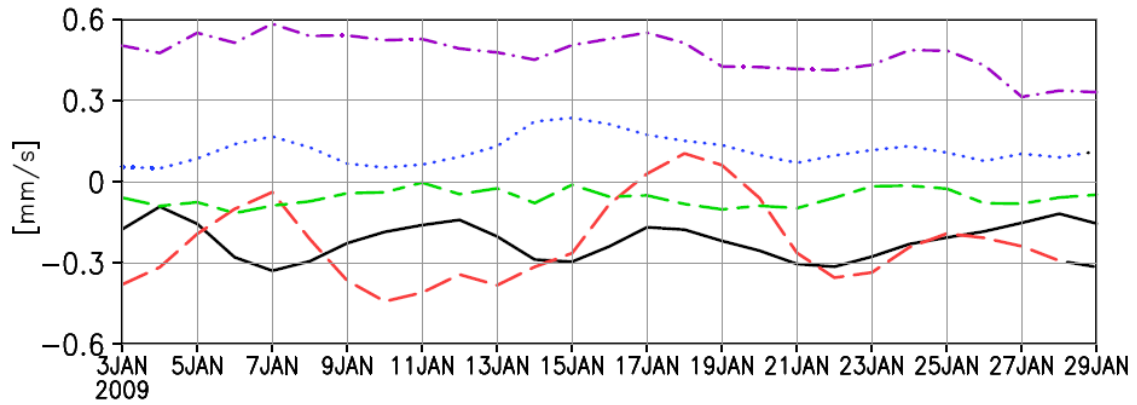


Figure 3.5. Time series of residual mean vertical wind (mm s^{-1}) in the tropics averaged over 150–100 hPa, based on each component of forcings in the northern hemispheric troposphere. Divergence of second meridional component of the EP flux $F_2^{(\phi)}$ (black solid line), divergence of first vertical component of the EP flux $F_1^{(z)}$ (red dashed line), divergence of second vertical component of the EP flux $F_2^{(z)}$ (blue dotted line), eastward residual forcing \bar{X} (green long–short dashed line), and diabatic heating \bar{Q} (purple dash–dotted line). Estimated vertical wind by other forcings is not shown because of its small value. See Table 3.1 for details.

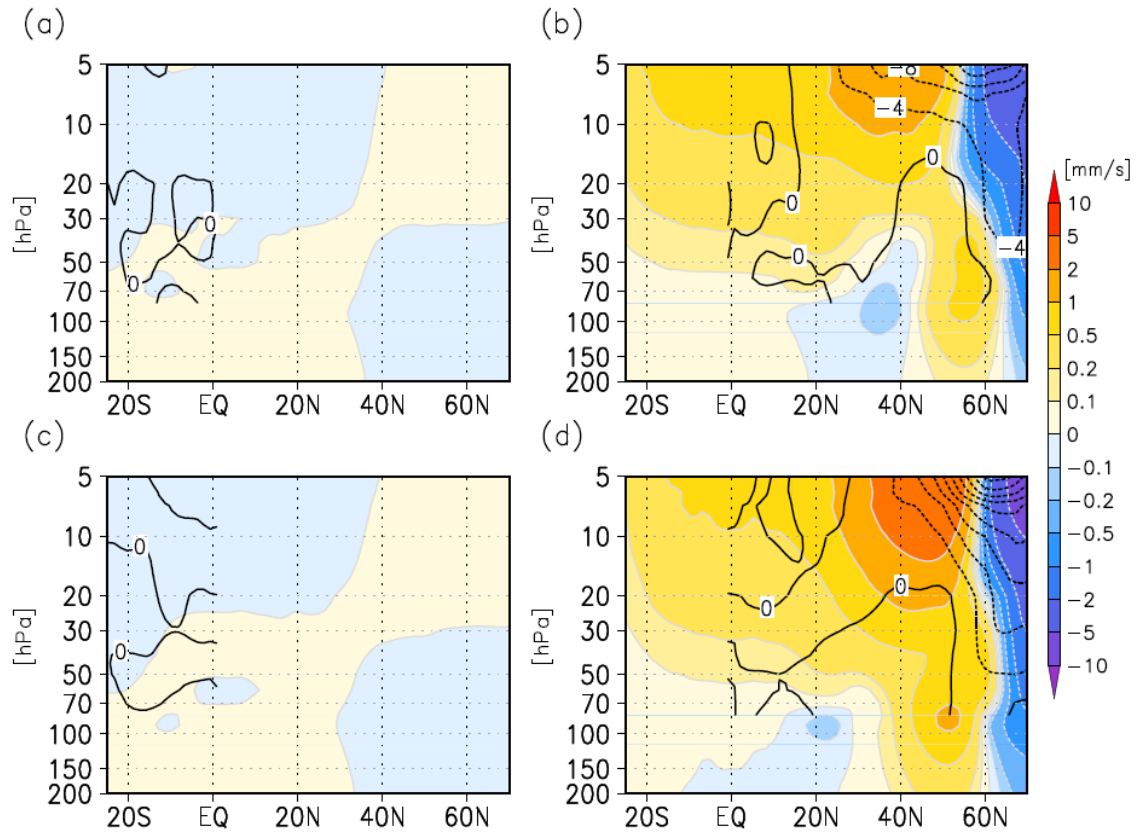


Figure 3.6. (Top) Anomalies of the EP flux divergence (contours; $\text{m s}^{-1}\text{d}^{-1}$) and of the generated residual mean vertical wind using the EP flux divergence above 80 hPa (color shading; mm s^{-1}) on 18 January 2009: (a) forcing in the southern hemispheric stratosphere and (b) northern hemispheric stratosphere. (bottom) Anomalies of divergence of first vertical component of the EP flux $F_1^{(z)}$ (contours; $\text{m s}^{-1}\text{d}^{-1}$) and of the generated residual mean vertical wind using divergence of $F_1^{(z)}$ above 80 hPa (color shading; mm s^{-1}) on 18 January: (c) forcing in the southern hemispheric stratosphere and (d) northern hemispheric stratosphere. These anomalies are the deviation from the mean value for January 2009. Contour interval is $4 \text{ m s}^{-1}\text{d}^{-1}$. Divergences of the EP flux and $F_1^{(z)}$ below 90 hPa are not shown. See Table 3.1 for details.

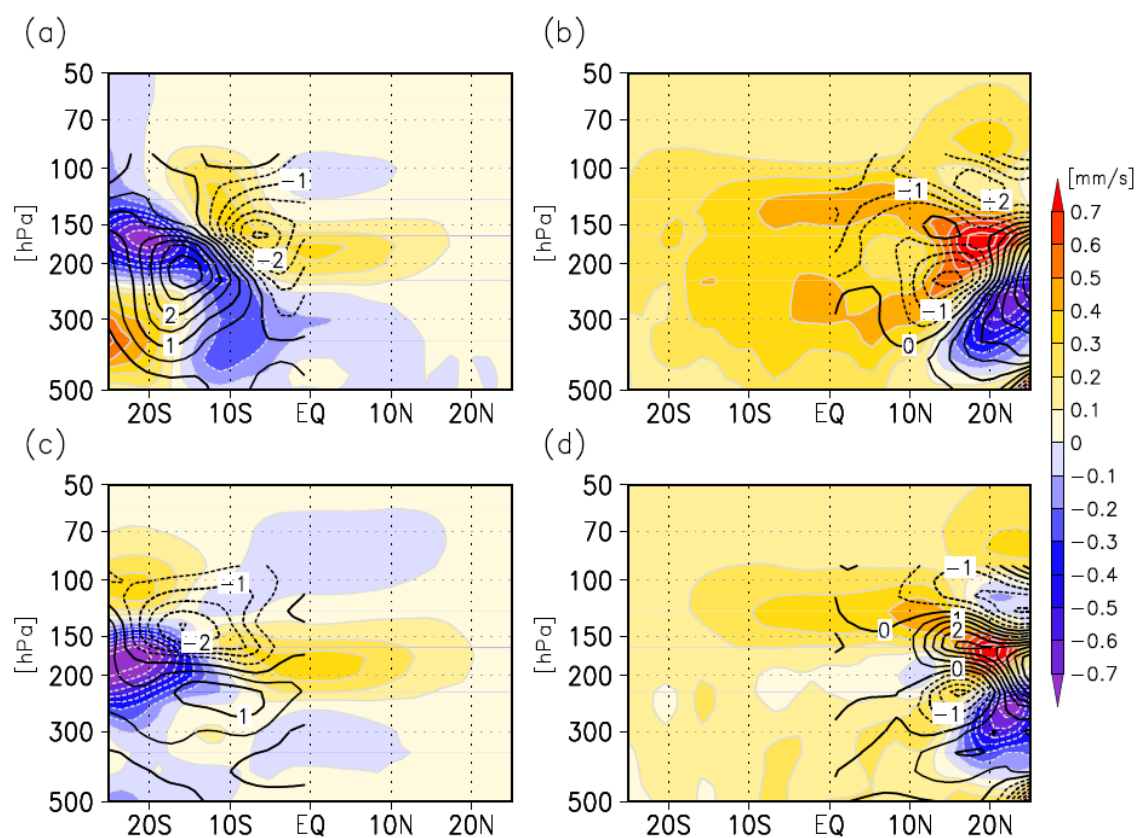


Figure 3.7. As for Figure 3.6, except for (left) forcing in the southern hemispheric troposphere and (right) northern hemispheric troposphere. Contour interval is $0.5 \text{ m s}^{-1} \text{ d}^{-1}$. See Table 3.1 for details.

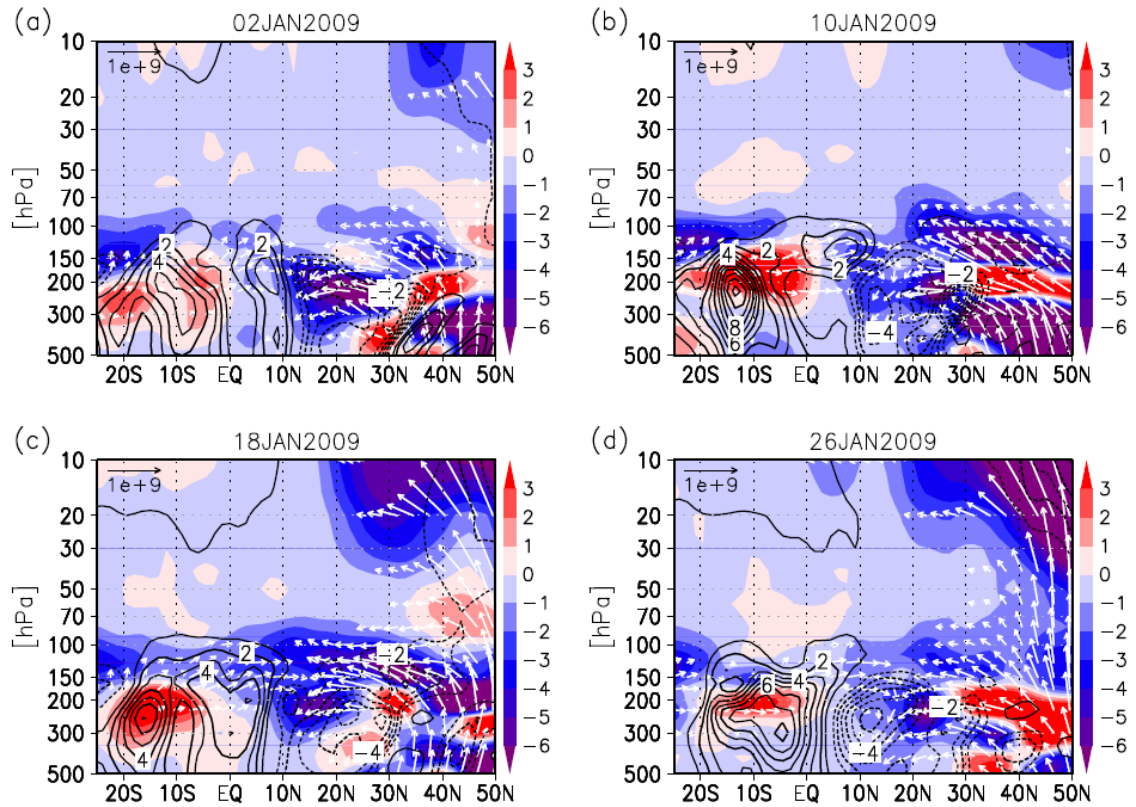


Figure 3.8. Latitude–height section of the Eliassen–Palm (EP) flux (vectors; $\text{m}^3 \text{s}^{-2}$), the EP flux divergence (color shading; $\text{m s}^{-1} \text{d}^{-1}$), and the residual mean vertical wind (contours; mm s^{-1}) on (a) 2 January 2009, (b) 10 January 2009, (c) 18 January 2009, and (d) 26 January 2009. The EP flux is divided by the reference density, and the vertical component of the EP flux is multiplied by 300.

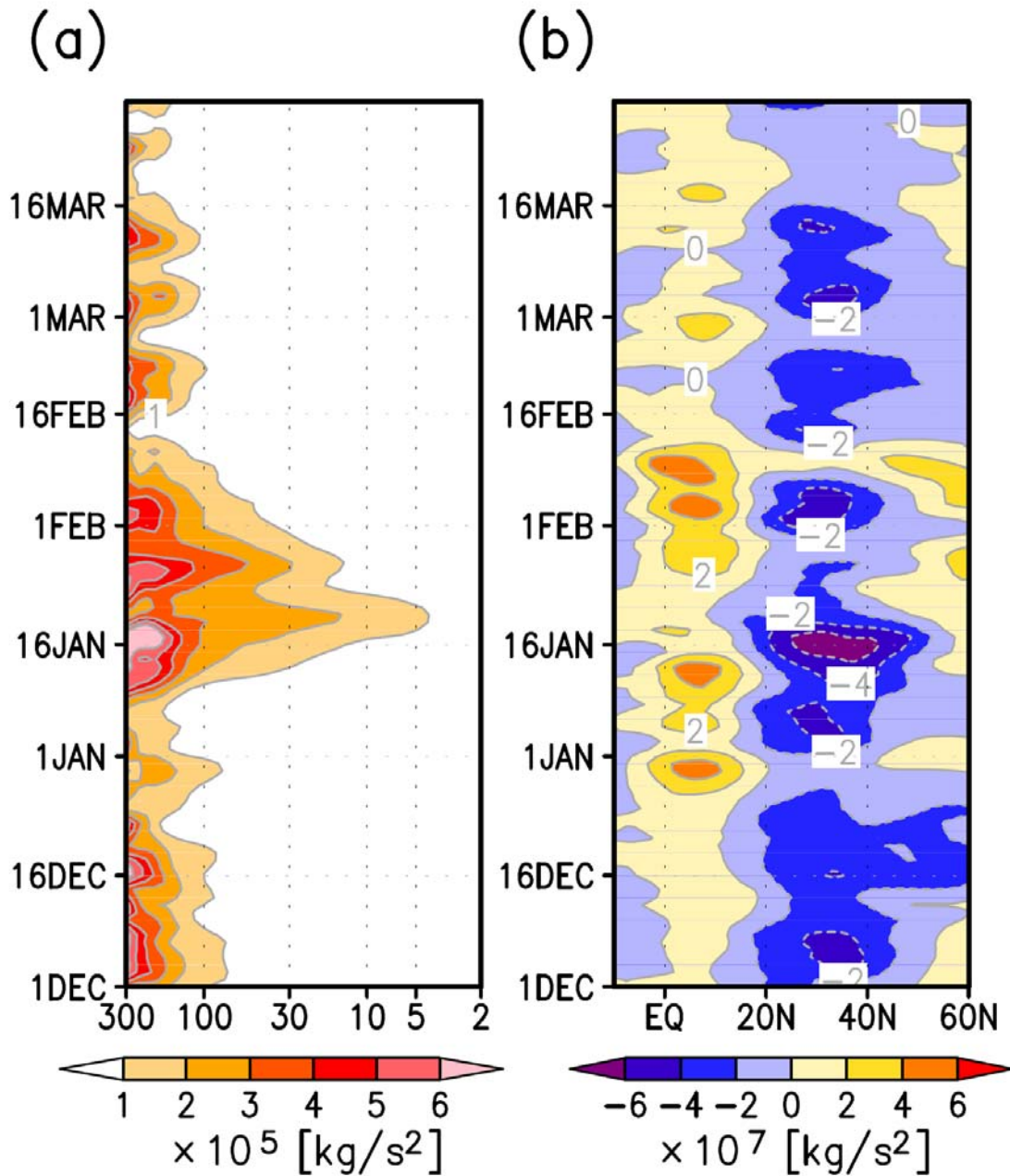


Figure 3.9. (a) Time–altitude section of the first vertical component of the Eliassen–Palm (EP) flux $F_1^{(z)}$ averaged over 40°N–70°N. (b) Time–latitude section of the second meridional component of the EP flux $F_2^{(\phi)}$ averaged between 125 and 100 hPa.

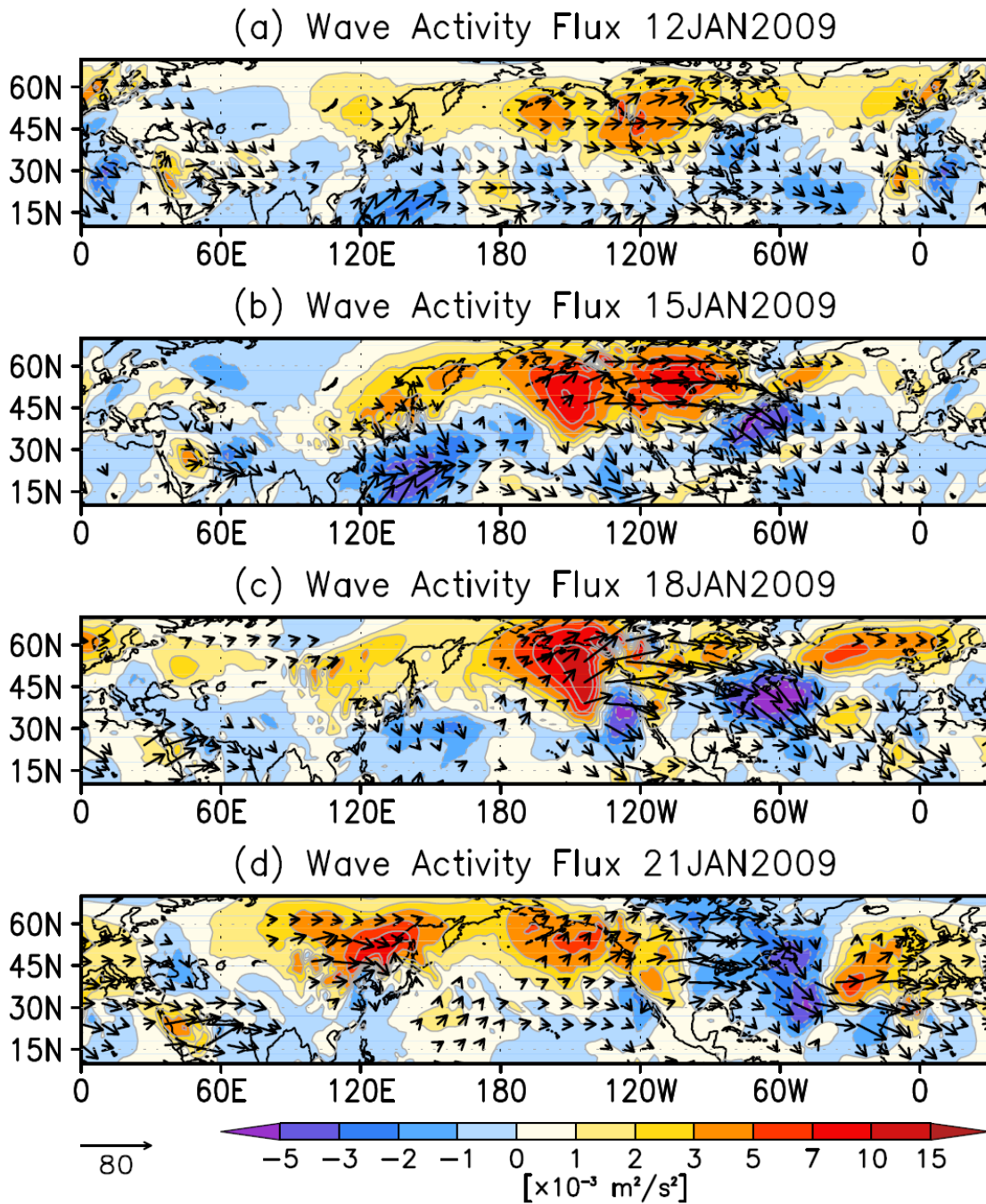


Figure 3.10. Maps of the horizontal component of *Plumb's* [1985] 3-D wave activity flux (vectors; $\text{m}^2 \text{s}^{-2}$) and vertical component (color shading; $\text{m}^2 \text{s}^{-2}$) averaged between 125 and 100 hPa on (a) 12 January 2009, (b) 15 January 2009, (c) 18 January 2009, and (d) 21 January 2009. Vectors and colors are multiplied by $\cos \phi$.

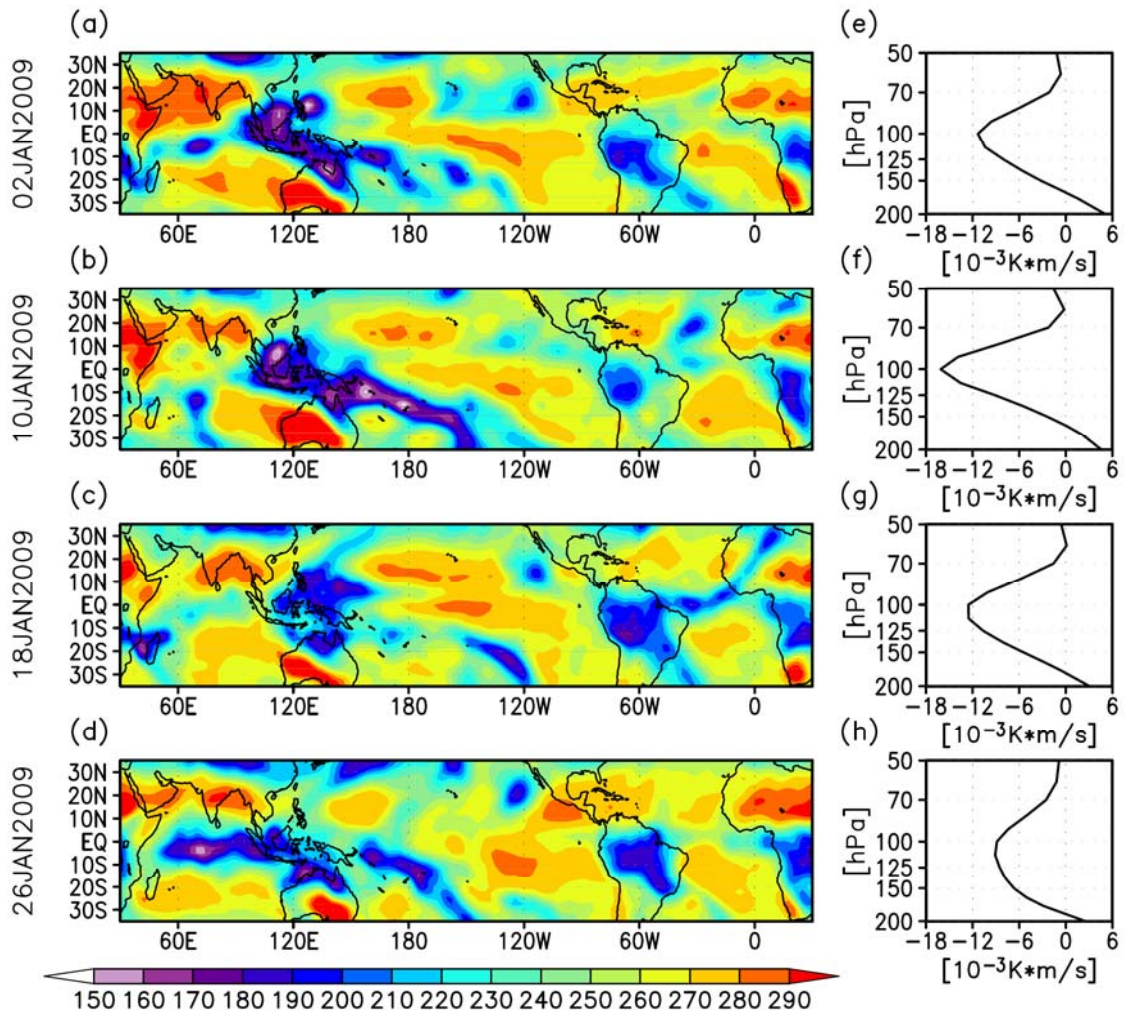


Figure 3.11. (left) Maps of OLR (W m^{-2}) and (right) vertical profiles of the vertical eddy heat flux $\overline{w'\theta'}$ (K m s^{-1}) averaged over 10°S–10°N. (a, e) 2 January 2009, (b, f) 10 January 2009, (c, g) 18 January 2009, and (d, h) 26 January 2009. Data are smoothed using a 5-day running average.

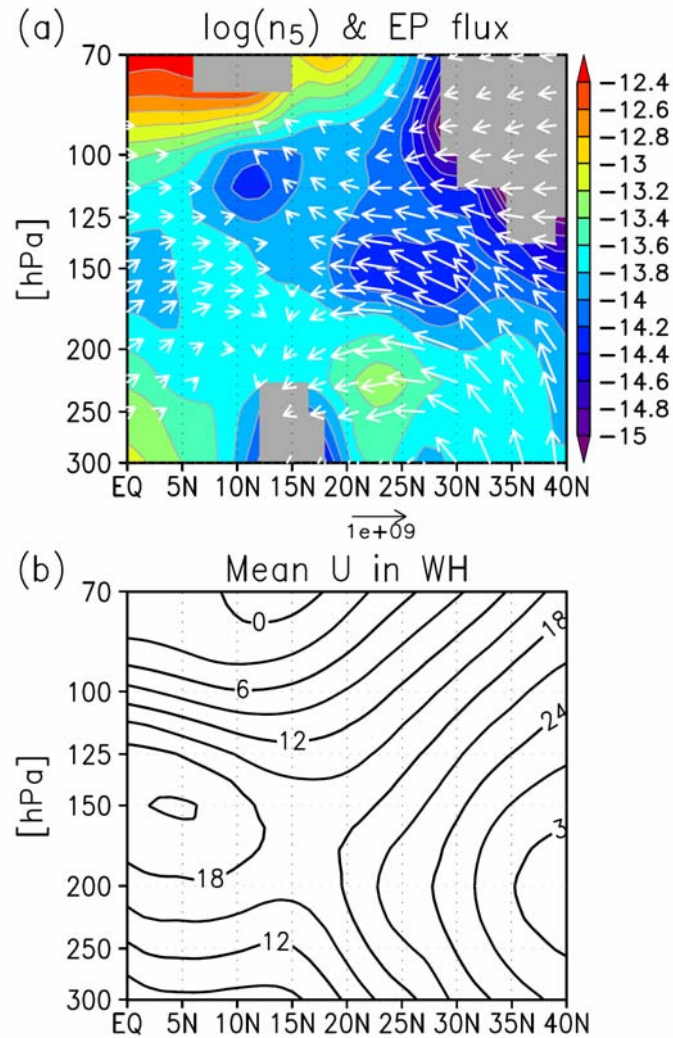


Figure 3.12. (a) Latitude–altitude section of refractive index for stationary waves in zonal wavenumber 5 in the western hemisphere (color shading). Vectors denote the EP flux ($\text{m}^3 \text{s}^{-2}$) on 18 January. (b) Latitude–altitude section of western hemispheric mean zonal wind (m s^{-1}). Data averaged from 10 to 17 January are used to calculate the refractive index and the zonal wind. The refractive index is expressed by a logarithmic unit; imaginary values of the refractive index are masked. The EP flux is divided by the reference density, and the vertical component of the EP flux is multiplied by 300.

Chapter 4| Seasonal changes in temperature and circulation in the tropical tropopause layer

4.1. Introduction

The annual cycle of temperatures at the tropical tropopause and in the tropical tropopause layer (hereafter TTL) is an important feature of the atmosphere [e.g. *Highwood and Hoskins, 1998; Fueglistaler et al., 2009a*; and see Chapter 1 and 2]. Figure 4.1 shows the annual cycle in zonal mean temperature in the tropics between 500 and 10 hPa levels (departure from the annual mean). There is a large annual cycle in temperature at around 70 hPa, which has a strong influence on concentration of water vapor in the stratosphere [*Mote et al., 1996*]. The annual cycle in temperature between 125 and 70 is not similar to that in the tropical troposphere. As introduced in Chapter 2, two mechanisms have been invoked to explain this annual cycle. The first is stratospheric pump, and the second is localized meridional circulation in the TTL generated by deep convection.

Figure 4.2 shows annual cycle of the residual mean vertical wind between 125 and 70 hPa. Upwelling at 70 hPa over 10°S - 10°N is weaker than that over the subtropics, and has semiannual variation of maximum in boreal spring and fall (Figure 4.2a). At both 100 and 125 hPa, upwelling over 10°S - 10°N is stronger in December and April, and weaker in August (Figure 2b and 2c), and it is different from that in the subtropics. The annual cycle of the upwelling averaged over 15°S - 15°N between 100 and 125 hPa is weaker than that over 10°S - 10°N . At 100 hPa, in the case averaged over 10°S - 10°N , the peak-to-peak value is 0.7 mm/s, which is 0.2 mm/s larger than that averaged over 15°S - 15°N . *Randel et al. [2008]* calculated the annual cycle of 100-hPa tropical (15°S - 15°N) upwelling following downward control mechanism by *Haynes et al. [1991]*, and suggested that equatorward extension of extratropical waves (baroclinic eddy and, in the northern hemisphere, quasi-stationary planetary waves) contribute a large component of the subtropical wave driving at 100 hPa. However, *Kerr-Munslow and Norton [2006]* showed EP flux divergence summed at 15°S and 15°N is weaker than that at 10°S and 10°N , and the terms which have dominant variation are different with latitudes.

As *Kerr-Munslow and Norton* [2006] pointed out, rate of temperature changes at around 100 hPa is uniform over 10° S-10° N. Additionally upwelling over 10° S-10° N does not synchronize with that over the subtropics between 125 and 70 hPa. Therefore, annual cycles of temperature changes and thermodynamic balance over 10° S-10° N are worth considering issue. The aim of this chapter is to clarify main drivers of annual cycle in the temperature over 10° S-10° N between 125 and 70 hPa.

The remainder of this chapter is organized as follows. Section 4.2 provides a description of the dataset and analysis methods, and Section 4.3 outlines the structures of temperature and the thermodynamic budget. The nature of the forcing that causes the upwelling in the TTL is evaluated in Section 4.4. The characteristics of wave forcing and unresolved forcing are described in Sections 4.5 and 4.6. Finally, the main results of this chapter are summarized in Section 4.7.

4.2. Data and methods

We used a 6-hourly dataset of European Centre for Medium-Range Weather Forecasts (ECMWF) ERA-Interim [*Simmons et al.*, 2006; *Uppala et al.*, 2008]. The period of analysis was from 1 January 1989 to 31 December 2009. Interpolated outgoing long-wave radiation (OLR) data were obtained from the Climate Diagnostic Center (CDC) of the National Oceanic and Atmospheric Administration (NOAA) [*Liebmann and Smith*, 1996]. To yield the detailed vertical structure, vertical spline interpolation was performed in the upper troposphere and the stratosphere as applied in Section 3.2.

To evaluate the zonal mean thermodynamic balance, quantitative analysis was performed by the transformed Eulerian mean (TEM) equations applied in Chapter 2. Tropical upwelling is estimated from the TEM eastward momentum balance and mass conservation as applied in *Haynes et al.* [1991] [see also *Andrews et al.*, 1987];

$$\frac{\partial \bar{u}}{\partial t} + \left[\frac{(\bar{u} \cos \phi)_\phi}{a \cos \phi} - f \right] \bar{v}^* + \frac{\partial \bar{u}}{\partial z} \bar{w}^* = \frac{1}{\rho_0 a \cos \phi} \nabla \cdot \mathbf{F} + \bar{X} \quad (4.1)$$

$$\frac{1}{a \cos \phi} \frac{\partial \bar{v}^* \cos \phi}{\partial \phi} + \frac{1}{\rho_0} \frac{\partial \rho_0 \bar{w}^*}{\partial z} = 0 \quad (4.2)$$

$$\bar{w}_m^* = \frac{1}{\rho_0 \cos \phi} \frac{\partial}{\partial \phi} \left[\int_z^\infty \left\{ \frac{\rho_0 a \cos^2 \phi (-\bar{u}_t + (\rho_0 a \cos \phi)^{-1} \nabla \cdot \mathbf{F} + \bar{X})}{\bar{m}_\phi} \right\} dz' \right]_{\bar{m}=\text{const}} \quad (4.3)$$

and latitudinal mean (from ϕ_1 to ϕ_2) residual mean vertical wind

$\langle \bar{w}_m^* \rangle \equiv \int \bar{w}^* \cos \phi d\phi / \int \cos \phi d\phi$ is calculated as follows;

$$\langle \bar{w}_m^* \rangle = \frac{\int_z^\infty \left\{ \frac{\rho_0 a \cos^2 \phi \left(-\bar{u}_t + (\rho_0 a \cos \phi)^{-1} \nabla[\mathbf{F} + \bar{X}] \right)}{\bar{m}_\phi} \right\}_{\bar{m}=\text{const}} dz'}{\rho_0 \int_{\phi_1}^{\phi_2} a \cos \phi d\phi} \quad (4.4)$$

where $\bar{m} = a \cos \phi (\bar{u} + a\Omega \cos \phi)$, zonal mean angular momentum per unit mass, \bar{w}_m^* is residual mean vertical wind from eastward momentum balance and continuity, and angle bracket is latitudinal mean. These integrations are calculated from top to corresponding levels along with constant \bar{m} . Under steady-state conditions, equations (4.3) and (4.4) reduce to the “downward control mechanism” [Haynes *et al.*, 1991]. Without steady-state restriction, equations (4.3) and (4.4) include contribution of \bar{u}_t . Unlike Randel *et al.* [2008], in equation (4.3) and (4.4), we added eastward residual forcing \bar{X} which consists of residual term in equation (4.1) and thus includes unresolved wave forcing and frictional forcing near planetary boundary layer. Under the quasi-geostrophic approximation, that is $\bar{m}_\phi / a \cos^2 \phi \approx -f$, contribution of the zonal body forcing G to latitudinal mean upwelling is proportional to vertical integration of sum of the forcing at the edges of latitudinal band (from $-\phi_1$ to ϕ_1), because the Coriolis parameters are same magnitude but reverse sign;

$$\langle \bar{w}_m^* \rangle \propto - \int_z^\infty G(-\phi_1, z') + G(\phi_1, z') dz'. \quad (4.5)$$

4.3. Transformed Eulerian Mean Thermodynamic analysis

Figure 4.3 shows climatological anomalies of zonal mean temperature and of TEM thermodynamic balance averaged between 10°S and 10°N . Tropical temperature anomalies show similar annual cycle between 125 and 70 hPa. In all levels, there are balances between vertical advection and diabatic heating. Convergence of vertical heat flux cools strongly in boreal winter and weakly in boreal summer at 70 hPa, has semiannual variations at 100 hPa, and warms up especially in boreal winter and weakly in boreal summer at 125 hPa.

Between 125 and 70 hPa, especially at 100 hPa, the diabatic heating has high

anticorrelation with the temperature (correlation coefficients are -0.83, -0.98, and -0.86 at 125, 100, and 70 hPa, respectively).

A simple estimate of diabatic heating in the case of less condensation is formed by solar heating and Newtonian (longwave) cooling; $Q = Q_{solar} + Q_{Newtonian}$ where $Q_{Newtonian} = -1/\tau (\theta - \theta_{Q=0})$ is diabatic heating anomaly estimated by Newtonian cooling, τ is radiative relaxation time. If diabatic heating is dominated by longwave cooling, diabatic heating has passive variation to temperature changes, and vertical advection is the main contributor to annual cycle of the temperature. As introduced in Fueglistaler et al. [2009a], probable radiative relaxation time near the tropical tropopause is in the range of 15-30 days. The estimation mentioned above is valid between 100 and 70 hPa. The difference of diabatic heating from ERA-Interim and Newtonian cooling can be approximated by solar heating, that is $Q^* = Q - Q_{Newtonian} \approx Q_{solar}$, where Q^* is residual diabatic heating.

Here, we perform Newtonian cooling model as used in *Kerr-Munslow and Norton* (2006);

$$\frac{\partial \bar{\theta}}{\partial t} = -\bar{w}^* \frac{\partial \bar{\theta}}{\partial z} - \frac{1}{\rho_0} \frac{\partial (\rho_0 \overline{w'\theta'})}{\partial z} + \bar{Q}^* - \frac{1}{\tau} (\bar{\theta} - \bar{\theta}_{mean}), \quad (4.6)$$

where $\bar{Q}^* = \bar{Q} + (\bar{\theta} - \bar{\theta}_{mean})_{reanalysis} / \tau$ is residual diabatic heating which is difference between diabatic heating from ERA-Interim and from Newtonian cooling, and it is considered that the residual diabatic heating mainly consists of solar heating. To estimate residual diabatic heating, potential temperature anomaly is calculated from ERA-Interim. Thermodynamical forcing terms consist of the vertical advection, vertical heat flux convergence, and residual diabatic heating. We input each forcing term into the right-hand-side of equation (4.6), and simulate the temperature variation imposed by the forcing. Radiative relaxation times used here are 20 days.

Figure 4.4 shows zonal mean temperature averaged over 10° S-10° N estimated by Newtonian cooling model of equation (4.6). In the case of all forcings (black lines in Figure 4.4), estimated temperature anomaly is in complete accordance with the observed temperature anomaly from ERA-Interim in all levels. Vertical advection induces temperature variation at 70 hPa higher in February and July and lower in April and November (blue lines in Figure 4.4a). Peak-to-peak amplitude of the temperature anomaly forced by the vertical advection is 4.5 K (blue line in Figure 4.4a).

Peak-to-peak amplitude of the temperature anomaly forced by the residual diabatic heating is 5 K (red line in Figure 4.4a). Vertical convergence of the vertical heat flux causes temperature variation which the highest is in October and the lowest in February (peak-to-peak amplitude is 2 K). Considering seasonal variation in solar heating, it is plausible that temperature variation imposed by residual diabatic heating is higher in boreal summer and lower values in boreal winter at 70 hPa. Observed ozone concentration from HALOE in the tropics at 68 hPa is higher in boreal summer and lower in boreal winter [see *Fueglistaler et al.*, 2010]. However, ozone concentration in the tropical lower stratosphere depends on tropical upwelling. Thus, practical role of tropical upwelling in the temperature change at 70 hPa is more important than the temperature change shown in Figure 4.4a.

At 100 hPa, vertical advection well reproduces the observed annual cycle in temperature anomaly at 100 hPa (blue lines in Figure 4.4b). However, amplitude of the temperature variation is slightly larger than that from the observation, and peak-to-peak amplitude is 5K in the case of forced only by the vertical advection. Adding the vertical heat flux convergence to the vertical advection as forcing, estimated temperature anomaly is closely similar to the observed temperature anomaly (gray line in Figure 4.4b).

As shown in Figure 4.4, at 100 hPa large part of variation in diabatic heating is consistent with longwave cooling, and temperature variation is primary given by the vertical advection. At 70 hPa, residual diabatic heating and vertical advection induce most part of temperature variation. The upwelling is the main driver for annual cycle in the tropical temperature at 100 hPa, and has a large impact on the annual cycle at 70 hPa. Next we consider what causes annual cycle in tropical upwelling between 125 and 70 hPa.

4.4. Upwelling estimated from zonal mean momentum budget

To examine what forcing contributes the tropical upwelling, we calculate the residual mean vertical wind from eastward momentum budget and continuity following steady downward control mechanism by *Haynes et al.* [1991] (see Section 4.2). Due to strong balance between vertical advection and diabatic heating and small variation in time change rate of the temperature as shown in Figure 4.3, thermodynamic balance is near

steady-state. Thus, the residual mean vertical flow is approximately diabatic flow, and downward control mechanism works out well.

Figure 4.5 compares residual mean vertical wind from the estimate and that from reanalysis. Except for 5°S - 5°N , estimated residual mean vertical winds are quite similar to that from reanalysis. It is considered that the estimation works well. In the case estimating residual mean vertical wind averaged over 10°S - 10°N , as noted in equation (4.4) we use the data only near 10°S and 10°N . Hence, the errors between 5°S and 5°N have no practical impact on the tropical mean estimation.

Figure 4.6 compares the residual mean vertical wind from both estimate and reanalysis averaged over 10°S - 10°N . At 70 hPa annual cycle in $\langle \bar{w}_m^* \rangle$ is similar variation to $\langle \bar{w}_m^* \rangle$ from reanalysis except for larger amplitude (Figure 4.6a). Eastward residual forcing is the main driver of annual cycle of $\langle \bar{w}_m^* \rangle$ at 70 hPa, and contribution of \bar{u}_t cancels contribution of other forcings from May to July and in November.

At 100 hPa, $\langle \bar{w}_m^* \rangle$ has closely similar variation and amplitude to $\langle \bar{w}_m^* \rangle$ from reanalysis (Figure 4.6b). Contribution of \bar{u}_t to $\langle \bar{w}_m^* \rangle$ is small (largest amplitude at -0.2 mm/s in June), and $\langle \bar{w}_m^* \rangle$ excluding the contribution of \bar{u}_t (forced by the EP flux divergence and eastward residual forcing) has similar annual cycle to $\langle \bar{w}_m^* \rangle$ from reanalysis. The EP flux divergence has a significant contribution to difference of $\langle \bar{w}_m^* \rangle$ between boreal winter and summer (peak-to-peak value is about 0.6 mm/s). The eastward residual forcing promotes semiannual variation peaking in both April and November (peak-to-peak value is 0.5 mm/s). Strong upwelling in April is driven by both the EP flux divergence and eastward residual forcing.

Estimated 125-hPa $\langle \bar{w}_m^* \rangle$ also has similar variation and amplitude to residual mean vertical wind from reanalysis without contribution of \bar{u}_t (Figure 4.6c). Same as 100 hPa, difference of $\langle \bar{w}_m^* \rangle$ between boreal winter and summer is mainly induced by EP flux divergence (peak-to-peak value is 1.1 mm/s), and strong upwelling in April is driven by both the EP flux divergence and eastward residual forcing.

At 70 hPa, the EP flux divergence induces small variation in tropical upwelling that consists of stronger in boreal winter and weaker in boreal summer/fall (peak-to-peak value is about 0.1 mm/s). Meridional divergence of F_2^{ϕ} (corresponding to meridional eddy momentum flux $\overline{u'v'}$) and vertical divergence of F_1^z (corresponding to meridional eddy heat flux $\overline{v'\theta'}$) are main contributors to its variation from EP flux

divergence (Figure 4.6d). At 100 hPa, meridional divergence of F_2^ϕ and vertical divergence of F_2^z (corresponding to vertical flux of zonal momentum $\overline{u'w'}$) mainly induce tropical upwelling variation based on the EP flux divergence (Figure 4.6e; both peak-to-peak values are 0.3 mm/s). At 125 hPa, same as 100 hPa, contributions of divergence of F_2^ϕ and F_2^z are dominant in variation in tropical ascent based on the EP flux divergence, but divergence of F_2^z has stronger contribution to tropical upwelling than that of F_2^ϕ (Figure 4.6f; peak-to-peak values are 0.4 mm/s for F_2^ϕ and 0.8 mm/s for F_2^z). Next, we investigate what levels of forcing has a strong influence on the tropical upwelling between 125 and 70 hPa.

Figure 4.7 shows annual cycle of residual mean vertical wind based on forcing from the parts of whole layers. At 70 hPa, most of $\langle \overline{w}_m^* \rangle$ is driven by forcing below 10 hPa, and about a half of annual cycle of the $\langle \overline{w}_m^* \rangle$ is driven by forcing above 50 hPa (Figure 4.7a). However, due to strong contribution of \overline{u}_t , this breakdown is not accurate. Large part of 100-hPa annual cycle of the tropical upwelling is based on forcing below 70 hPa (Figure 4.7b; peak-to-peak amplitude is 0.75 mm/s). Forcing above 70 hPa drives the small variation in residual mean vertical wind, which has peak-to-peak amplitude at 0.15 mm/s. Most part of the 125-hPa tropical upwelling is also generated by forcing below 70 hPa (Figure 4.7c).

As shown in Figures 4.6 and 4.7, EP flux divergence below 70 hPa has the largest contribution to 125 and 100 hPa tropical upwelling difference between boreal winter and summer. Next, we consider what kind of wave activity has a large contribution to difference in the tropical upwelling between December and August.

4.5. Wave activity driving tropical upwelling

Figure 4.8 shows the EP flux, meridional divergence of meridional components of the EP flux and vertical divergence of vertical components of the EP flux, and estimated residual mean vertical wind based on corresponding wave forcing in December.

The EP flux between 150 and 70 hPa directs equator-upward near both 20° S and 20° N and north-upward near the equator. Strong meridional convergence occurs in north of 5° N, divergence around the equator, and convergence in south of 10° S, 100 hPa (Figure 4.8a and 4.8d). These wave forcings drive strong upwelling near 10° N, downwelling

near the equator, and upwelling near 5°S . Vertical convergence occurs around the equator, 125 hPa and promotes upwelling centered at the equator, 150 hPa and downwelling near both 5°S and 5°N (Figure 4.8b and 4.8e). In total, the EP flux diverges around 7°S , 200 hPa and converges broadly around 100 hPa (Figure 4.8c and 4.8f), and drives upwelling centered at 10°S below 125 hPa and between the equator and 10°N below 70 hPa.

Figure 4.9 is the same as Figure 4.8 but in August. There is southward EP flux around the equator, 150 hPa. Near both 20°S and 20°N , the EP flux directs equator-upward above 150 hPa. Strong meridional divergence occurs around 5°N , 150 hPa, strong meridional convergence around 10°S , 150 hPa, and meridional convergence around 20°N , 200 hPa (Figure 4.9a and 4.9d). These wave forcings drive upwelling around 10°N below 125 hPa and downwelling south of 10°S . Vertical convergence occurs around the equator, 150 hPa, which is enclosed by vertical divergence (Figure 4.9b and 4.9e). These wave forcings induce upwelling below 125 hPa around 5°S , and downwelling below 125 hPa around both 10°S and 5°N . In total, the EP flux diverges around 5°N , 150 hPa and converges around 10°S , 150 hPa, and drives upwelling near 10°N and downwelling near 10°S (Figure 4.9c and 4.9f). The amplitude of the vertical wind is weak around 100 hPa.

Compared to December, tropical wave forcing of both meridional and vertical components is weaker and locates lower levels in August. Thus tropical upwelling in August is weaker than that in December. Next, we examine the EP flux in greater detail to diagnose what types of waves are involved.

Figure 4.10 shows annual cycle of $\langle \bar{w}_m^* \rangle$ based on each component of wave forcing decomposed into the contributions from stationary component (wave forcing from monthly mean field) and transient component (residual component) at 125 and 100 hPa. At 100 hPa stationary component of $F_2^{(\phi)}$ drives stronger upwelling in boreal winter and weaker upwelling in boreal summer (Figure 4.10a). Transient component has small contribution to difference between boreal winter and summer, and induces upwelling in May. $F_1^{(z)}$ induces relatively small variation in upwelling (Figure 4.10b). Stationary component of $F_2^{(z)}$ induces most of variation in total $F_2^{(z)}$, and transient component drives weak semiannual variation in vertical wind (Figure 4.10c). Difference of upwelling between boreal winter and summer is mainly driven by stationary

components of $F_2^{(\phi)}$ and $F_2^{(z)}$. At 125 hPa, $F_2^{(\phi)}$ and $F_2^{(z)}$ induce similar variation in upwelling to that at 100 hPa (Figure 4.10d and 4.10f) except its amplitude. Variation in the upwelling induced by stationary component of $F_1^{(z)}$ is smaller than that at 100 hPa in boreal winter (Figure 4.10e).

As expressed in equation (4.5), the contribution of zonal body forcing to tropical upwelling is roughly assessed by sum of zonal body forcing at the edges of latitudinal band under the assumption of quasi-geostrophic condition. Figure 4.11 shows annual cycle of stationary and transient components of $F_2^{(\phi)}$ and its divergence at 90 hPa over 20°S - 20°N . In boreal winter, meridional convergences of total $F_2^{(\phi)}$ around 10°N are mainly generated by poleward-propagating waves in the tropics and equatorward-propagating waves from the northern hemispheric midlatitude (Figure 4.11a). Stationary component of $F_2^{(\phi)}$ mainly contributes to the meridional convergence of total $F_2^{(\phi)}$ (Figure 4.11b). These waves consist of planetary and synoptic scale waves (zonal wave number 1-4; data are not shown). Regions of meridional convergence of stationary $F_2^{(\phi)}$ around 10°S and 10°N move southward from November to February, which is coincided with southward shift of tropical convection (see also Figure 4.15c). Transient $F_2^{(\phi)}$ generates relatively weak meridional convergence in the winter hemispheric subtropics especially in May, and tends to form meridional divergence around the latitude where convection is active (Figure 4.11c; see also Figure 4.15c).

Sum of convergence of total $F_2^{(\phi)}$ at 10°S and 10°N is stronger in boreal winter and weaker in late-summer/fall, due to contribution of stationary $F_2^{(\phi)}$ at 10°N (Figure 4.11d and 4.11e). In addition, relatively large value in April and May is promoted in the Southern hemisphere, which is generated by transient $F_2^{(\phi)}$ (blue lines in Figure 4.11d and 4.11f). Thus, stationary component of $F_2^{(\phi)}$ contributes to about a half of tropical upwelling variation which is stronger in boreal winter and weaker in boreal summer, and transient component of $F_2^{(\phi)}$ slightly contributes to tropical upwelling in May.

Figure 4.12 shows annual cycle of stationary and transient components of $F_2^{(z)}$ at 100 hPa and its vertical divergence at 90 hPa over 20°S - 20°N . Total $F_2^{(z)}$ at 100 hPa over 10°S - 10°N is positive in boreal winter and negative in boreal summer (Figure 4.12a). Decaying the amplitude of $F_2^{(z)}$ with height, at 90 hPa vertical convergence occurs in boreal winter and vertical divergence in boreal summer. Stationary component

of $F_2^{(z)}$ strongly contributes to the vertical convergence of $F_2^{(z)}$ in boreal winter, and weakly diverges at around 5°N in boreal summer (Figure 4.12b). It is a remarkable result that tropical stationary $F_2^{(z)}$ changes sign with seasonal variation. Transient component of $F_2^{(z)}$ contributes to vertical divergence of total $F_2^{(z)}$ at around equator especially in boreal summer (Figure 4.12c). Regions of vertical divergence of transient stationary $F_2^{(z)}$ at around the equator move to south and north with season, which corresponds to moving the region where tropical convection is active (see also Figure 4.15c).

Sum of divergence of total $F_2^{(z)}$ at 10°S and 10°N is negative (convergence) in boreal winter and positive in late-summer/fall, due to contribution of stationary $F_2^{(z)}$ especially at 10°N (Figure 4.12d and 4.12e). From June to October, divergence of stationary $F_2^{(z)}$ occurs at 10°N , and relatively weak convergence at 10°S . In April, October, and November, when maximum of divergence of transient $F_2^{(z)}$ locates near the equator, sum of divergence of transient $F_2^{(z)}$ at 10°S and 10°N is small (Figure 4.12f).

To evaluate the structure of stationary $F_2^{(\phi)}$ (corresponding to $-\overline{u'v'}\cos\phi$), Figure 4.13 shows climatology of horizontal wind and geopotential height deviations from zonal mean at 100 hPa in December and August. In December, easterly momentum is transported equatorward in the subtropical eastern Pacific and Atlantic (so-called “westerly duct” region), and poleward in the tropical western Pacific and the Indian Ocean due to Matsuno-Gill type circulation pattern (Figure 4.13a). Thus, $-\overline{u'v'}\cos\phi < 0$ occurs in the subtropics of northern hemisphere, and $-\overline{u'v'}\cos\phi > 0$ near the equator. The momentum transport forms strong convergence of stationary component of $F_2^{(\phi)}$ around 15°N . In August, easterly momentum transports southward around southeastern Asia associated with the Asian summer monsoon pattern. However, the momentum transport is clearly weaker than that in December, and it generates only weak convergence at around 10°N (Figure 4.13d).

To assess the structure of stationary $F_2^{(z)}$ (corresponding to $-\overline{u'w'}$), Figure 4.14 shows climatological wind and geopotential deviations from zonal mean averaged over 4.5°S - 4.5°N in longitude-height section. In December there are westward and upward flow around 140°E and eastward and downward flow around 100°W and 20°W in the upper troposphere (Figure 4.14a). These winds transport easterly momentum upward,

that is $-\overline{u'w'} > 0$, and weaken with height at around 100 hPa, therefore vertical convergence of $F_2^{(z)}$ is generated. In August, amplitude of winds between 150 and 100 hPa is weaker than that in December, and westward and downward winds around 70°E contributes to transport easterly momentum downward weakly between 125 and 100 hPa, that is $-\overline{u'w'} < 0$ (Figure 4.14b). The westward and downward winds correspond to decent part of summer monsoon pattern. Thus, weak divergence of $F_2^{(z)}$ is generated in the tropics around 100 hPa.

4.6. Behavior of eastward residual forcing

Eastward residual forcing is the main contributor to semiannual variation of the tropical upwelling between 125 and 70 hPa. Tropical upwelling at 100 hPa estimated by Randel et al. (2008), which excluded contribution of eastward residual forcing, did not reproduce the strong upwelling in April. Hence, the contribution of the eastward residual forcing is plausible.

Figure 4.15 shows annual cycle of eastward residual forcing \bar{X} , and OLR between 20°S and 20°N at 50 and 90 hPa. Sum of the eastward residual forcing at 10°S and 10°N has semiannual variation which is strong negative in boreal spring and fall (Figure 4.15a and 4.15b). It causes strong tropical upwelling in boreal spring and fall. The eastward residual forcing is almost anticorrelated with zonal wind at lower level. In addition, the eastward residual forcing is large near the equator when tropical convection is active (Figure 4.15c). Therefore, it is presumable that a large part of the eastward residual forcing consists of gravity waves.

4.7. Summary

In summary, the remarkable findings in this chapter are as follows;

- 1) The annual cycle in tropical temperature between 125 and 70 hPa are mainly driven by annual cycle in tropical upwelling.
- 2) Steady downward control mechanism can almost entirely explain the annual cycle in the tropical upwelling at 125 and 100 hPa, and due to long radiative relaxation time, annual cycle in tropical upwelling at 70 hPa is smaller than that estimated from steady downward control mechanism.

3) Variation in tropical upwelling between boreal winter and summer is driven by the EP flux divergence, and semiannual variation in the tropical upwelling is driven by residual forcing.

4) Variation in the EP flux divergence between boreal winter and summer is dominated by stationary waves with meridional divergence of meridional eddy momentum flux (corresponding to $-\overline{u'v'}$) and vertical divergence of vertical flux of zonal momentum (corresponding to $-\overline{u'w'}$), and semiannual variation is dominated by transient waves with meridional divergence of meridional eddy momentum flux and vertical divergence of vertical flux of zonal momentum.

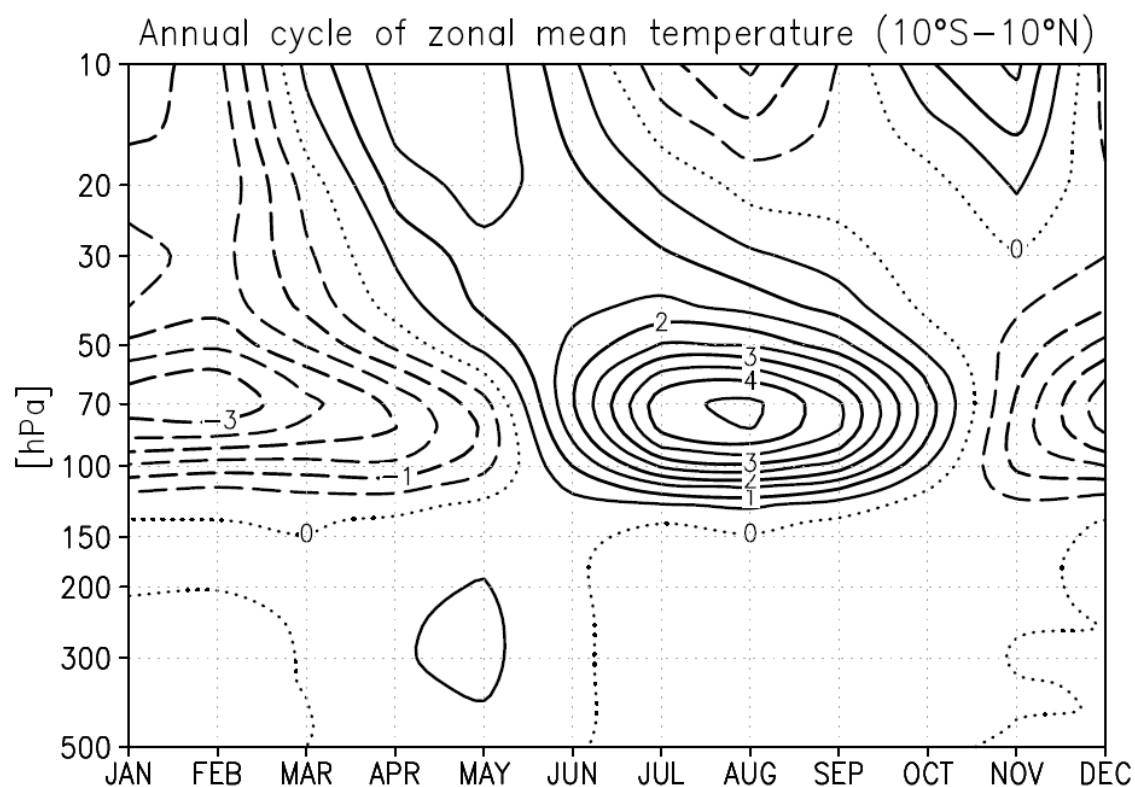


Figure 4.1. Annual cycle in the temperature averaged over 10S-10N from ECMWF ERA-Interim 1989-2009 (time mean has been removed). Contour interval is 0.5 K; solid contours indicate positive values, dashed contours negative values, dotted is the zero contour.

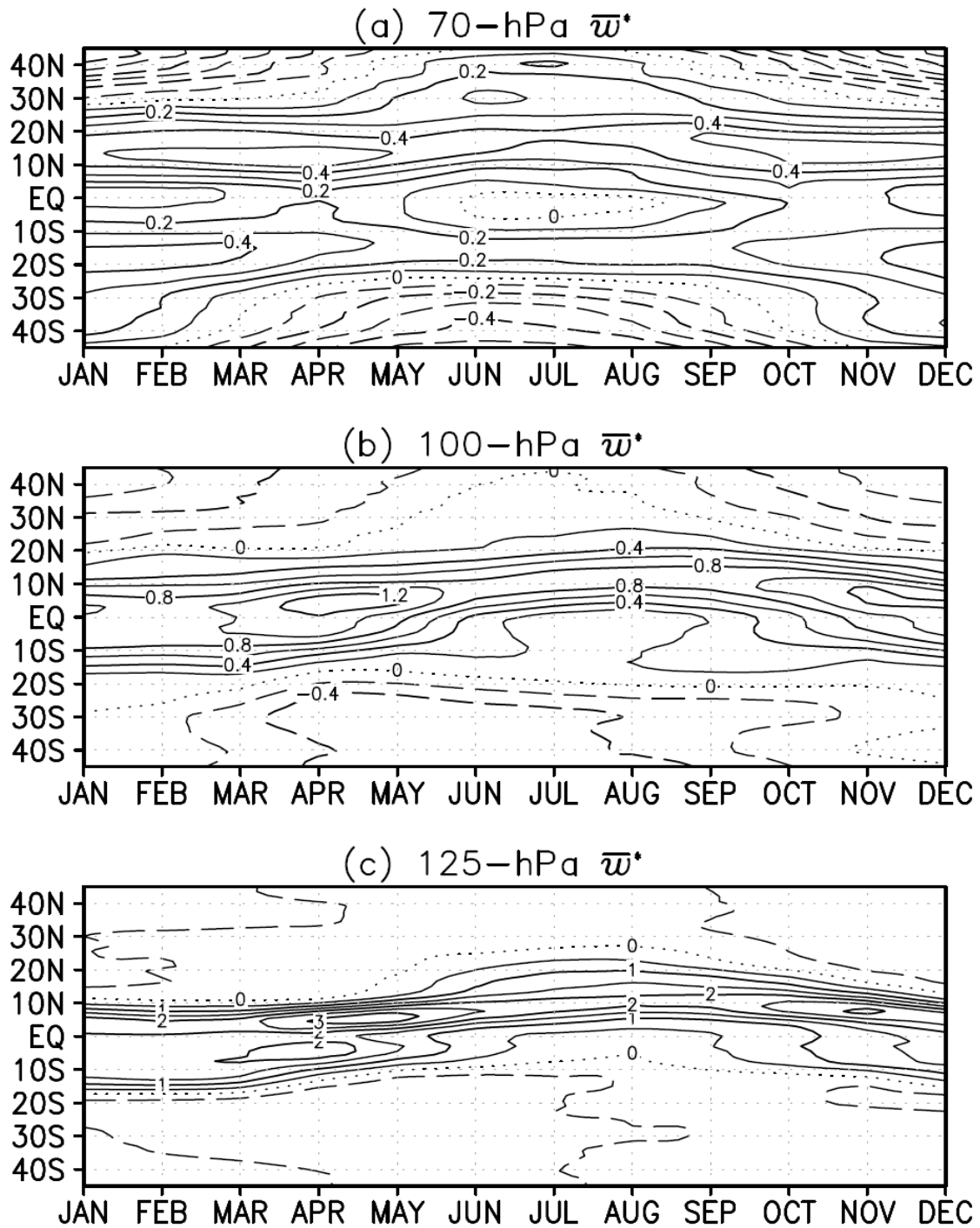


Figure 4.2. Annual cycle in the residual mean vertical wind at (a) 70 hPa, (b) 100 hPa, and (c) 125 hPa from ECMWF ERA-Interim 1989-2009 (time mean has been removed). Contour intervals are (a) 0.1 mm s^{-1} , (b) 0.2 mm s^{-1} , and (c) 0.5 mm s^{-1} ; solid contours indicate positive values, dashed contours negative values, dotted is the zero contour.

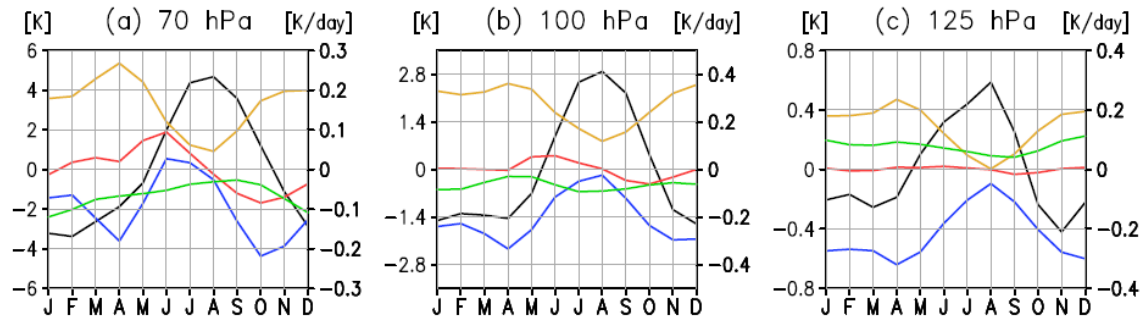


Figure 4.3. Annual cycle in the zonal-mean temperature (K; black) and major terms in the transformed Eulerian mean (TEM) thermodynamic equation averaged over 10°S – 10°N (K d^{-1}). (a) 70 hPa, (b) 100 hPa, (c) 125 hPa. The terms in the TEM thermodynamic equation consist of potential temperature change (red), vertical advection (blue lines), convergence of vertical heat flux (green), and diabatic heating (yellow). Other terms are not shown. Time mean has been removed for zonal mean temperature.

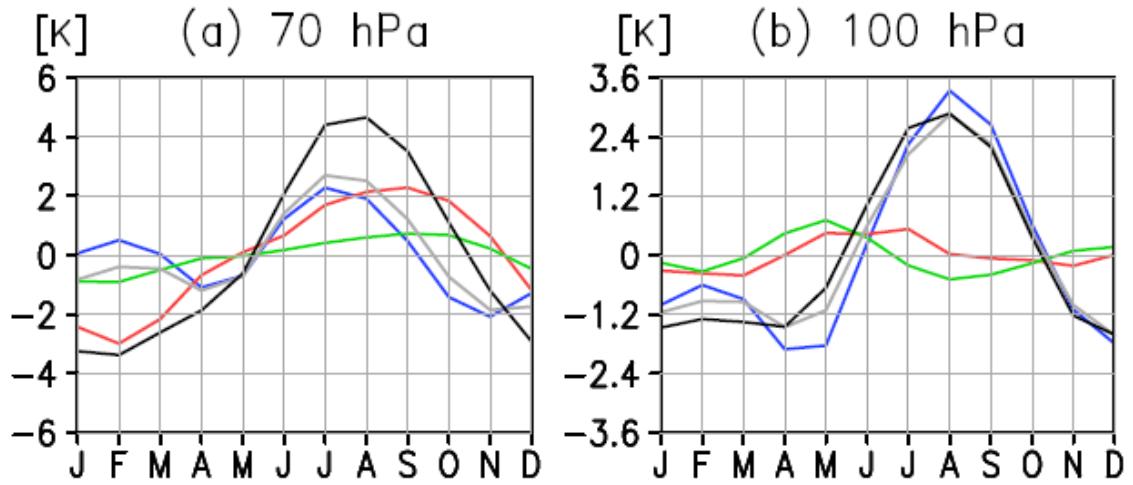


Figure 4.4. Annual cycle in the zonal-mean temperature averaged between 10°S and 10°N at (a) 70 hPa and (b) 100 hPa: results from Newtonian cooling model of equation (4.6); imposed by total forcing (black), vertical advection $-\bar{w}^*(\partial\bar{\theta}/\partial z)$ (blue), vertical convergence of the vertical heat flux $-1/\rho_0(\partial\rho_0\overline{w'\theta'}/\partial z)$ (green), $-\bar{w}^*(\partial\bar{\theta}/\partial z)-1/\rho_0(\partial\rho_0\overline{w'\theta'}/\partial z)$ (gray), and residual diabatic heating \bar{Q}^* (red). Radiative relaxation time used in this model is 20 days.

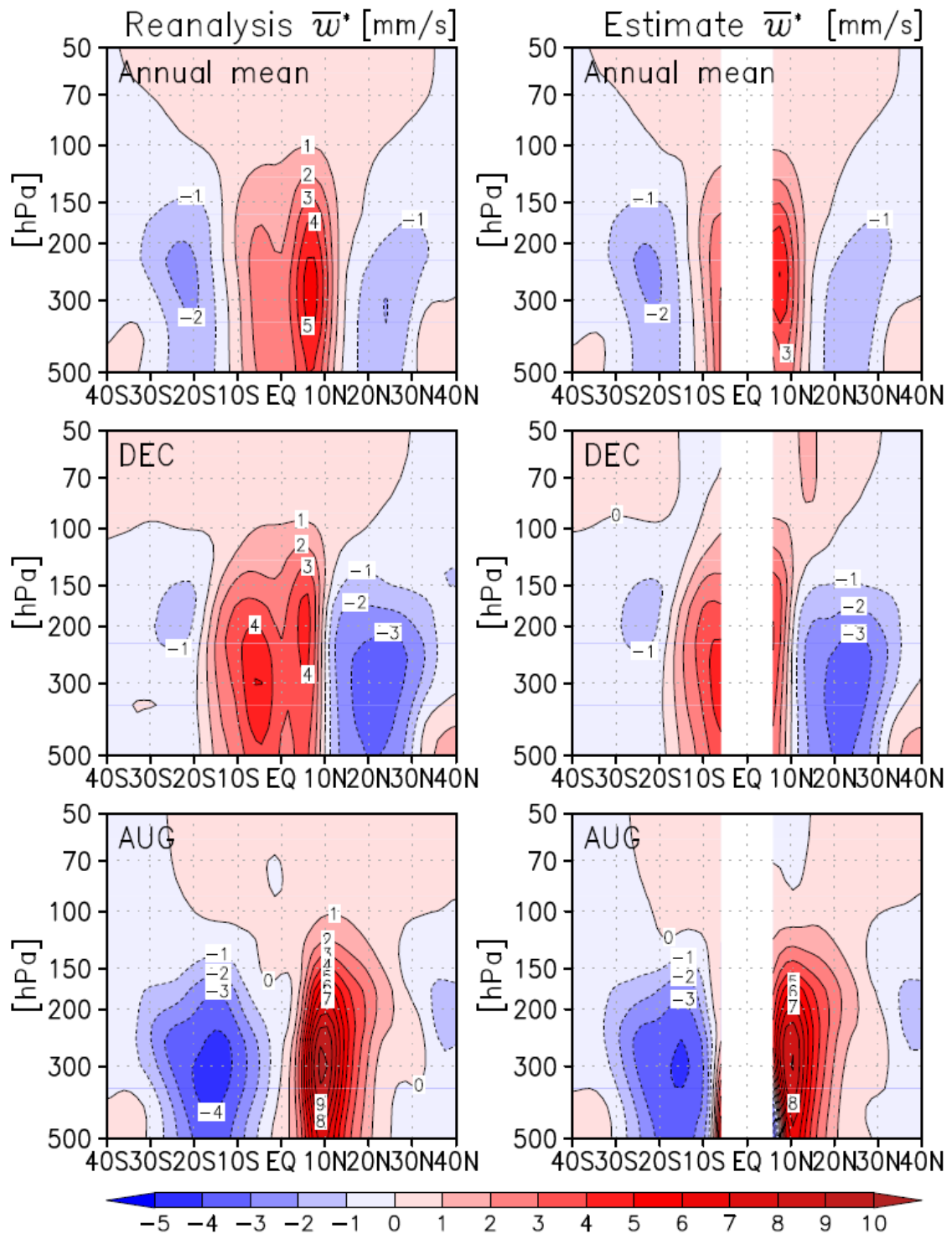


Figure 4.5. Comparison of the climatological residual mean vertical wind between (left) reanalysis and (right) estimate by Eq. (4.3) in latitude-height section. Results are in (top) Annual mean, (center) December, and (bottom) August.

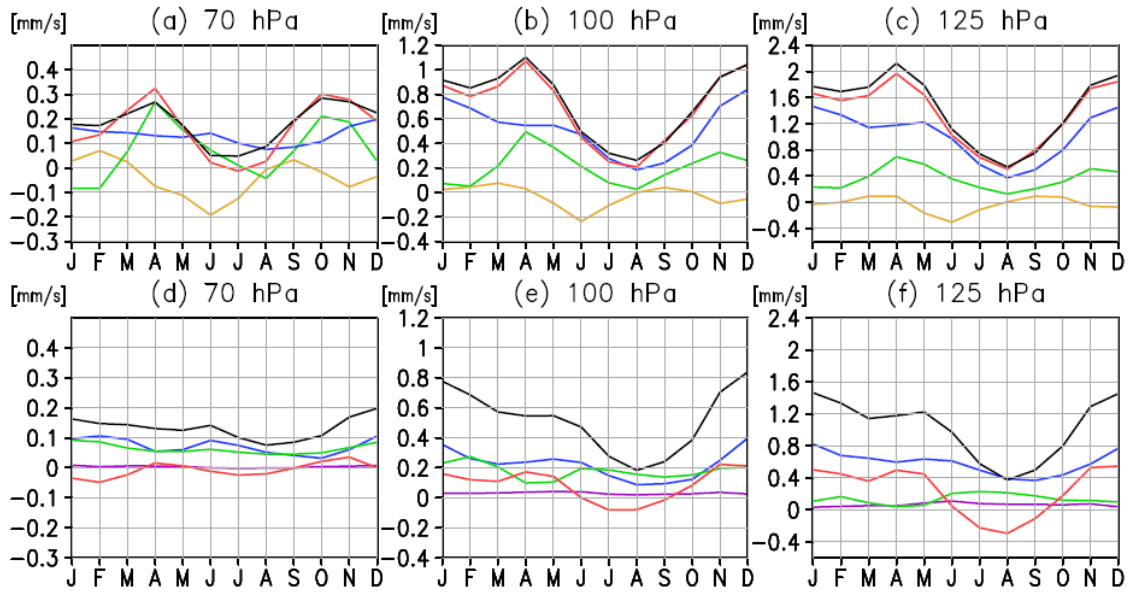


Figure 4.6. (top) Annual cycle in the residual mean vertical wind averaged over 10°S - 10°N from reanalysis (black lines) and from estimate by Eq. (4.4) (red lines) at (a) 70 hPa (b) 100 hPa (c) 125 hPa. The separate lines correspond to EP flux divergence (blue lines), residual forcing (green lines), and \bar{u}_i (yellow lines). (bottom) Annual cycle in residual mean vertical wind based on EP flux divergence (black lines) and on corresponding to $F_1^{(\phi)}$ (purple lines), $F_2^{(\phi)}$ (blue lines), $F_1^{(z)}$ (green lines), and $F_2^{(z)}$ (red lines) at (d) 70 hPa (e) 100 hPa (f) 125 hPa.

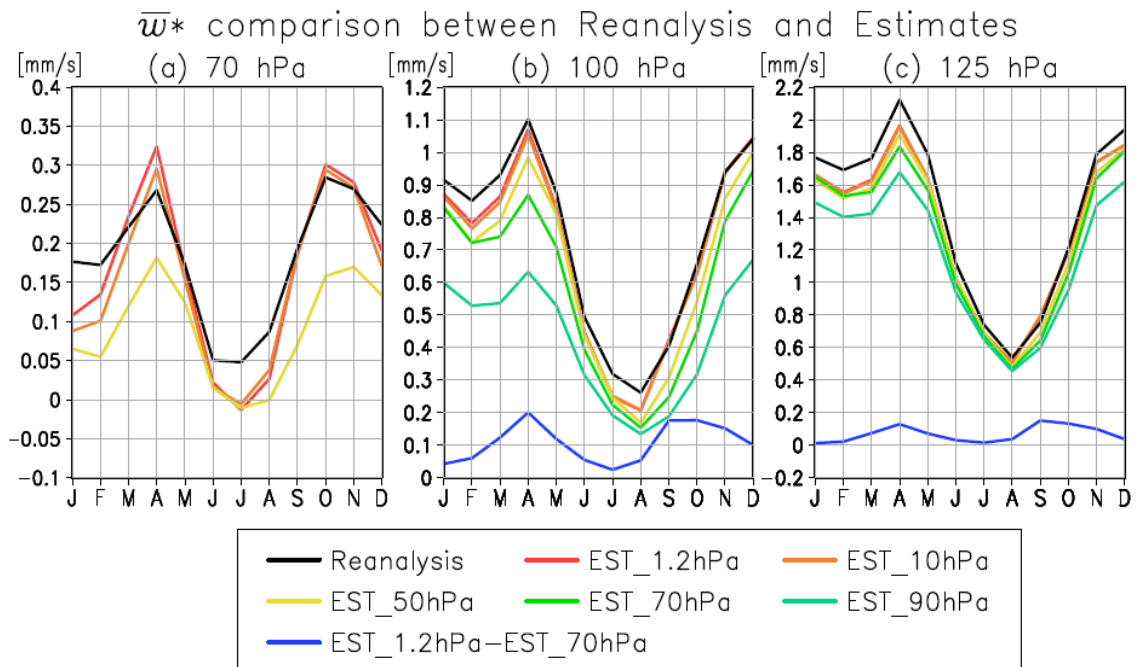


Figure 4.7. Annual cycle in the residual mean vertical wind averaged over 10°S - 10°N from reanalysis (black lines) and from estimate by Eq. (4.4) (red lines). The separate lines are estimate from forcing below 10 hPa (orange lines), 50 hPa (yellow lines), 70 hPa (green lines), 90 hPa (aqua lines), and above 70 hPa (blue lines). Results are at (a) 70 hPa (b) 100 hPa (c) 125 hPa.

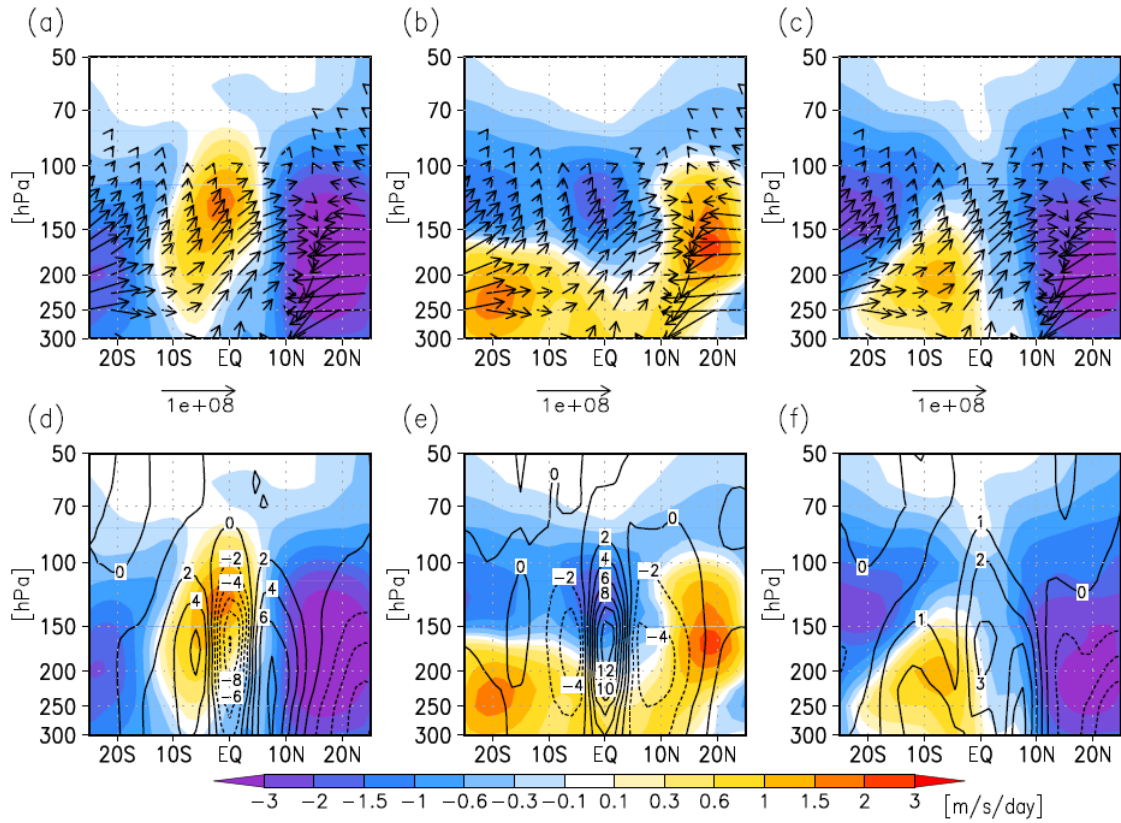


Figure 4.8. (top) Latitude-height section of the climatological EP flux (vector) and components of divergence of the EP flux (color) in December. Colors are (a) meridional divergence of $F_1^{(\phi)} + F_2^{(\phi)}$, (b) vertical divergence of $F_1^{(z)} + F_2^{(z)}$, and (c) divergence of the EP flux. (bottom) Colors are same as top, and contours are residual mean vertical wind based on (d) meridional divergence of $F_1^{(\phi)} + F_2^{(\phi)}$, (e) vertical divergence of $F_1^{(z)} + F_2^{(z)}$, and (f) divergence of the EP flux. Contour intervals are (d, e) 2 mm s^{-1} and (f) 1 mm s^{-1} .

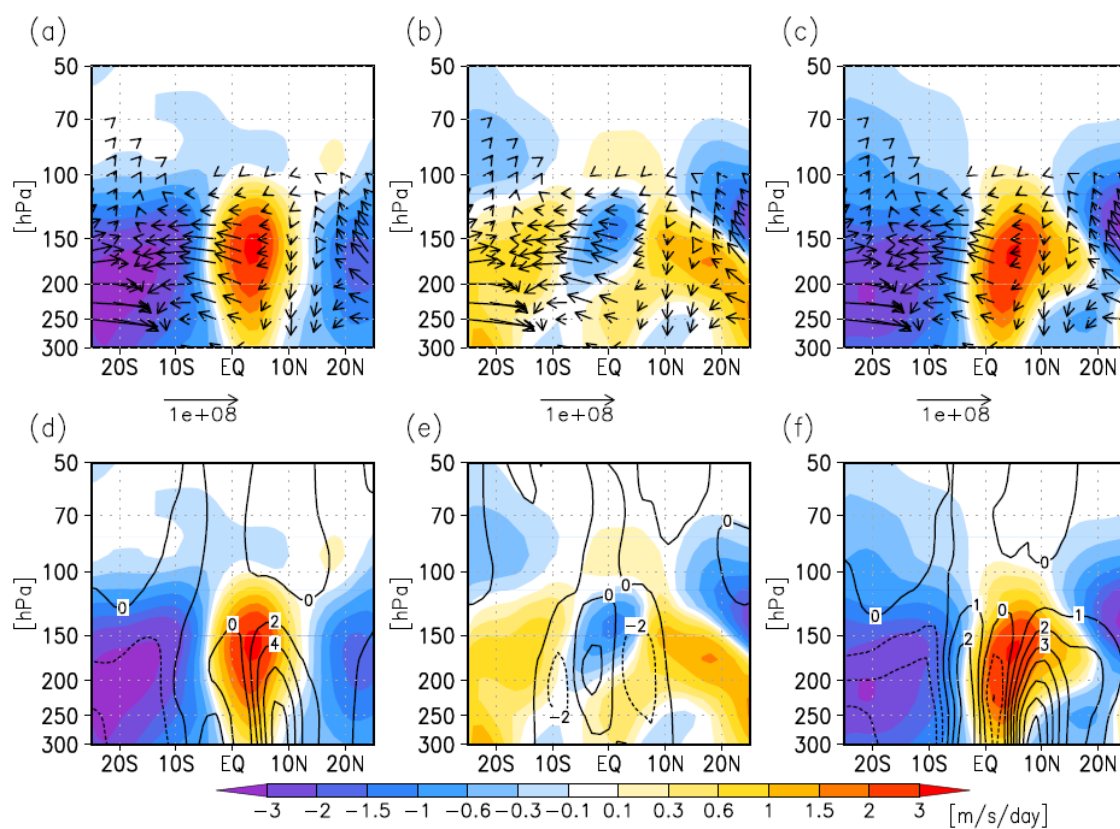


Figure 4.9. Same as Figure 4.8, but in August.

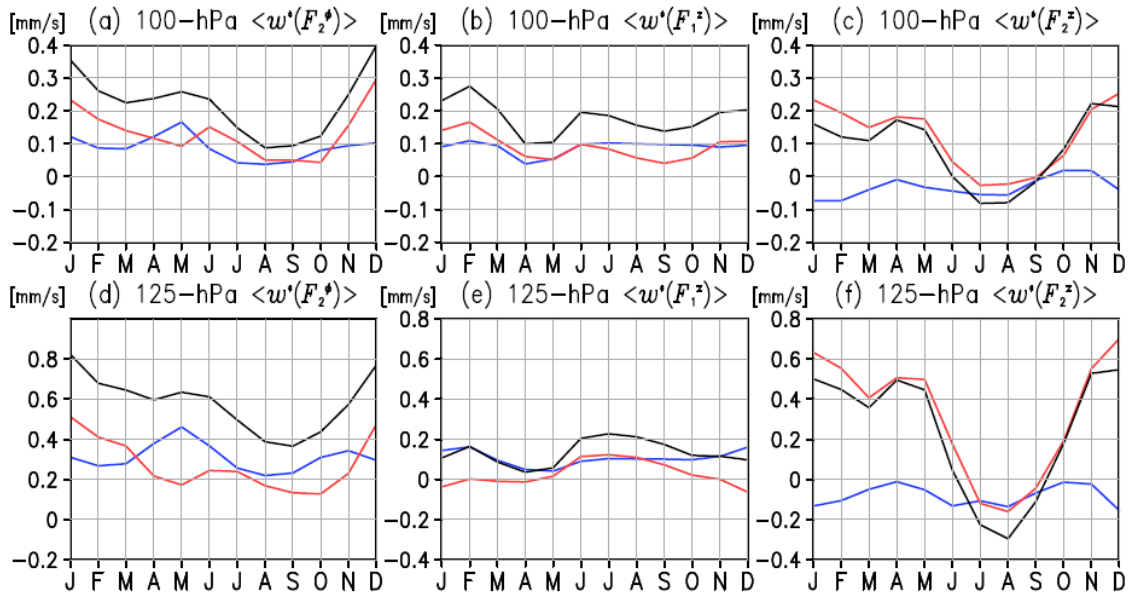


Figure 4.10. Annual cycle in the residual mean vertical wind driven by each component of divergence of the EP flux (top) at 100 hPa (bottom) at 125 hPa. (left) Meridional divergence of $F_2^{(\phi)}$, (center) vertical divergence of $F_1^{(z)}$, and (right) vertical divergence of $F_2^{(z)}$. Meridional divergence of $F_1^{(\phi)}$ is not shown due to its smallness. Black lines are stationary plus transient components, red lines are stationary component, and blue lines are transient component.

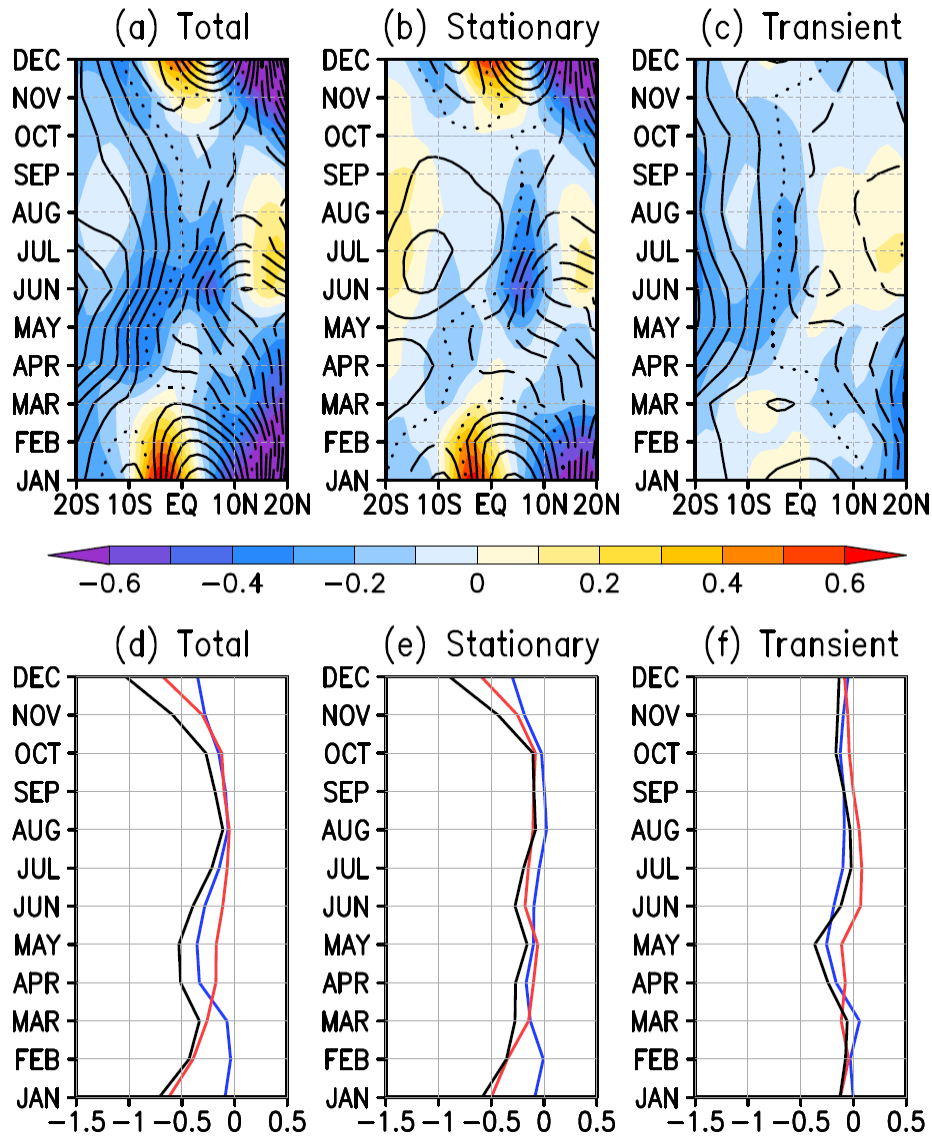


Figure 4.11. (top) Latitude-time section of meridional component of the climatological EP flux $F_2^{(\phi)}$ (contour) and its meridional divergence (color; m/s/day) at 90 hPa. (a) Total (b) stationary component, (c) transient component. (bottom) Sum of convergence of $F_2^{(\phi)}$ at 10°S and 10°N (black), convergence of $F_2^{(\phi)}$ at 10°S (blue), and convergence of $F_2^{(\phi)}$ at 10°N (red). (d) Total, (e) stationary component, and (f) transient component. Contour intervals are (top) $5 \times 10^5 \text{ kg s}^{-2}$; solid contours indicate positive values, dashed contours negative values, dotted is the zero contour.

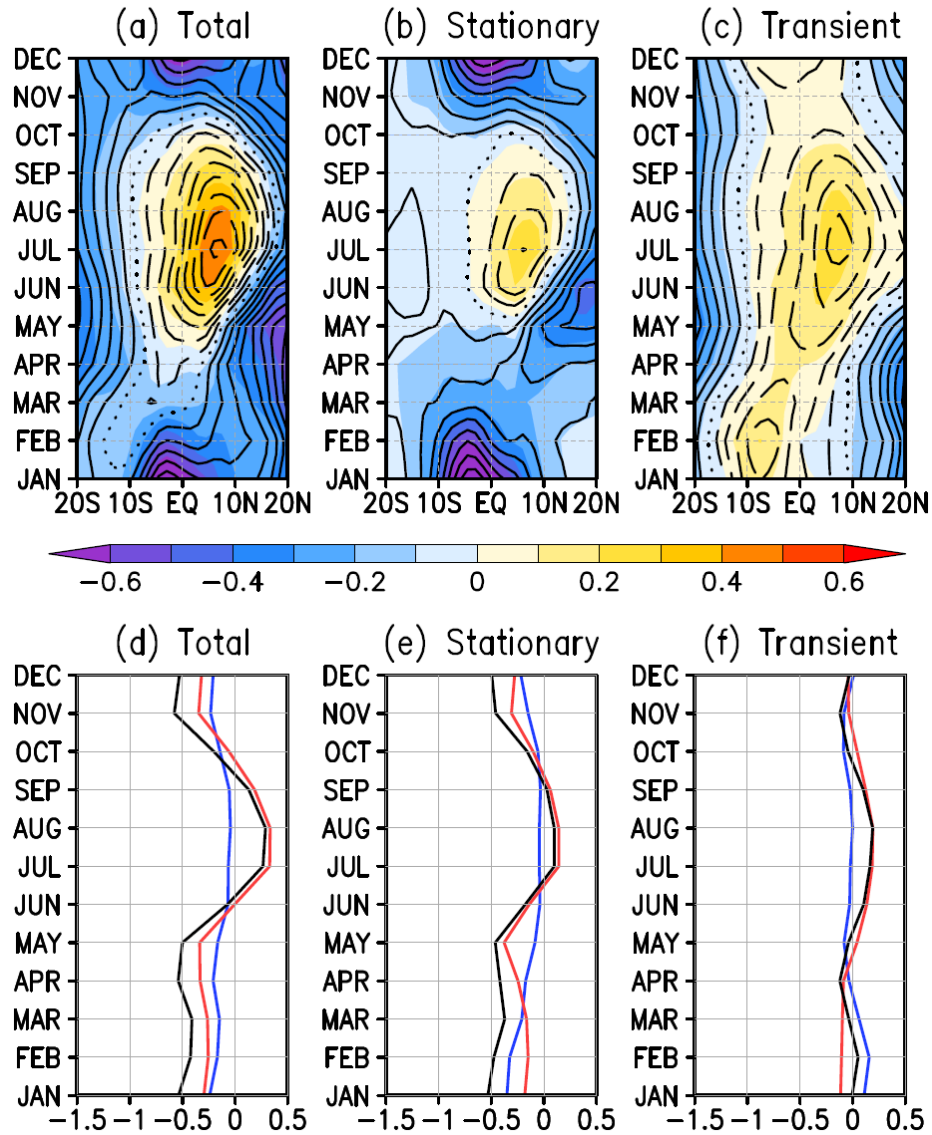


Figure 4.12. (top) Latitude-time section of vertical component of the climatological EP flux $F_2^{(z)}$ at 100 hPa (contour) and its vertical divergence at 90 hPa (color; $\text{m s}^{-1}\text{d}^{-1}$). (a) Total (b) stationary component, (c) transient component. (bottom) Sum of convergence of $F_2^{(\phi)}$ at 10° S and 10° N (black), convergence of $F_2^{(\phi)}$ at 10° S (blue), and convergence of $F_2^{(\phi)}$ at 10° N (red). (d) Total, (e) stationary component, and (f) transient component. Contour intervals are (top) $1 \times 10^3 \text{ kg s}^{-2}$; solid contours indicate positive values, dashed contours negative values, dotted is the zero contour.

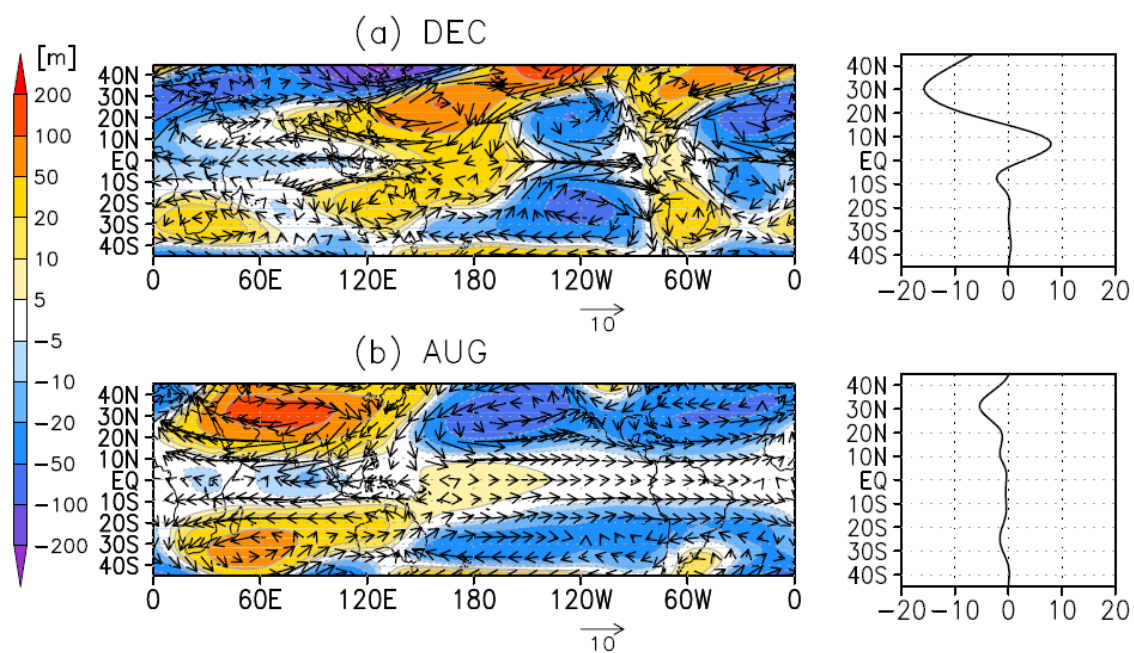


Figure 4.13. (left) Maps of the climatological horizontal wind (vector) and geopotential height (color; m) at 100 hPa in (a) December (b) August (the data are deviation from zonal mean). (right) Latitudinal profile of $-\overline{u'v'} \cos \phi$ (m² s⁻²) at 100 hPa.

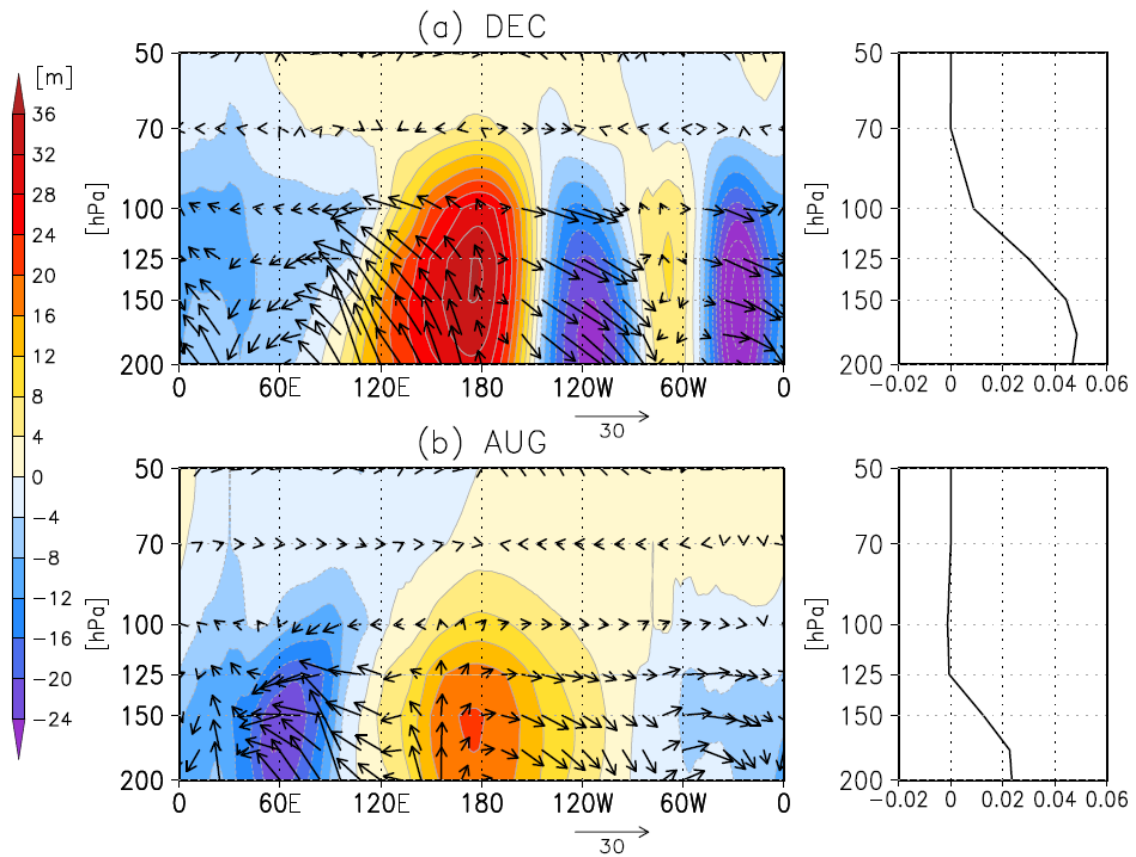


Figure 4.14. (left) Longitude-height section of the climatological vector wind and geopotential height (color; m) averaged over 4.5°S - 4.5°N in (a) December (b) August (the data are deviation from zonal mean). (right) Vertical profile of $-\overline{u'w'}$ ($\text{m}^2 \text{s}^{-2}$) averaged over 4.5°S - 4.5°N .

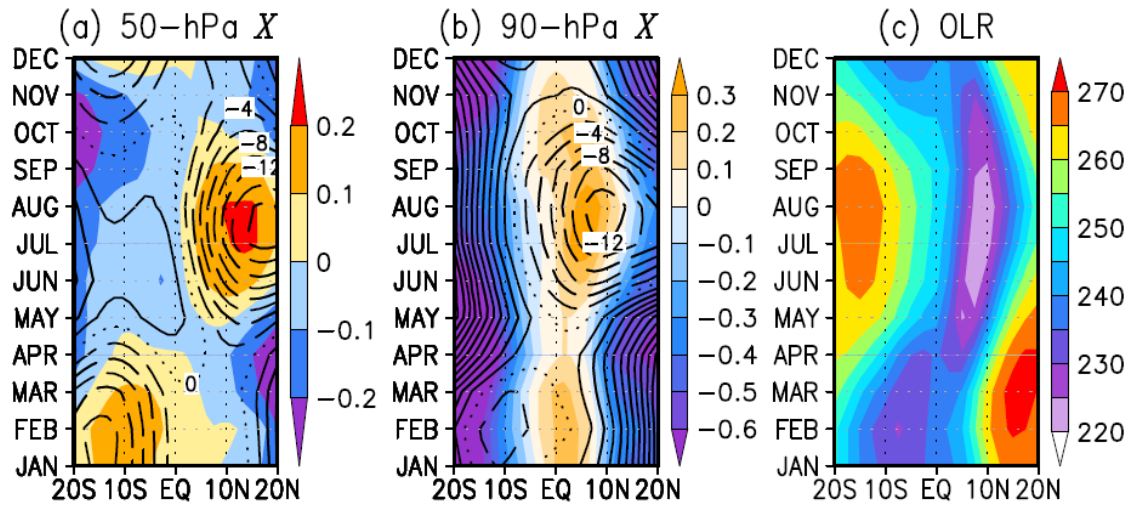


Figure 4.15. Latitude-time section of the climatological eastward residual forcing (color; $\text{m s}^{-1}\text{d}^{-1}$) at (a) 50 hPa (b) 90 hPa and (c) outgoing longwave radiation (color; W m^{-2}). Contour shows climatological zonal wind at (a) 70 hPa (b) 125 hPa (m s^{-1}). Contour interval is 2 m/s ; solid contours indicate positive values, dashed contours negative values, dotted is the zero contour.

Chapter 5| General conclusion

In present study, we have investigated temperature changes in the tropical tropopause layer (TTL) in the cases of tropical sea-surface temperature (SST) changes as in El Niño/Southern Oscillation, stratospheric sudden warming (SSW) event, and annual cycle.

In Chapter 2, we have revealed the role of vertical heat flux $\overline{w'\theta'}$ in the TTL associated with changes in tropical SST as in El Niño/Southern Oscillation for the first time. With decreasing (increasing) longitudinal gradient of tropical SST as in El Niño (La Niña), the vertical heat flux increases (decreases) zonal mean temperature in the tropics between 100 and 70 hPa and decreases (increases) between 150 and 125 hPa. In the case of El Niño event, minimum temperature in the cold-point tropopause is larger than that in La Niña event (*Hatsushika and Yamazaki, 2001*), and it corresponds to weakening of dehydration in the TTL. Because the vertical heat flux increases zonal mean temperature in the case of El Niño event, dehydration in the TTL is furthermore weakens.

In Chapter 3, during a major SSW event of January 2009, changes in the temperature in the tropics between 150 and 100 hPa are induced by tropical upwelling which is driven by the tropospheric wave forcing from equatorward-propagating waves excited in the midlatitudes troposphere rather than the stratospheric forcing associated with SSW. In addition, vertical heat flux $\overline{w'\theta'}$, which is closely tied to convection structure, also induced changes in the temperature in the tropics between 150 and 125 hPa. This is a case study and the present results may not valid in other SSWs. Further study is needed for this issue.

In Chapter 4, we have revealed that annual cycle in tropical temperature between 125 and 70 hPa is mainly driven by annual variation in tropical upwelling and consequent diabatic heating. The eastward residual forcing mainly drives annual cycle in tropical upwelling at 70 hPa. Variation in 125-100 hPa tropical upwelling between boreal winter and summer is dominated by wave forcing of stationary waves with meridional eddy momentum flux ($F_2^{(\phi)}$) and vertical flux of zonal momentum ($F_2^{(z)}$), and semiannual variation is dominated by eastward residual forcing and wave forcing of transient waves with $F_2^{(\phi)}$ and $F_2^{(z)}$. Randel et al. (2008) suggested that $F_2^{(\phi)}$ has a large contribution

to variation in 100 hPa upwelling over 15°S - 15°N between boreal winter and summer. However, a contribution of $F_2^{(\phi)}$ for tropical upwelling is weaker in 10°S - 10°N than that in 15°S - 15°N . In addition, importance of $F_2^{(z)}$ for 125-100 hPa upwelling over 10°S - 10°N is quantitatively revealed in the present study. The eastward residual forcing has a strong impact for semiannual variation in 125-70 hPa upwelling over 10°S - 10°N , which is heretofore not pointed out. To investigate the eastward residual forcing for more detail, further study is needed.

Acknowledgements

I would express my sincere thanks to my supervisor Prof. Koji Yamazaki to guide, encourage and support me for 6 years. I would like to express my gratitude to Prof. Humio Hasebe, Dr. Masatomo Fujiwara, Dr. Takeshi Horinouchi, and Dr. Yuhji Kuroda for helpful and insightful comments. I would thank all members of Yamazaki laboratory, and Mr. Takeshi Watanabe's support was invaluable. Special thanks to all members of C-306. My deepest appreciation goes to all members of course in atmosphere-ocean and climate dynamics. Finally, I would thank to my family for helpful support.

References

- Andrews, D. G., J. R. Holton, and C. B. Leovy (1987), *Middle Atmosphere Dynamics*, 489 pp., Elsevier, New York.
- Folkins, I., M. Loewenstein, J. Podolske, S. J. Oltmans, and M. Prodditt (1999), A Barrier to vertical mixing at 14 km in the tropics: Evidence from ozonesondes and aircraft measurements, *J. Geophys. Res.*, D18, 22095-22102.
- Fueglistaler, S., M. Bonazzola, P. H. Haynes, and T. Peter (2005), Stratospheric water vapor predicted from the Lagrangian temperature history of air entering the stratosphere in the tropics, *J. Geophys. Res.*, 110, D08107, doi: 10.1029/2004JD005516.
- Fueglistaler, S., A. E. Dessler, T. J. Dunkerton, I. Folkins, Q. Fu, and P. W. Mote (2009), Tropical tropopause layer, *Rev. Geophys.*, 47, RG1004, doi:10.1029/2008RG000267.
- Fueglistaler, S., B. Legras, A. Beljaars, J.-J. Morcrette, A. Simmons, A. M. Tompkins, S. Uppala (2009), The diabatic heat budget of the upper troposphere and lower/mid stratosphere in ECMWF reanalyses, *Quart J. Roy. Meteor. Soc.*, 135, 21–37, doi: 10.1002/qj.361.
- Fueglistaler, S., P. H. Haynes, and P. M. Forster (2010), The annual cycle in lower stratospheric temperatures revisited, *Atmos. Chem. Phys. Discuss.*, 10, 26813–26839, <http://www.atmos-chem-phys-discuss.net/10/26813/2010/>, doi:10.5194/acpd-10-26813-2010.
- Gates, W. L. (1992), AMIP: The atmospheric intercomparison project. *Bull. Amer. Meteor. Soc.*, 73, 1962–1970. (<http://www-pcmdi.llnl.gov/projects/amip/index.php>)
- Gill, A. E. (1980), Some simple solutions for heat-induced tropical circulation, *Quart J. Roy. Meteor. Soc.*, 106, 447–462.
- Harada, Y, A. Goto, H. Hasegawa, N. Fujikawa, H. Naoe, T. Hirooka (2010), A Major Stratospheric Sudden Warming Event in January 2009. *J. Atmos. Sci.*, 67, 2052-2069, doi: 10.1175/2009JAS3320.
- Hartmann, D. L., J. R. Holton, and Q. Fu (2001), The heat balance of the tropical tropopause, cirrus, and stratospheric dehydration, *Geophys. Res. Lett.*, 28, 1969–1972.
- Hartmann, D. L. (2007), The atmospheric general circulation and its variability, *J. Meteor. Soc. Japan*, 85B, 123–143.
- Hatsushika, H., and K. Yamazaki (2001), Interannual variations of temperature and vertical motion at the tropical tropopause associated with ENSO, *Geophys. Res. Lett.*, 28, 2891–2894.
- Hatsushika, H., and K. Yamazaki (2003), Stratospheric drain over Indonesia and dehydration within

- the tropical tropopause layer diagnosed by air parcel trajectories, *J. Geophys. Res.*, *108*(D19), 4610, doi:10.1029/2002JD002986.
- Haynes, P. H., C. J. Marks, M. E. McIntyre, T. G. Shepherd, and K. P. Shine (1991), On the “downward control” of extratropical diabatic circulations by eddy-induced mean zonal forces. *J. Atmos. Sci.*, *48*, 651–678.
- Haynes, P. H. and T. G. Shepherd (1989), The importance of surface pressure changes in the response of the atmosphere to zonally-symmetric thermal and mechanical forcing. *Quart. J. Roy. Meteor. Soc.*, *115*: 1181–1208. doi: 10.1002/qj.49711549002
- Highwood, E. J., and B. J. Hoskins (1998), The tropical tropopause, *Quart. J. Roy. Meteor. Soc.*, *124*, 1579–1604.
- Holton J. R., P. H. Haynes, M. E. McIntyre, A. R. Douglass, R. B. Rood, and L. Pfister (1995), Stratosphere-troposphere exchange, *Rev. Geophys.*, *33*, 403–439.
- Holton J. R., and A. Gettleman (2001), Horizontal transport and the dehydration of the stratosphere, *Geophys. Res. Lett.*, *28*, 2799–2802.
- Hu, Y., and K. K. Tung (2002), Interannual and Decadal Variations of Planetary Wave Activity, Stratospheric Cooling, and Northern Hemisphere Annular Mode. *J. Climate*, **15**, 1659–1673.
- Kerr-Munslow, A. M., and W. A. Norton (2006), Tropical wave driving of the annual cycle in tropical tropopause temperatures. Part I: ECMWF analyses, *J. Atmos. Sci.*, *63*, 1410–1419.
- Kiladis, G. N. (1998), An observational study of Rossby waves linked to convection over the eastern tropical Pacific. *J. Atmos. Sci.*, *55*, 321–339.
- Kiladis, G. N. and K. M. Weickmann (1997), Horizontal structure and seasonality of large-scale circulations associated with submonthly tropical convection. *Mon. Wea. Rev.*, **125**, 1997–2013.
- Kodera, K. (2006), Influence of stratospheric sudden warming on the equatorial troposphere, *Geophys. Res. Lett.*, *33*, L06804, doi:10.1029/2005GL024510.
- Kuroda, Y. (2008), Effect of stratospheric sudden warming and vortex intensification on the tropospheric climate, *J. Geophys. Res.*, *113*, D15110, doi:10.1029/2007JD009550.
- Kuroda, Y., and K. Kodera (2004), Role of the Polar-night Jet Oscillation on the formation of the Arctic Oscillation in the Northern Hemisphere winter, *J. Geophys. Res.*, *109*, D11112, doi:10.1029/2003JD004123.
- Labitzke, K., and M. Kunze (2009), On the remarkable Arctic winter in 2008/2009, *J. Geophys. Res.*, *114*, D00I02, doi:10.1029/2009JD012273.
- Liebmann B. and C.A. Smith (1996), Description of a Complete (Interpolated) Outgoing Longwave

- Radiation Dataset. *Bull. Am. Meteor. Soc.*, 77, 1275-1277.
- Manney, G. L., M. J. Schwartz, K. Krüger, M. L. Santee, S. Pawson, J. N. Lee, W. H. Daffer, R. A. Fuller, and N. J. Livesey (2009), Aura Microwave Limb Sounder observations of dynamics and transport during the record-breaking 2009 Arctic stratospheric major warming, *Geophys. Res. Lett.*, 36, L12815, doi:10.1029/2009GL038586.
- Marti, J., and K. Mauersberger (1993), A survey and new measurements of ice vapor pressure at temperatures between 170 and 250K, *Geophys. Res. Lett.*, 20(5), 363-366.
- Matsuno, T. (1966), Quasi-geostrophic motions in the equatorial area, *J. Meteor. Soc. Japan*, 44, 25-43.
- Matsuno, T. (1970), Vertical propagation of stationary planetary waves in the winter Northern Hemisphere. *J. Atmos. Sci.*, 27, 871-883.
- Matsuno, T. (1971), A dynamical model of the stratospheric sudden warming, *J. Atmos. Sci.*, 28, 1479-1494.
- Matthews, A. J., G. N. Kiladis (2000), A Model of Rossby Waves Linked to Submonthly Convection over the Eastern Tropical Pacific. *J. Atmos. Sci.*, 57, 3785-3798.
- Monge-Sanz, B. M., M. P. Chipperfield, A. J. Simmons, and S. M. Uppala (2007), Mean age of air and transport in a CTM: Comparison of different ECMWF analyses, *Geophys. Res. Lett.*, 34, L04801, doi:10.1029/2006GL028515.
- Norton, W. A. (2006), Tropical wave driving of the annual cycle in tropical tropopause temperatures. Part II: Model results, *J. Atmos. Sci.*, 63, 1420-1431.
- Numaguti, A., M. Takahashi, T. Nakajima, and A. Sumi (1995), Development of an atmospheric general circulation model, in *Reports of a New Program for Creative Basic Research Studies, Studies of Global Environment Change with Special Reference to Asia and Pacific Regions, Rep. I-3*, pp. 1-27, Center for Climate System Research, Tokyo.
- Olsen, M. A., M. R. Schoeberl, and J. E. Nielsen (2007), Response of stratospheric circulation and stratosphere-troposphere exchange to changing sea surface temperatures, *J. Geophys. Res.*, 112, D16104, doi:10.1029/2006JD008012.
- Plumb, R. A. (1982), Zonally symmetric Hough modes and meridional circulations in the middle atmosphere, *J. Atmos. Sci.*, 39, 983-991.
- Plumb, R. A. (1985), On the Three-Dimensional Propagation of Stationary Waves, *J. Atmos. Sci.*, 42, 217-229.
- Plumb, R. A., and J. Eluszkiewicz (1999), The Brewer-Dobson circulation: Dynamics of the tropical

- upwelling, *J. Atmos. Sci.*, 56, 868–890.
- Randel, William J., R. Garcia, F. Wu, (2008), Dynamical Balances and Tropical Stratospheric Upwelling. *J. Atmos. Sci.*, 65, 3584–3595. doi: 10.1175/2008JAS2756.1
- Schoeberl, M. R., A. R. Douglass, Z. Zhu, and S. Pawson (2003), A comparison of the lower stratospheric age spectra derived from a general circulation model and two data assimilation systems, *J. Geophys. Res.*, 108, D3, 4113, doi:10.1029/2002JD002652.
- Simmons, A. J., and J. K. Gibson (2000), The ERA-40 project plan, *ERA-40 Project Report Series, Tech. Rep. I*, 63 pp., European Centre for Medium-Range Weather Forecasts, Reading, U.K.
- Simmons, A. J., S. M. Uppala, D. Dee, and S. Kobayashi (2006), ERA-Interim: New ECMWF reanalysis product from 1989 onwards, *ECMWF Newsletter*, 110, 25–35.
- Trenberth, K. E., and L. Smith (2006), The vertical structure of temperature in the tropics: Different flavors of El Niño, *J. Climate*, 19, 4956–4970.
- Uppala, S. M., P. W. Kallberg, A. J. Simmons, U. Andrae, V. da Costa Bechtold, M. Fiorino, J. K. Gibson, J. Haseler, A. Hernandez, G. A. Kelly, X. Li, K. Onogi, S. Saarinen, N. Sokka, R. P. Allan, E. Andersson, K. Arpe, M. A. Balmaseda, A. C. M. Beljaars, L. van de Berg, J. Bidlot, N. Bormann, S. Caires, F. Chevallier, A. Dethof, M. Dragosavac, M. Fisher, M. Fuentes, S. Hagemann, E. Holm, B. J. Hoskins, L. Isaksen, P. A. E. M. Janssen, R. Jenne, A. P. McNally, J.-F. Mahfouf, J.-J. Morcrette, N. A. Rayner, R. W. Saunders, P. Simon, A. Sterl, K. E. Trenberth, A. Untch, D. Vasiljevic, P. Viterbo, and J. Woollen (2005), The ERA-40 re-analysis, *Quart. J. Roy. Meteor. Soc.*, 131, 2961–3012.
- Uppala, S. M., D. Dee, S. Kobayashi, P. Berrisford, and A. Simmons (2008), Towards a climate data assimilation system: status update of ERA-Interim, *ECMWF Newsletter*, 115, 12–18.
- Vecchi, G. A., B. J. Soden, A. T. Wittenberg, I. M. Held, and A. Leetmaa (2006), Weakening of tropical Pacific atmospheric circulation due to anthropogenic forcing, *Nature*, 441, doi:10.1038/nature04744.
- Webster, P. J., and J. R. Holton (1982), Cross-equatorial response to middle-latitude forcing with a latitudinally and zonally nonuniform basic state. *J. Atmos. Sci.*, 39, 722–733.
- Yamaguchi, K., and A. Noda (2006), Global warming patterns over the North Pacific: ENSO versus AO, *J. Meteor. Soc. Japan*, 84, 221–241.
- Yoshida, K., and K. Yamazaki (2010), Role of vertical eddy heat flux in the response of tropical tropopause temperature to changes in tropical sea surface temperature, *J. Geophys. Res.*, 115, D01108, doi:10.1029/2009JD012783.

Yulaeva, E., J. R. Holton, and J. M. Wallace (1994), On the cause of the annual cycle in tropical lower-stratospheric temperatures, *J. Atmos. Sci.*, 51, 169–174.